Chapter 3

GMRT H I SYNTHESIS OBSERVATIONS

Abstract:

The GMRT H I 21cm-line observations of galaxies in the Eridanus group are presented. A total of 46 galaxies of different morphological types were observed, out of which 31 galaxies were detected. The typical observing time on each galaxy was $\sim$ 4 hour. A total of $\sim$ 200 hour of the GMRT observations were carried out. The images presented in this thesis are at a spatial resolution of $20'' - 30''$ and at a velocity resolution of $\sim$ 13.4 km s^{-1} . A 5σ sensitivity of $\sim$ 3.5 mJy beam^{-1} per channel was obtained, which corresponds to a 5σ sensitivity of $\sim 1 \times 10^{20}$ cm^{-2} to the H I column density. The corresponding 5σ sensitivity to H I mass is 1.2×10^7 M$_\odot$ for an H I line-width of 50 km s^{-1} . The weakest detection is 8.0×10^7 M$_\odot$ of H I mass for an S0 galaxy. Total H I images, velocity fields, global H I line profiles, H I mass surface densities, H I disk parameters, and H I rotation curves are presented. The approaching and the receding sides of galaxies are analysed separately. The data will be used to study the H I content of the Eridanus group, H I and radio continuum morphological studies of galaxies, and the Tully-Fisher relations.

Keywords: Radio synthesis imaging, GMRT, spectral-line data analyses, H I moment maps, H I velocity fields, H I rotation curves.

3.1 Introduction

In this chapter, the Giant Meterwave Radio Telescope (GMRT) H I 21cm-line synthesis observations of galaxies in the Eridanus group are presented. This data will be used to study the following:

- H I content and H I morphological studies of galaxies in the Eridanus group. The main aim is to identify galaxy evolution processes in a group environment.
- Tully-Fisher (TF) relations. The main aim is to study the slope and the scatter in the *classical* TF relation and the baryonic (stellar+gas mass) TF relation.
- Radio continuum properties of some galaxies in the Eridanus group. The emphasis will be to understand the nature of galaxies deviating from the mean radio-fir correlation.

The present GMRT H I observations offer several advantages over studies carried out in the past using single dish telescopes. The GMRT has a mix of short and long interferometric baselines. This arrangement makes it possible to obtain images sensitive to diffuse H I emission from galaxies at resolutions adequate for the present purpose. The GMRT is expected to be sensitive to image structures on the scales of $2'' - 7'$. The angular sizes of the galaxies in the Eridanus group are in the range $1' - 5'$, implying that the data should be sensitive to image radio emission (H I and continuum) over the entire galactic disk. However, large sizes of galaxies and diffuse nature of H I also implies that at higher angular resolutions, flux per beam will decrease. This will limit the highest angular resolution with which images can be obtained with sufficient signal to noise ratio. For the present work, an angular resolution in the range $20'' - 30''$ ($2 - 3$ kpc at a distance of the Eridanus group as $\sim$ 23 Mpc) was found to be adequate for the H I imaging. The radio continuum emission from galaxies may have both diffuse component and compact emission from active nucleus. In order to identify such compact nuclear emission, one needs high angular resolution images. The GMRT is, therefore, an unique instrument which allows one to simultaneously obtain images sensitive to diffuse emission and images at sufficiently high angular resolutions from the same observations.

Typical values of rms in the channel (width 62.5 kHz) images are 0.7–0.8 mJy beam^{-1}. This corresponds to a column density sensitivity (5σ) of $\sim 1 \times 10^{20}$ cm^{-2} at an angular and velocity resolution of $20''$ and $\sim$ 13.4 km s^{-1} respectively. The corresponding sensitivity for the H I detection of a galaxy with an H I line-width of 50 km s^{-1} is 1.2×10^7 M$_\odot$.

In this chapter, H I images are presented. The radio continuum images are presented in Chap 7. The details of the observations are described in the next section. A brief introduction of principles behind synthesis imaging and the GMRT array is given in Sect. 3.3. The data reduction procedures are described in Sect. 3.4. Details of image analyses are given in Sect. 3.5. Some H I properties of galaxies are discussed in Sect. 3.6. An atlas comprising of total H I images, H I velocity fields, H I global profiles, H I mass surface densities, position-velocity (XV) diagrams, H I rotation curves, and H I disk parameters of galaxies as a function of galacto-centric distance are presented at the end of the chapter. The results are presented in Tab. 4.2.

3.2 Observations

The observations were carried out typically for $\sim$ 3.5 hour on each galaxy using 8 MHz bandwidth. The observations were carried out for longer duration (8 hour) for some early type galaxies and in certain cases where smaller bandwidths (2-4 MHz) were selected for lower inclination galaxies to get enough velocity resolution. A total of $\sim$ 200 hour of GMRT observations were carried out spread over a period of 2 years (2000–2002). The observations with 8 MHz bandwidth have a velocity resolution of $\sim$ 13.4 km s^{-1} . The GMRT does not provide a real-time Doppler tracking. This lack of Doppler tracking can introduce a maximum velocity smearing of $\sim$ 1 km s^{-1} . This smearing is insignificant compared to the velocity resolution of the observations. The observations carried out during November, 2001 were corrupted due to scintillation which were possibly related to the strong solar activity in that year. This data consist of observations on 15 galaxies were discarded. Five galaxies from these lost observations were re-observed later in 2002. We do not see any effect of solar RFI (Radio Frequency Interference) in the data collected during in the months of May – June although R.A. of the Eridanus group is close to that of the Sun but the difference in the two declinations was more than 40° . No other terrestrial RFI was noticed in the data, however, some internal RFI was seen in 2-3 channels.

The details of each pointings are given in Tab. 3.1. These pointings are marked in Fig. 3.1.

3.3 Imaging principles and array properties

The GMRT uses the principle of aperture synthesis invented by Ryle & Hewish (1960). Briefly, each correlation measurement across a baseline gives a point in the spatial frequency (u, v) plane which is sampled from a certain minimum value to a maximum value as baseline vectors change due to the rotation of the earth. This minimum value decides the largest angular extent of a region which can be imaged by the array. The array will be insensitive to any emission which is smoothly distributed on an angular scale larger than this value. The resolution is decided by the maximum value of the spatial frequency. The Van Cittert Zernike theorem relates this spatial correlation function (visibility) to the intensity distribution in the sky via Fourier transform. A typical sampling of the Fourier plane obtained from the GMRT observations and the Fourier inversion of the same are shown in Fig. 3.3.

The GMRT is an interferometric array of thirty 45m diameter fully steerable parabolic dishes. A description of the GMRT is given by Swarup et al. (1990). The GMRT is located at a site (longitude = 74° .05 E, latitude = 19° .092 N, height $\sim$ 650m above MSL) about 80 km north of Pune, India. The design of the GMRT antennas is based on a concept of Stretch Mesh Attached to Rope Trusses (SMART). This concept made possible the fabrication of light weight ($\sim$ 80 tonnes) alt-azimuth mountable dishes suitable for the meterwave radio observations. A light thin wire mesh of 0.55 mm diameter with a grid size varying from 10×10 mm in the inner 1/3 area of the dish, 15×15 mm in the middle 1/3 area of the dish, and 20×20 mm in the outer 1/3 area stretched over the rope truss facets forms the reflecting surface of the dish. The aperture efficiency of a GMRT dish is $\sim$ 40% at the L band (900 MHz - 1450 MHz) and $\sim$ 60% at other frequencies (150 MHz, 233 MHz, 327 MHz, and 610 MHz). The gain (K/Jy) of an antenna is $\sim$ 0.22 at L band and $\sim$ 0.33 at other frequencies. The sum of the receiver and ground temperature is $\sim$ 66 K at L band, $\sim$ 82 K at 610 MHz, $\sim$ 68 K at 327 MHz and 233 MHz, and $\sim$ 174 K at 150 MHz. The full width at half maximum of the primary beam of an antenna is 24′ at L band, 54′ at 610 MHz, 1° .8 at 327 MHz, 2° .5 at 233 MHz, and 3° .8 at 150 MHz.

The configuration of the GMRT array is optimized to meet the requirement of high angular resolution at low frequencies as well as imaging radio emission from diffuse extended regions. This

Table 3.1: Observational details

#	Date	Pointing centre		Galaxy	Separation	rms
		α (J2000)	δ (J2000)	name		
	(dd-mm-yy)	(hh mm ss)	($^\circ$ $'$ $''$)		(arcmin)	(mJy/beam)
1	01-03-00	03 33 47.7	–19 29 31.0	N 1359	0	1.8
2	27-10-00	03 35 01.4	–24 55 58.0	N 1371	0	1.3
3	27-10-00	03 37 28.3	–24 30 05.0	N 1385	0	1.3
4	15-12-00	03 22 06.5	–15 24 00.0	N 1309	0	1.7
5	03-05-01	03 24 25.6	–21 32 39.0	N 1325	0	1.9
6	06-05-01	03 23 25.1	–19 17 04.0	S 0321.2-1929	0	1.3
7	17-05-01	03 54 33.4	–20 28 14.2	N 1482	2.3	1.0
				N 1481	2.8	1.1
				E 549-G035	8.9	1.4
8	18-05-01	03 40 34.4	–18 30 23.0	A 548-110-078 ($\times$)	4.6	1.0
				N 1407 ($\times$)	6.9	1.1
				I 0343 ($\times$)	7.5	1.1
				A 548-108-069 ($\times$)	8.6	1.1
9	19-05-01	03 27 02.3	–21 16 05.7	N 1332 ($\times$)	4.1	1.1
				E 548-G016 ($\times$)	5.6	1.1
				N 1331 ($\times$)	5.9	1.1
10	20-05-01	03 45 02.9	–18 15 58.0	N 1440 ($\times$)	0	0.9
11	21-05-01	03 35 14.6	–20 22 25.0	N 1370 ($\times$)	0	0.9
12	22-05-01	03 36 39.1	–20 54 08.0	N 1377 ($\times$)	0	0.9
13	16-06-02	03 29 31.7	–17 46 43.0	N 1345	0	1.5
14	16-06-02	03 32 19.3	–17 43 07.0	U 077	0	1.4
15	17-06-02	03 35 37.3	–21 17 39.1	I 1962	0	0.9
				E 548-G049	5.1	1.1
16	17-06-02	03 23 47.2	–19 45 15.0	U 068	0	0.9
17	18-06-02	03 41 13.9	–21 41 48.5	N 1414	4.0	0.9
				N 1422	4.1	1.0
18	20-06-02	03 40 56.8	–22 38 24.5	E 482-G031 ($\times$)	3.6	0.9
				N 1415	4.5	0.9
				N 1416 ($\times$)	4.9	0.9
19	22-06-02	03 29 21.1	–22 12 43.9	E 548-G025 ($\times$)	6.2	1.2
				N 1347	6.3	1.2
20	23-06-02	03 33 26.5	–23 42 41.0	I 1952	0	1.2
21	23-06-02	03 33 34.5	–21 30 58.7	I 1953	2.8	1.4
				E 548-G036	3.3	1.4
22	24-06-02	03 27 35.3	–21 13 42.0	E 548-G021	0	0.9
23	24-06-02	03 37 52.2	–19 00 30.0	N 1390	0	1.1
24	26-06-02	03 41 15.0	–23 50 10.0	E 482-G035	0	1.2
25	26-06.02	03 48 14.1	–21 28 28.0	E 549-G018	0	1.4
26	27-06-02	03 40 31.4	–19 24 40.0	E 548-G065	7.3	1.1
				E 548-G072	7.3	1.3
				E 548-G064 ($\times$)	7.5	1.3
27	27-06-02	03 42 57.3	–19 01 12.0	E 549-G002	0	1.0
28	28-06-02	03 41 00.3	–19 27 19.0	E 548-G077 ($\times$)	0	1.2
29	28-06-02	03 43 35.5	–16 00 52.0	M -03-10-041	0	1.2
30	29-06-02	03 33 02.2	–24 07 58.0	E 482-G005	0	1.1
31	29-06-02	03 36 53.9	–24 54 46.0	E 482-G013	0	1.1

Notes: (1) The bandwidth was 8 MHz except for pointings 5 and 6 where it was 4 MHz and for pointing 4 it was 2 MHz. Therefore, the velocity resolutions were $\sim$ 13.4 km s^{-1} for all except for N 1325 and S 0321.2-1929 where it were $\sim$ 6.7 km s^{-1} and for N 1309 it was $\sim$ 3.3 km s^{-1} .
(2) The on-source integration time for observation was $\sim$ 3 hours except for pointings 5,6,7,8,9 where it was $\sim$ 7 hours.
(3) The centre frequency was 1412.6 MHz except for pointing 1 (1408.0 MHz), pointings 2 and 3 (1414.0 MHz), pointing 4 (1410.0 MHz), pointing 5 and 6 ($\sim$ 1413 MHz) and pointing 7 (1412.0 MHz).
(4) The column with the heading 'Separation' indicates the angular separation between the pointing centre and the galaxy.
(5) The $FWHM$ of the image cubes was $20'' \times 20''$ except for N 1309 and N 1325 where it was $25'' \times 25''$ and for N 1371, E 482-G031, N 1415, and N 1416 it was $30'' \times 30''$.
(6) A cross against the galaxy name indicates an H I non-detection.

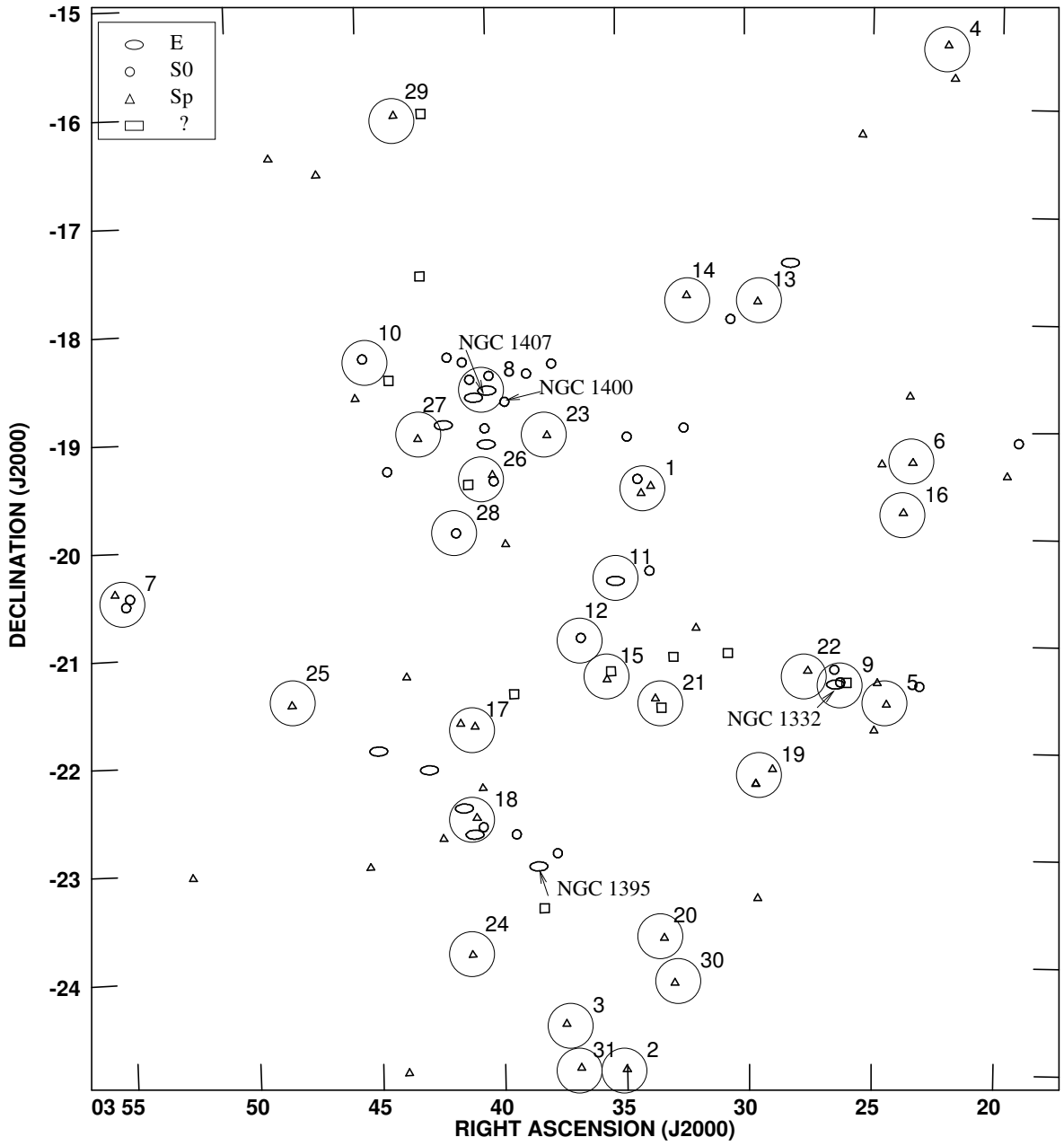

Figure 3.1: Locations of the H I observations. The bigger circles correspond to the $FWHM$ of the GMRT beam ($\sim 24'$) at 1.4 GHz. The pointings in the month of November 2001 for which no useful images could be constructed are not shown here. Details of each pointing are given in Tab. 3.1.

optimization is achieved through fourteen of the thirty dishes being located more or less randomly in a compact central array in a region of about 1×1 square kilometer, and remaining sixteen dishes being spread out along the 3 arms of an approximately 'Y' shaped configuration over a much larger region. The longest interferometric baseline is $\sim$ 25 km and the shortest baseline is $\sim$ 100 m. The locations of the GMRT antennas are marked in Fig. 3.2.

The correlations of the radio signals from all 435 possible pairs of interferometers or baselines are carried out in a digital FX type (Fourier-transform followed by Multiplication) correlator. The correlation is performed over 128 channels for each baseline and each of the two polarizations, horizontal and vertical for the L-band, and, right and left circular for other frequency bands. The spectrum from an FX correlator does no suffer from Gibbs ringing phenomena. In GMRT, the maximum sampling rate is 32 MHz which limits the maximum bandwidth to 16 MHz in each of the polarizations. The correlator can be programmed to use every 2^n (n=0,1,2,3,4,5,6,7) sample thereby effectively increasing the sampling interval, and hence, reducing the bandwidth. The total base-band bandwidth can be selected in steps of 2 from 62.5 kHz to 16 MHz. The channel resolution ($FWHM$) is about the same as the channel width.

3.4 Data acquisition and reduction

The Eridanus group can be observed with the GMRT for $\sim$ 8 hours in a given day. Often, two galaxies were observed in each day of observations. The observing strategy was optimized to get a uniform distribution of the visibilities in the (u, v) plane. The two galaxies were observed alternately for 15-20 minutes each, followed by $5-7$ minutes of observations of secondary calibrators to calibrate the complex gains of the antennas. This cycle was repeated and a total of 3-4 hours of observing time was spent on each galaxy. 0240-231 ($S_{20\ cm} \sim 6.3$ Jy) and 0409-179 ($S_{20\ cm} \sim 2.2$ Jy) from the VLA (Very Large Array) calibrator list were used as secondary calibrators. 0240-231 is classified as a point source calibrator for all the four VLA configurations and 0409-179 is resolved at baselines longer than 10 km.. 0137+331 (3C 48) and 0542+498 (3C 147) were used as primary calibrators. 3C 48 is resolved at baselines longer than 8 km with a total 20-cm flux density of 16.5 Jy, and 3C 147 is resolved at baselines longer than 10 km with a total 20-cm flux density of 22.5 Jy. 3C 48 was observed in the beginning and 3C 147 was observed at the end of each observing run for 20-30 minutes. The flux density of the primary calibrators were estimated at the observing frequency using the spectrum of these sources observed in 1999.2 epoch with the VLA. The data analyses and imaging were carried out using the *Astronomical Image Processing System (AIPS)* developed by the *National Radio Astronomy Observatory (NRAO)*.

The data (visibilities) were collected in the LTA (*Long Time Accumulation*) format which is the native format for the GMRT data. The LTA data was converted to FITS (*Flexible Image Transport System*) format for subsequent processing. Visibilities were averaged in bins of 16*second*. The data were inspected online using the softwares developed at GMRT. The auto-correlation data from antennas were monitored. This data enables one to quickly locate the intermittent problems (e.g., failure of antennas, variations in the band-shape etc.) during observations. A few antennas showed fast variation in their band-shapes on the time scales of a few minutes which were flagged. The cross-correlations were normalized with the geometric mean of instantaneous auto-correlations of the two antennas at each integration time. This normalization is supposed to take care of system gain variations. During the period of observations, continuous monitoring of the system temperature was not enabled. Therefore, if the system (receiver + ground + sky) temperature varies in different regions either due to variations in the sky temperature or ground pick-up, one needs to make corrections in the flux densities of the sources observed in different regions of the sky or over longer periods. Usually at L-band, the variations in the ground and in the sky temperature are negligible as compared to the system temperature. At L-band, the sky temperature is typically in the range $4-8$ K at high Galactic latitudes ($l > 10^\circ$) toward the anti-centre directions where Eridanus galaxies and both primary and secondary calibrators are. Therefore, for the present observations, no significant corrections were needed.

The data were flagged for the antennas having low gains, for time ranges where data were corrupt, and at low elevations (usually $< 25^\circ$) where gains of antennas drop significantly (down to 50% for some antennas) compared to that at higher elevations. The flux densities of the secondary calibrators were estimated by boot-strapping the flux densities of the primary calibrators. The data on the target galaxies were calibrated by interpolating the complex gains determined using the secondary

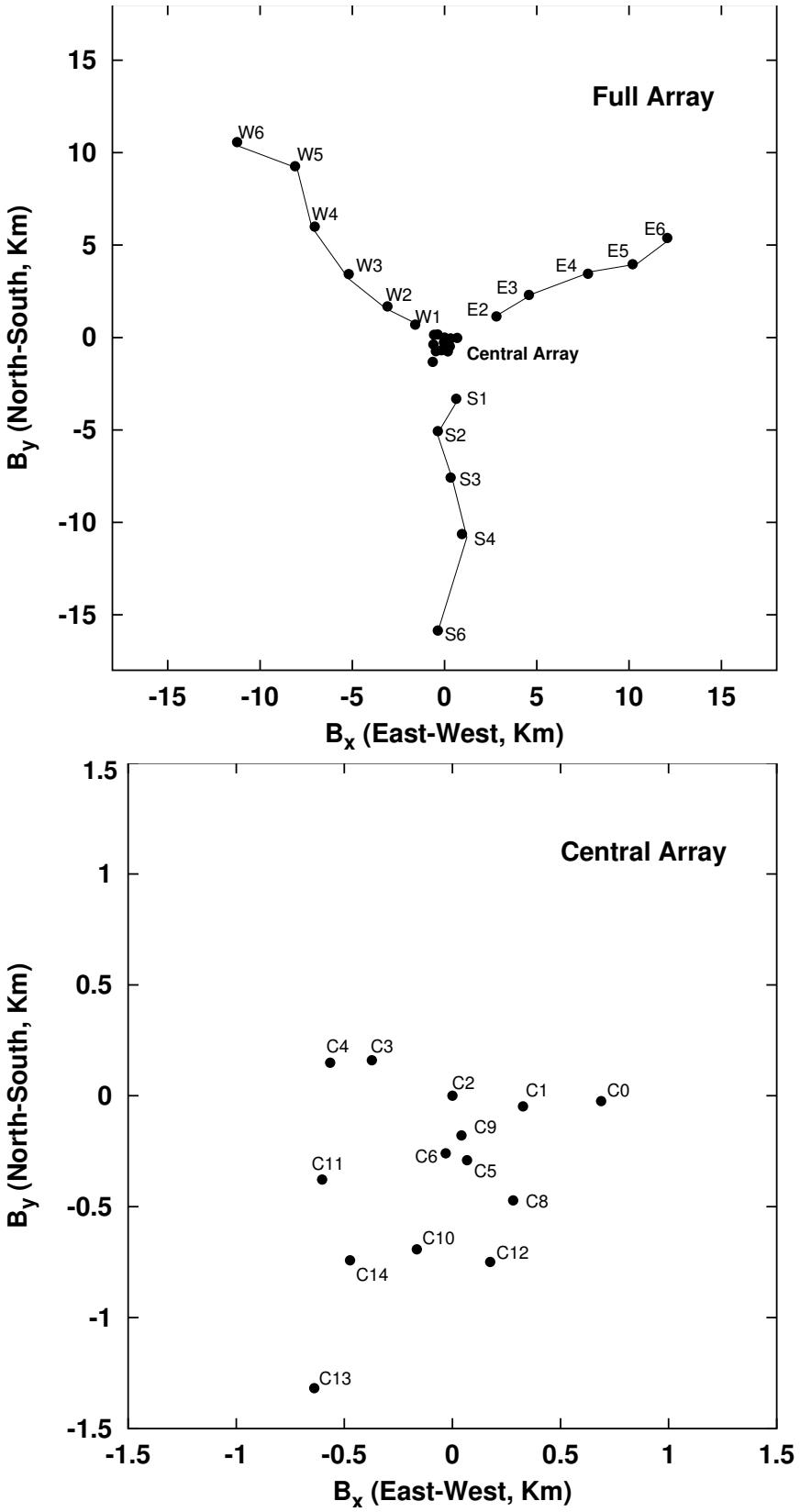

Figure 3.2: The locations of the GMRT antennas. The site is located near Pune, India at longitude 74° .05 E, latitude 19° .092 N, and height $\sim$ 650m above the MSL.

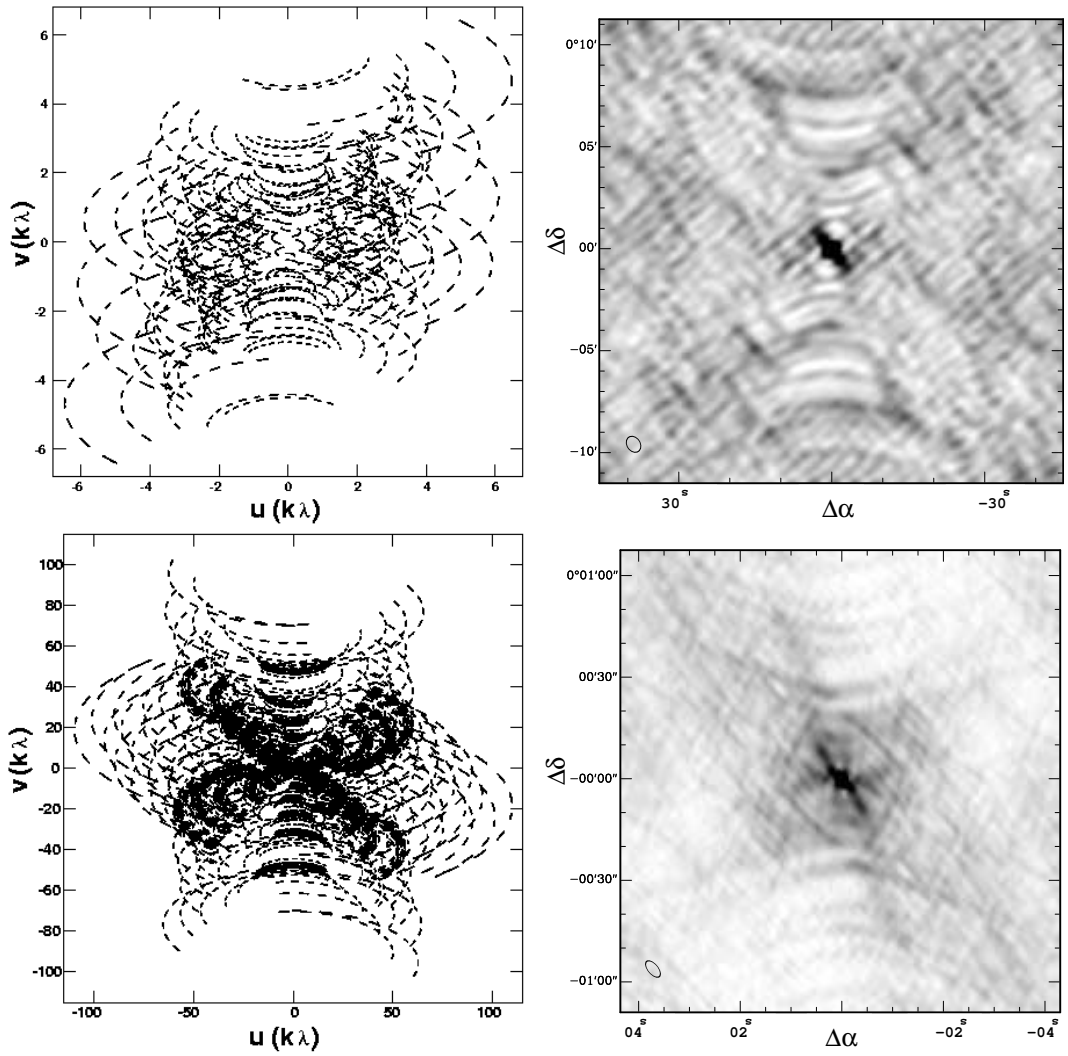

Figure 3.3: The (u, v) sampling of a source of unit flux density at the phase centre in the Fourier plane (left) and its Fourier transform (right). The transformed images (right) are also called the dirty beam. In a given day, two sources were observed at regular intervals of 15–20 minutes each with a gap of 5–7 minutes for calibrations. The top two images are for a (u, v) sampling within the central square and the bottom images are for a (u, v) sampling with the full GMRT array for a source at $\delta = -20^\circ$ and for an hour angle range of ± 4 hr from the zenith with total integration time on each source as ~ 4 hr.

calibrators. Since the spectral responses of filters are not flat, the initial calibration is carried out using a four channel averaged (u, v) data set. It was found that in most antennas, the phases across the channels vary less than 10 degrees across 4 to 6 channels. This channel averaged data set increases the signal to noise ratio for the primary calibration without leading to de-correlation due to phase averaging. The spectral response of the antennas were determined using both the secondary and the primary calibrators, and, an averaged spectrum was used to correct the band shape. An initial H I spectrum was generated using the AIPS task '*POSSM*' at spatial frequencies below 2kλ at the locations of galaxies in the field of view. This range of spatial frequency enables most of the H I signal to be detected in the H I spectrum. This spectrum is obtained to find out which channels have H I emission. The gains start declining significantly after 110th channel. The first 1-3 channels are generally corrupted in the filter response. Therefore, the data were used between channels 3 – 115.

A continuum data set was generated by averaging the channels devoid of H I line emission. The continuum images were made using this channel averaged data and was used for the self-calibration. Several iterations of phase self-calibrations were performed to improve the dynamic range in the images. The final best fit self-cal solutions were applied to the each channel in the line data. Afterwards, the continuum emission was subtracted from the line data using the AIPS task '*UVSUB*' and '*UVLIN*'. The self-calibrated and continuum subtracted line data were used to make image cubes. The image cubes were made at different resolutions by selecting appropriate (u, v) ranges and tapers. Finally, cubes at $20'' - 30''$ (high resolution cube) and $\sim$ 50" (low resolution cube) were produced.

3.5 Image analyses

The images were analysed in the *Groningen Image Processing System (GIPSY)* developed by the *Kapteyn Institute, Groningen*, the *KARMA* visualization tool and *AIPS*. The cubes were *CLEANed* for emission above 3 times the rms. The images were corrected for the attenuation due to primary beam response. The shape of the primary beam of a GMRT antenna at 21 cm wavelength is approximated by a Gaussian of $FWHM \sim 24'$. The cubes were regridded to a pixel size of $4''$ and the co-coordinates were transformed to the J2000 epoch. Since the angular resolution varied by a few arcseconds in different cubes, all high resolution cubes were convolved to a common resolution of $20'' \times 20''$. The image cubes were inspected visually by running a movie of channel images to identify H I signal. Some cubes for larger galaxies were convolved to $25''$ or $30''$. The channel rms of $\sim$ 0.7 mJy beam^{-1} was obtained. The typical 5σ column density sensitivity in the $20''$ images is 1×10^{20} cm^{-2}. The cubes are sensitive (5σ) to detect a galaxy of H I mass 1.2×10^7 M$_\odot$ for an H I line-width of 50 km s^{-1}.

3.5.1 Total H I maps

The zeroth and first order moment maps are generated at both low ($50''$) and high ($20'' - 30''$) resolutions. The moment zero map or the total H I image is obtained by summing the H I images in different channels. The cubes are first blanked to separate the H I signal from the noise before adding the channels. The blanking can be done in several ways. The total H I image depends on the blanking procedure (Rupen 1999). The simplest method is to blank pixels below a certain level. Since H I is a low surface brightness feature, a higher cutoff (e.g., 5σ) can make total H I images patchy while a low cutoff (e.g., 3σ) can often make images noisy. The low surface brightness nature of H I emission makes it difficult to separate low level signal from the noise. A hybrid approach has been shown to be effective in overcoming this problem (e.g, Rupen 1999). This approach involves masking of noise via smoothing the cube. Although the moment maps are still estimated using the un-smoothed cube in this approach. The advantage of smoothing the cube while blanking is following. The H I signal spreads over several channels at a given pixel location in the image due to the finite beam size and large H I line-width compared to the channel resolution. The spectral smoothing will, therefore, increase the signal to noise ratio for the H I emission at a given pixel location. In the present case, a boxcar spectral smoothing of 3 channels and a Gaussian spatial smoothing of 3 pixels was applied. The synthesised beam has five pixels of sizes $4'' \times 4''$. The smoothed images have typical rms of 0.4 mJy beam^{-1}. The pixels to be summed were identified from the smoothed cube if the H I emission was above 3σ in those pixels. However, the original data cube was used to obtain the total H I image

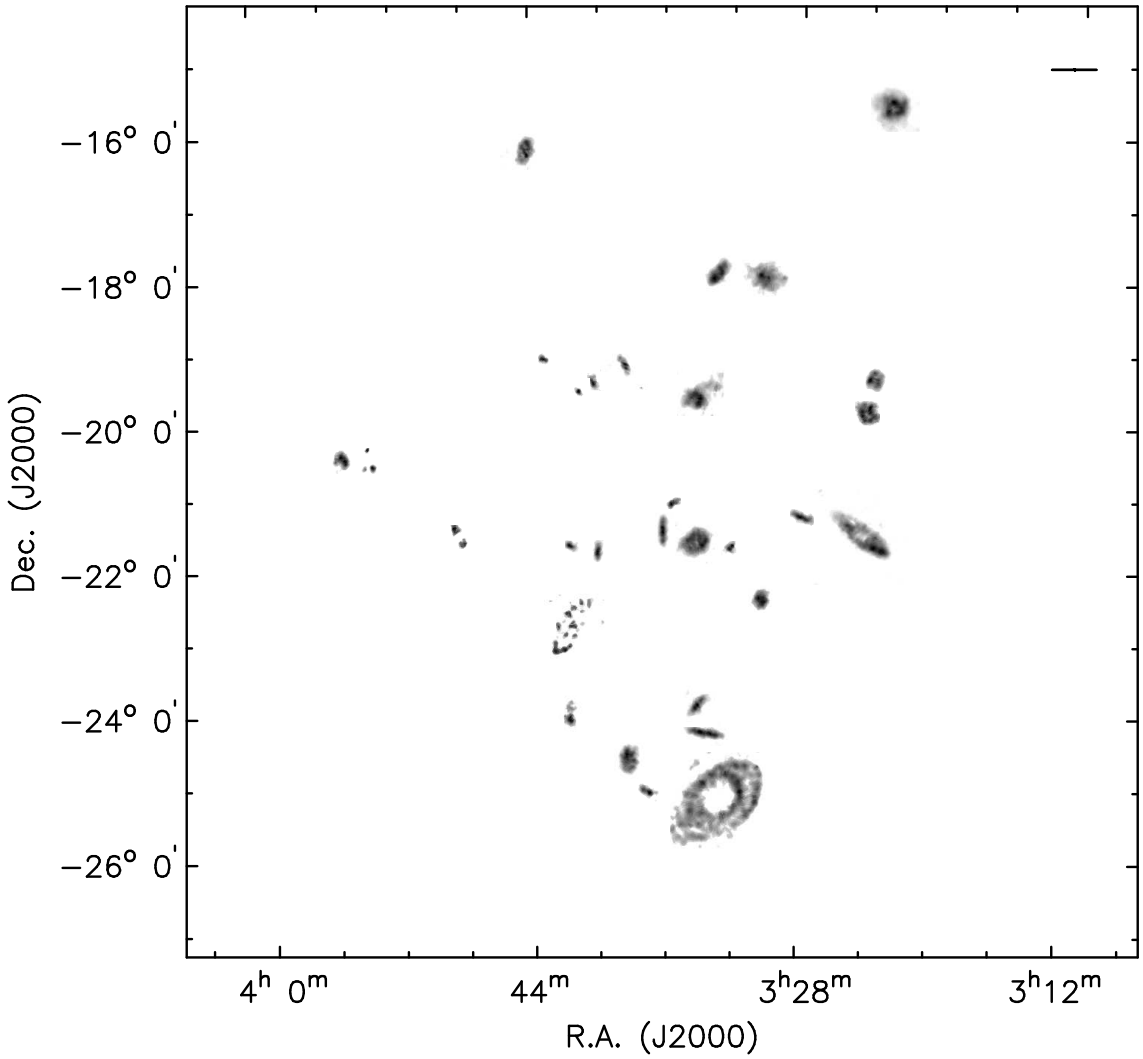

Figure 3.4: A collage of integrated H I maps of galaxies from GMRT. The individual galaxies are enlarged by $\sim$ 10 times their original size. The actual positions of some galaxies are displaced to avoid overlap. A bar on the upper right hand corner indicates a scale of 20 kpc for the enlarged sizes of the galaxies, otherwise, 1° corresponds to a linear dimension of $\sim$ 400 kpc. The maps are sensitive down to an 5σ column density of $N_{\rm H\,I} = 10^{20}$ cm^{-2}.

by summing the emission over those identified pixels. The intensity units (mJy beam^{-1}) at a location (α, δ) are converted to the column density units (cm^{-2}) using the relation:

$$N_{HI}(\alpha,\delta) = \frac{1.1 \times 10^{21} cm^{-2}}{\theta_a \times \theta_b}\, \delta v \sum_{j=1}^{N_{chan}} S_j(\alpha,\delta) \qquad (3.1)$$

(using eqn. 3.38, Spitzer 1978); where θ_a and θ_b are the full widths at half maxima ($FWHM$) of the synthesised beam along the major and minor axes respectively measured in arcsecond. S_j is the H I flux density (mJy beam^{-1}) in the channel j and δv is the velocity resolution in km s^{-1} . The H I gas is assumed to be optically thin. A collage of integrated H I maps of galaxies from the GMRT is shown in Fig 3.4 as grayscale and in Fig 3.5 . The individual galaxies are enlarged by $\sim$ 10 times in this figure. The actual positions of some galaxies are displaced to avoid overlap.

3.5.2 H I velocity fields

A conventional way of deriving the velocity field is to compute the intensity-weighted first order moment of the H I distribution at different velocities. The first order moments can be estimated

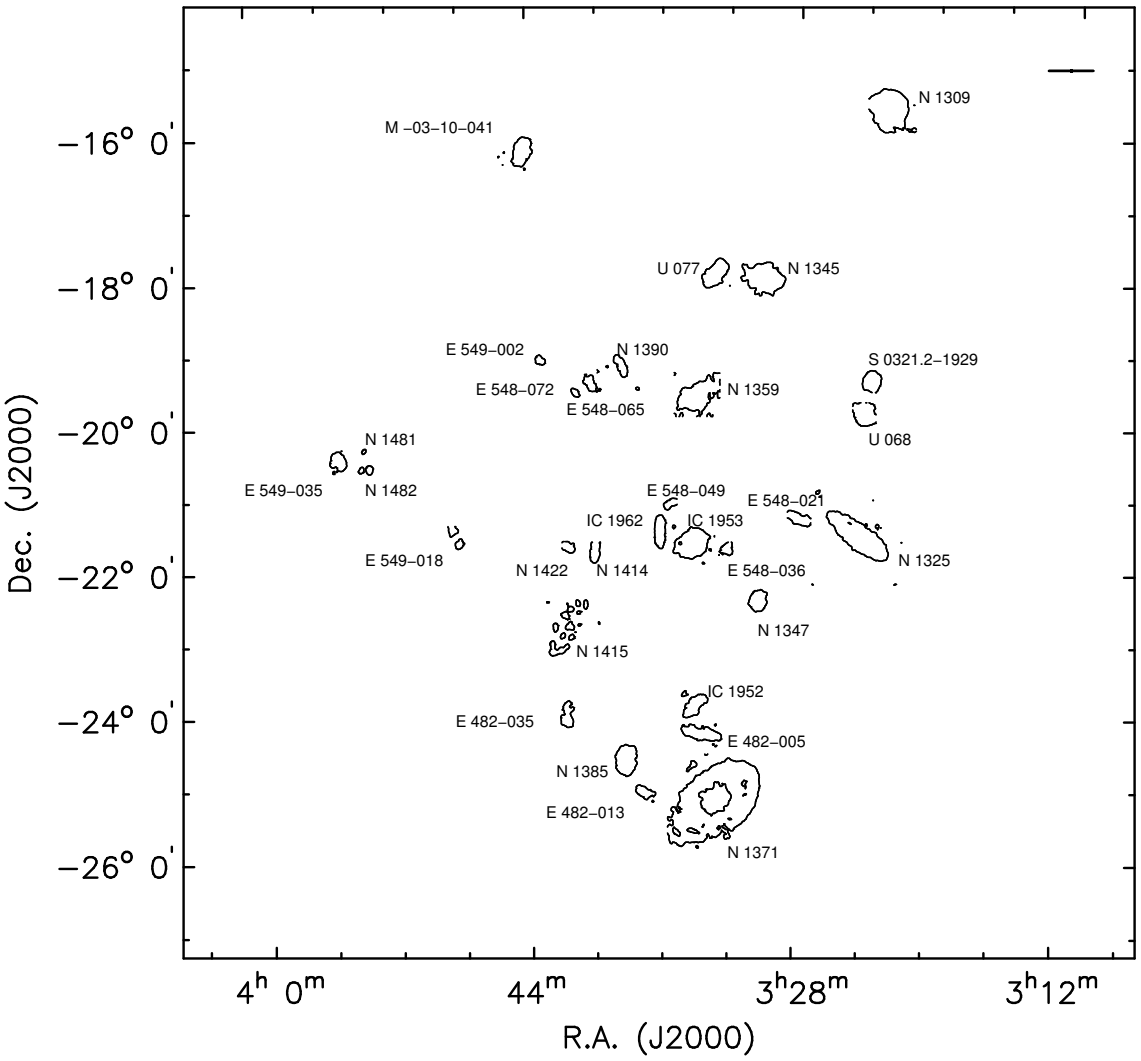

Figure 3.5: The H I detected galaxies in the Eridanus group shown in the HI contour image. The contour level is at $N_{HI} = 10^{20}$ cm^{-2}. The individual galaxies are enlarged by $\sim$ 10 times their original size. The actual positions of some galaxies are displaced to avoid overlap. A bar on the upper right hand corner indicates a scale of 20 kpc for the enlarged sizes of the galaxies, otherwise, 1° corresponds to a linear dimension of $\sim$ 400 kpc.

using the following relation -

$$\bar{v}(\alpha,\delta) = \frac{\sum_{j=1}^{N_{chan}} v_j S_j(\alpha,\delta)}{\sum_{j=1}^{N_{chan}} S_j(\alpha,\delta)} \tag{3.2}$$

where $\bar{v}$ is the velocity at location (α,δ), v_j is the velocity at channel j, and S_j is the H I flux at channel j. N_{chan} is the total number of channels over which H I emission from a galaxy is detected.

There is an alternate way to estimate $\bar{v}(\alpha,\delta)$ via carrying out a fit to the H I profile (flux vs. velocity) at a given pixel. These profiles are usually asymmetric depending upon the kinematics of H I along the line of sight and due to the beam smearing caused by the finite size of the synthesized beam. The broadening and asymmetry will depend upon the H I distribution in the galaxy. The effect of beam smearing will be more pronounced in the edge-on systems. As a result of the asymmetry and broadening in the H I profile, a single Gaussian fit may not give a satisfactory result. Unfortunately, multi-component Gaussian fit could not be carried out as the signal to noise ratios at each pixel were not sufficient.

Rupen (1999) has briefly discussed the merits and drawbacks of these two procedures. The first order moment maps are generally noisier than the velocity field maps obtained by a Gaussian fit. This is because the Gaussian fits are not as sensitive to the outliers as a moment map is. Therefore in the present analysis, Gaussian fits were used to construct the velocity field maps. It should be noted that both the procedures to obtain the velocity field will underestimate rotation velocities at locations of steep velocity gradients. The flat portions of the rotation curves will remain unaffected.

3.5.3 Global H I profiles

The integrated H I flux density as a function of velocity gives the global H I profile as would have been obtained from a single dish observation. The low resolution ($50''$) cubes are used to obtain the global profiles as the low resolution cubes will be more sensitive to any diffuse emission. The entire region of the H I emission as seen in the total H I map (zeroth moment map) at low resolution was used to integrate the flux density. The H I mass is estimated using the following relation:

$$M_{HI}(M_\odot) = 2.36 \times 10^5 D^2\ \delta v \sum_{j=1}^{N_{chan}} S_j \tag{3.3}$$

where D is the distance in Mpc, S_j is the integrated flux density in Jy in the spectral channel j of velocity width δv. The distance is taken as 23 Mpc. The H I flux integral of some galaxies obtained from GMRT is compared in Fig. 3.6 with the HIPASS data and other single dish data. Some galaxies with higher flux integral in the single dish data show significantly less flux in the GMRT. The H I disk sizes of these galaxies are among the largest in our sample. We believe that the loss of flux for large galaxies in the GMRT images is due to inadequate sampling of shorter (u,v) spacings in the GMRT.

3.5.4 H I line-width

The H I global profiles often peaks at the two extreme ends of the rotation velocities of galaxies. The detailed shape of H I profile depends on the rotation curve, the inclination and the H I distribution in the galaxy. The H I line-widths are broadened from their true values due to random motions in the H I gas and the finite spectral resolution. The H I line-width is a crucial parameter for studying the Tully-Fisher (TF) relation. Most of the TF studies still use the H I line-widths obtained from single dish observations because of the simplicity of such observations. The synthesis data on the Eridanus group of galaxies provides an opportunity to compare the corrected H I line-widths obtained from the single dish H I profiles with those obtained from the H I rotation curves.

For cases in which double-peaked H I profiles are seen, H I line-widths are estimated at 20% (W_{20}) and 50% (W_{50}) levels of the peak intensities at the two ends of the H I profiles. The locations of the two peak intensities are estimated separately using Gaussian fit to the profiles. Various correction procedures are described to correct the widths for the finite spectral resolution (Bottinelli et al. 1990) and for random and turbulent motions in galaxies (e.g., Tully & Fouque 1985). These corrections are determined empirically.

Bottinelli et al. (1990) derived an empirical relation to correct for the instrumental broadening. They convolved the H I profile progressively with coarser velocity resolutions for a model galaxy, and

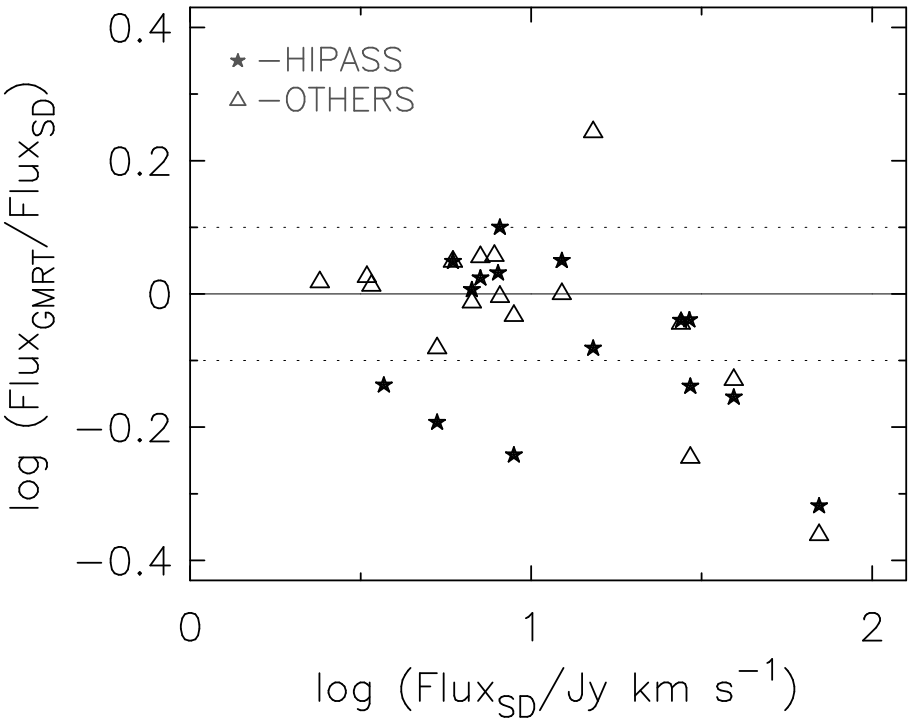

Figure 3.6: A comparison of the H I flux integrals from the GMRT observations with that from the published single dish data (others) and the HIPASS data on some galaxies in the Eridanus group. The dotted lines indicate 25% uncertainties in the flux.

determined the broadening. They advocated for a linear relationship between the channel resolution and the instrumental broadening. They estimated a correction of $\delta W = 0.55 \times \delta V_i$ for W_{20} and $\delta W = 0.13 \times \delta V_i$ for W_{50} for a instrumental resolution δV_i. For $\delta V_i = 13$ km s^{-1} , the correction is ~ 7 km s^{-1} for the W_{20} and ~ 2 km s^{-1} for the W_{50}.

It is expected that a linear summation of rotation and random motions is appropriate to get the observed width for the case where the intrinsic width is almost boxy (i.e., in giant galaxies) but a summation in quadrature will be required in the case of dwarf galaxies where the solid body rotation together with the radial distribution of the H I gas will lead to an almost Gaussian profile. An empirical composite relation for both giant and dwarf galaxies is given by Tully & Fouque (1985). According to this relation, the width due to the rotation motion W_R and the width due to random and turbulent motions W_t, the observed width W_l can be given by the following relation -

$$W_l^2 = W_{R,l}^2 - W_{t,l}^2 \left(1 - 2e^{-(W_l/W_{c,l})^2}\right) + 2W_l W_{t,l} \left(1 - e^{-(W_l/W_{c,l})^2}\right) \quad (3.4)$$

where the subscript l refers to the level (20%, or 50%) at which the widths are estimated. The $W_{t,l}$ is estimated as $2k_l\sigma$ from the dispersion of the H I gas (σ) due to random and turbulent motions. The constant factor k_l is 1.80 at 20% level and 1.18 for the 50% level for a Gaussian profile. The value of σ is taken as 6 km s^{-1} . $W_{c,l}$ is a parameter which defines the transition region for the linear to a quadratic sum. The Eqn. 3.4 does a linear subtraction if $W_l > W_{c,l}$ and a quadratic subtraction if $W_l < W_{c,l}$. The values of $W_{c,l}$ are determined empirically as 120 km s^{-1} for the 20% level and 100 km s^{-1} for the 50% level by Tully & Fouque (1985).

3.5.5 Radial H I density profiles

The total H I maps were used to estimate the radial mean H I surface density profiles by azimuthally averaging the column densities in concentric elliptical annuli. The axial parameters of the ellipses were obtained from the tilted ring fit to the velocity field. The elliptical annuli were sampled at intervals of 10″ to get two points in one synthesised beam of 20″. The widths of the annuli were kept fixed at 10″. The average radial profile in each annulus is scaled by the ratio of the total H I mass to the summed column density in all annuli to obtain the H I mass surface density. The profiles are

corrected for the projection effects to obtain the face-on mass surface density in units of $M_\odot$ pc^{-2}. The profiles can be quite uncertain in high inclination galaxies where some flux density from the lower radii along the minor axis will be included at larger radii due to finite spatial resolution. Also, the profiles will artificially extend to larger radii near the outer edge of the H I disk due to the finite angular resolution.

3.5.6 Rotation curves

The rotation curves are derived using the tilted ring model (cf. Begeman 1989). The basic methodology of this model is following. The model assumes gas to be in circular orbits. The position angle and the inclination of the H I disk are allowed to vary with radius. The fitting procedure generally involves estimation of 5 unknowns, *viz.*, dynamical centre (X,Y), systemic velocity (V_{sys}), position angle (PA) of the major axis, inclination (INCL) and circular rotation velocity (V_{rot}), and optionally the expansion velocity V_{exp}. The observed radial velocity V(x,y) at rectangular sky coordinate (x,y) at a radius r can be given by -

$$\begin{aligned} V(x,y) &= V_{sys} + V_{rot}\ cos(\theta)sin(INCL) + V_{exp}\ sin(\theta)sin(INCL) \\ &where \\ cos(\theta) &= \frac{-(x-X)sin(PA) + (y-Y)cos(PA)}{r} \\ sin(\theta) &= \frac{-(x-X)cos(PA) + (y-Y)sin(PA)}{r\ cos(INCL)} \end{aligned} \tag{3.5}$$

The V_{exp} term was not fitted in the present analysis and was kept fixed at zero. This term can be useful to estimate any non-axisymmetric term in the velocity field. The velocity fields at $20''$ resolution obtained via Gaussian fit were used in the analysis. The iterative procedure described by Begeman (1989) is used to estimate the remaining five parameters. The velocities are averaged in elliptical annuli of width $10''$ and extracted as a function of the azimuth angle at radii in increments of $10''$. The rotation curves in the receding side and the approaching side were fitted separately.

The iterative scheme used here is described below:

Estimating dynamical centre (X,Y) and systemic velocity V_{sys} :

The centre velocity determined from the H I width or the optical velocity of the galaxy is used as the initial guess for the systemic velocity. The centre, the position angle and the inclination estimated from an elliptical fit to the optical isophotes are taken as an initial guess. The first iteration is started with fixing the inclination and the position angle and fitting the centre and the systemic velocity. If the velocity field is symmetric, the fitted value of the dynamical centre and the systemic velocity should be similar for all the rings. However, often galaxies do not have symmetric velocity fields due to asymmetric warps or kinematical lopsidedness and different results may be obtained in each ring. An overlay of the velocity field contours over the optical image helps in deciding the quality of the fit. For a galaxy with no warp, the velocity field line should run straight along the minor axis and the line joining the cusps of the iso-velocity contours of identical rotation velocity at the two halves of the galaxy should trace the direction of the major axis. The intercept of the major axis with the minor axis will be the dynamical centre.

If a galaxy has a warp, the velocity field will show a characteristic S shaped or integral sign shaped structure. Often by visual inspection of the velocity field, a sufficiently good estimate can be obtained to decide whether the fitting routine is giving a reasonably good fit or not. It was found in some cases that the dynamical centre was not coincident with the optical centre (e.g., in IC 1953). The centre and the systemic velocity were computed as unweigthed mean of values in all the rings for which satisfactory solutions were found. Once the centre and the systemic velocity are determined, these values are held fixed at all radii during the successive iterations.

Estimating position angles :

The position angle is determined at each annulus and held fixed in the subsequent iterations. The Incl. was kept fixed and Vrot was allowed to vary during this step. The variations in position angle with radii can be inferred from the visual inspection of the velocity field. If a galaxy is warped, the position angle varies monotonically starting at certain radii and often becomes constant at large radii. Also, warps result in variations of both the inclination and the position angle simultaneously. For galaxies, where no significant change in the position angle or in the inclination or in both is seen, an average value of the position angle is taken.

Estimating inclination angles :
In this iteration, fit is carried out for the inclination and the rotation velocity. The previously determined parameters (centre, systemic velocity, and PA) are kept fixed. Galaxies with inclinations below 45° are not suitable for the tilted ring fits (Begeman 1989). In such cases, optical inclination angle is taken. If the inclination is found to be more or less same for all annuli, an average value is taken.
Estimating the rotation velocities :
In the final iteration, all the disk parameters obtained from the previous iterations are kept fixed, and a fit is carried out to obtain the circular rotation velocities at each annulus. The receding and the approaching sides of the galaxies are fitted separately. In this step, a cosine weighting scheme is adopted such that points along the major axis have maximum weight and points along the minor axis have zero weight. In addition, points within ±20 degrees from the minor axis are not used in the fitting procedure. This is due to the fact that the minor axis does not have any information on the rotation velocity, and the points along major axis gives a direct estimate for the maximum projected rotation velocity.

The rotation velocities obtained from the tilted ring fit should be corrected for the effects of beam smearing. The effects of beam smearing are maximum at locations of steep velocity gradients. In this thesis, we are interested in deriving the flat rotation velocities to obtain the Tully-Fisher relation. The flat portions of the rotation curve remain nearly unaffected due to beam smearing. The rotation curve presented in this thesis are not corrected for the effects of beam smearing. Therefore, analysis which are critically dependent on the quality of the rotation curves (e.g., dark matter analysis), these rotation curves should not be used without making an appropriate correction. Such analyses will be presented elsewhere.

3.5.7 H I diameter

The diameters of the H I disks were estimated at a fixed face-on H I surface density of 1 $M_\odot$ pc^{-2}. Due to projection effects, the sensitivities to the face-on H I surface densities were not uniform. Therefore, in some cases the H I diameters were extrapolated to the face-on H I surface density level of 1 $M_\odot$ pc^{-2}. The high resolution ($20'' - 30''$) total H I images were used.

3.5.8 Dynamical mass

An estimation of dynamical mass can be obtained using the rotation velocities obtained from the rotation curves. The total mass within a radius R (kpc) can be derived using the relation $M_{tot}/M_\odot = 2.3 \times 10^5 V_{rot}^2 R/G$, where V_{rot} is the rotation velocity in km s^{-1} . There can be several choices for the radius R, e.g, H I disk radius, optical disk radius, disk scale length etc. We estimate the dynamical mass within the optical radius (i.e. $0.5 \times D_{25}$). The estimates are made only for those galaxies in which flat rotation velocity could be estimated.

3.6 H I properties of galaxies

In this section, some H I properties of the Eridanus galaxies are presented and discussed briefly.

3.6.1 H I and total dynamical mass

The histogram of the H I masses of galaxies detected by GMRT is shown in Fig. 3.7. The lowest H I mass ($\sim 8 \times 10^8$ $M_\odot$) detected is of an S0 galaxy NGC 1481. Some galaxies toward the high mass end in the histogram will have their H I masses underestimated as GMRT seems to have missed some flux in larger galaxies. Due to limited sample size, this plot is of a little statistical significance to estimate the H I mass function. However, it can be notice that there are almost equal number of galaxies in the H I mass range (log) of 8.5 and 9.5. This histogram implies that the H I mass function will be flat over this mass range and will drop at higher values of the H I masses.

The dynamical masses are plotted in Fig. 3.8 as a function of Hubble type. Only those galaxies are plotted where flat part of the rotation curve could be measured. There seems to be a systematic trend in the sense that early type galaxies have on average higher dynamical mass than late type galaxies. This result is consistent with other H I imaging studies (e.g., Broeils & Rhee 1997, Verheijen et al. 2001).

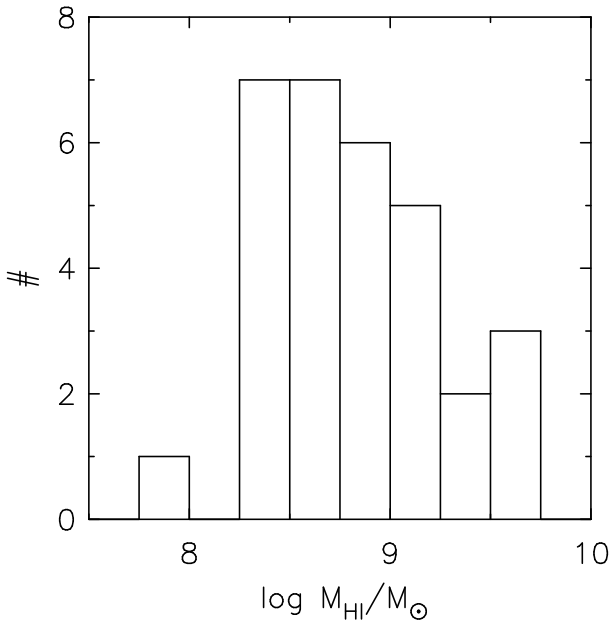

Figure 3.7: The histogram of H I mass in the Eridanus galaxies observed with the GMRT.

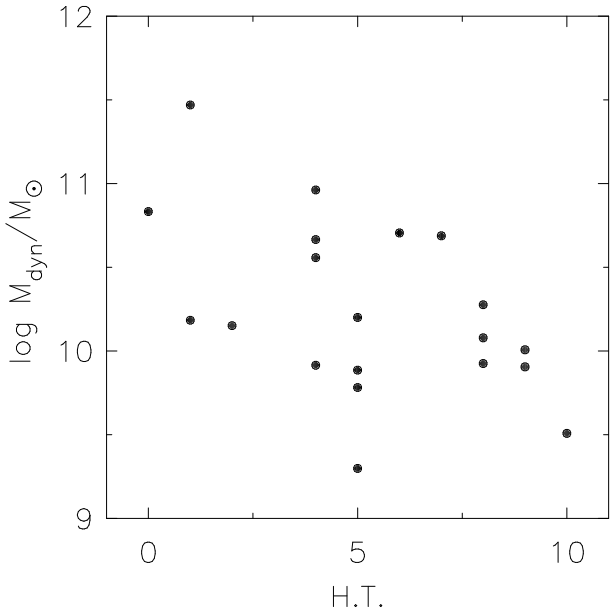

Figure 3.8: Dynamical mass plotted against the Hubble type. The masses are estimated within the optical diameter (D_{25}).

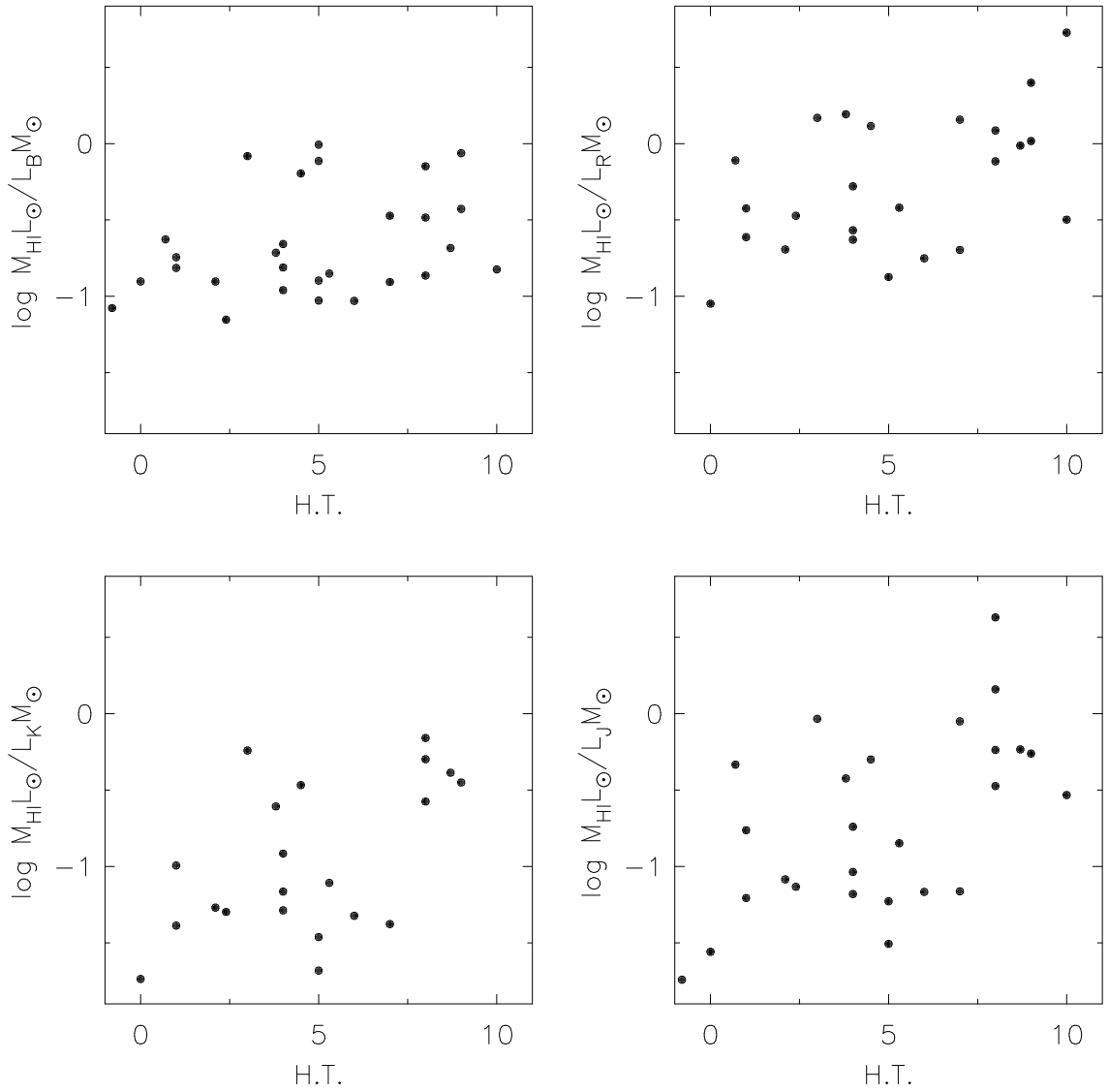

Figure 3.9: The H I mass to luminosity ratio in optical and near-IR bands. There appears to be a trend in the R, and the near-IR bands in the sense that late type galaxies have on average higher values of $M_{\rm H\,I}/L$.

3.6.2 H I mass to luminosity ratio

The ratios of the H I mass to the luminosity in the B, R, J, and K bands are plotted in Fig 3.9 against the Hubble types. The B-band luminosities are estimated using the face-on magnitudes from the RC3 catalog and assuming the Sun's absolute magnitude in the B-band as 5.48. The values of M_{HI}/L_B is in general consistent with that of Broeils & Rhee (1997). No significant trend in the M_{HI}/L ratio is seen in the B-band, however, there appears to be a trend in the R and the near-IR (J & K) bands in the sense that late type galaxies have on average higher M_{HI}/L. This trend in M_{HI}/L in the J and K bands for which the extinction corrections are relatively less significant are entirely consistent with the results from Verheijen & Sancisi (2001) based on the Ursa-major group.

3.6.3 Ratio of H I diameter to optical diameter

The ratio of the H I diameter to the optical diameter (D_{HI}/D_{25}) is plotted in Fig. 3.10 against various properties of galaxies. No significant correlation is seen with the Hubble type, H I mass, and the projected distance to the nearest neighbor. There appears to be a weak trend in the D_{HI}/D_{25} ratio with the galaxy luminosity in the J-band in the sense that the ratios could be higher in luminous

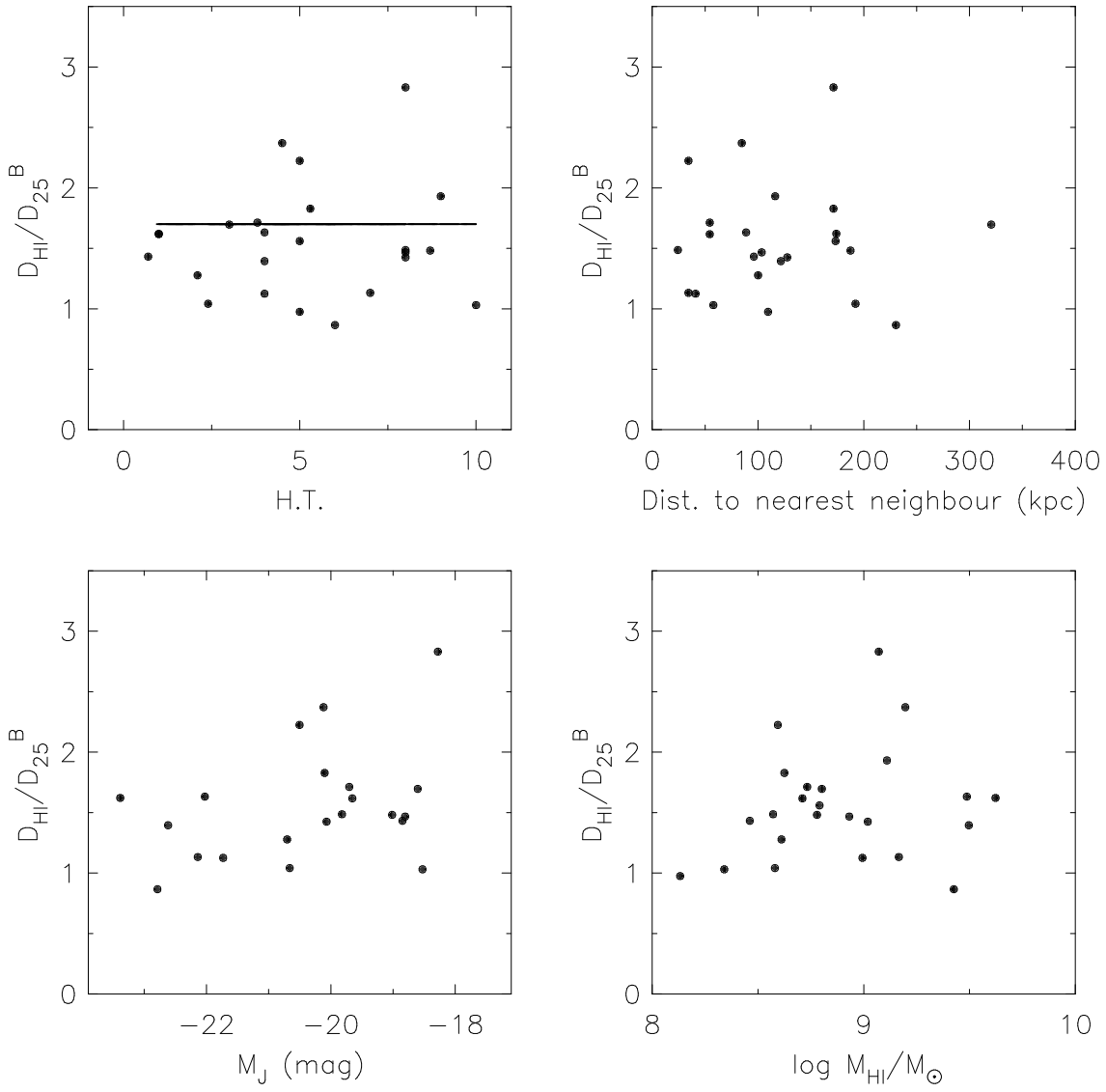

Figure 3.10: The ratio of the H I diameter to the optical diameter is plotted with different properties of galaxies. The mean ratio of the sample is 1.7 ± 0.8. The ratio seems to be independent of the Hubble type and the H I mass. The ratio also seems to be unaffected by the distance to the nearest neighbor. There appears to be a trend with respect to the J-band luminosity.

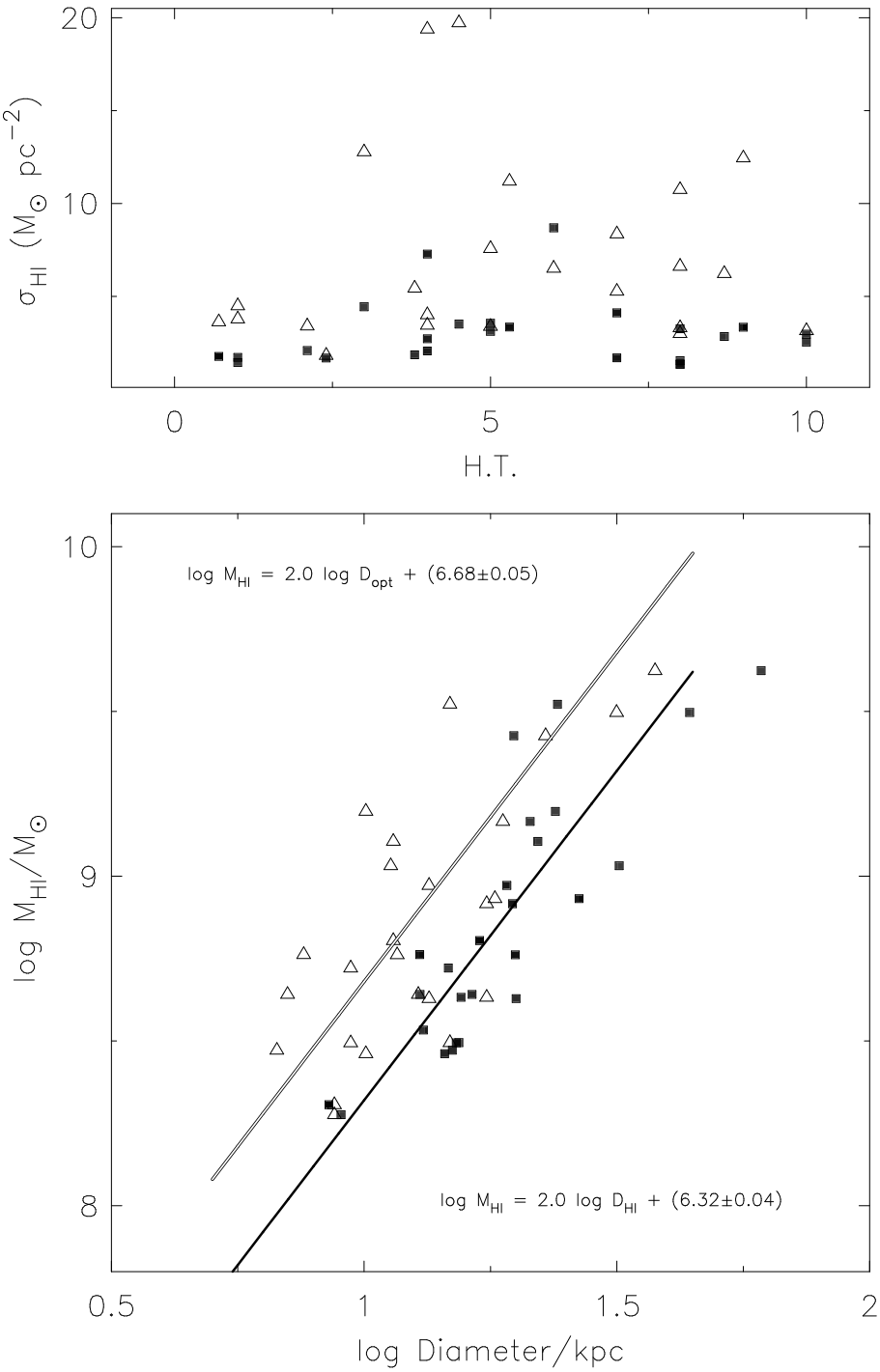

Figure 3.11: (Lower panel) The log of H I mass is plotted (in ordinate) against log diameter (in abscissa) for the H I disks (filled squares) and the optical disks (open triangles). The lines are fits to the data with the equation written on the top left hand corner for the optical diameters and with the equation written on the bottom right hand corner for the H I diameters. The slopes were kept fixed at 2. (Upper panel) The H I mass surface density estimated over the H I disks of galaxies plotted against their Hubble types.

galaxies. This trend is consistent with the results of Verheijen & Sancisi (2001) on the Ursa-Major group of galaxies. However, we do not confirm their result that there is also a similar trend with the Hubble type. The average value and scatter D_{HI}/D_{25} is 1.7 ± 0.8, which is consistent with the value of 1.7 ± 0.5 obtained by Broeils & Rhee (1997).

3.6.4 H I surface density

Tight correlations between log M_{HI} with log D_{HI} and log D_{opt} respectively have been reported (Haynes & Giovanelli 1984, Broeils & Rhee 1997, Verheijen & Sancisi 2001). The latter authors showed that the correlation is tighter with the H I diameter than with the optical diameter with slopes close to 2. The lower panel of Fig. 3.11 shows log M_{HI} for the Eridanus galaxies plotted against log D for both optical and H I diameters. A straight line is fitted with a fixed slope of 2. It can be seen that indeed the H I diameters of galaxies in the Eridanus group are more tightly correlated than the optical diameters with their H I masses.

The upper panel of Fig. 3.11 shows the distribution of the H I mass surface densities ($\sigma_{\rm H\,I} = 4M_{HI}/\pi D^2$) of Eridanus galaxies against their Hubble types. It can be seen that the mass surface densities over the H I disks have less scatter than the mass surface density over the optical disks.

3.7 Summary

GMRT H I observations were carried out for $\sim$ 200 hours on galaxies in the Eridanus group. This data is used in this thesis to study the H I content of the group, Tully-Fisher relations and the radio continuum properties. There is considerable scope to use this data for several other studies. Subsequent studies on the dark matter properties and kinematical properties of gas disks in the Eridanus galaxies will be carried out.

The following conclusions can be drawn from the H I properties of the Eridanus galaxies -

- The early type disk galaxies seems to have higher dynamical mass compared to the late type disk galaxies.
- There appears to be a trend in the R and the near-IR (J & K) bands in the sense that late type galaxies have on average higher M_{HI}/L.
- The average value of $D_{\rm H\,I}/D_{opt}$ is 1.7 ± 0.8 for the Eridanus galaxies is entirely consistent with other H I imaging studies.
- There also appears to be a weak trend in the D_{HI}/D_{opt} ratio with the galaxy luminosity in the J-band in the sense that the ratio could be higher in luminous galaxies.
- The ratio $M_{HI}/D_{\rm H\,I}$ has less scatter as compared to that in the ratio M_{HI}/D_{opt} .

3.8 Table of results & the H I atlas

The results are presented in Tab. 4.2. The description of the entries in the table is following:

Column 1 Galaxy name, Opt. Centre, Radio Centre: The abbreviated names of galaxies with convention used in the Chapter 3. The optical centre is from the RC3 catalog, and the radio centre is that estimated from the tilted ring fit.

Column 2 Type, INCL, PA: The morphological type, inclination, and the position angle.

Column 3 Velocities: The systemic velocities obtained from the tilted ring fit, the global profile fit, and from RC3. All these velocities are Helio-centric.

Column 4 Diameters: The HI diameter (in kpc), B-band optical diameter at B25 mag arcsec^{-2} from RC3, and R-band optical diameter at R25 mag arcsec^{-2} from the UPSO observations.

Column 5 Rotation velocities: The entries in this column are velocity at the last measured point of the rotation curve, velocity at the flat part of the rotation curve, and the velocity as half of the W_{20} from the H I global profile corrected for the broadening due to the velocity resolution and random motions.

Column 6 Masses: The H I mass, the stellar mass from the K-band light assuming M^*/L ratio of 0.6, and the total mass.

Column 7 Mass to light ratios: The ratios of the H I mass to the B-band, R-band, and K-band luminosities.

Column 8 Mean H I *surface density, and ratio of the* H I *diameter to the optical diameter* The mean H I surface density ($M_\odot/pc^2$) over the H I diameter and the optical diameter at B25 mag arcsec^{-2}. The last entry in this column is the ratio of the H I diameter to the optical diameter at 25 mag arcsec^{-2}.

Table 3.2: Results from the GMRT H I synthesis observations

Galaxy Name Opt. centre Radio centre (RA - Dec (J2000))	Type INCL. P.A.	V_{sys} V_{cent} V_{opt} (km/s)	D_{HI} D_{B25} D_{R25} (kpc)	V_{lmp} V_{flat} $W_{50}/2$ (km/s)	M_{HI} M_K M_{total} ($10^9 M_\odot$)	M_{HI}/LB M_{HI}/LR M_{HI}/LK ($M_\odot/L_\odot$)	$\sigma_{HI}(HI)$ $\sigma_{HI}(opt)$ D_{HI}/D_{B25} ($M_\odot/pc^2$)
ESO 482- G 005	SBdm	1923	32	80.2	1.08	0.71	1.34
03 33 02.2 -24 07 58	82	1918	11.3	80.2	–	–	10.7
03 33 2.15 -24 07 58	264	1915	–	79.5	8.423	–	2.83
ESO 482- G 013	Sb	–	12.9	–	0.578	0.83	4.44
03 36 53.9 -24 54 46	63	1850	7.59	–	0.604	1.5	12.8
03 36 53.8 -24 54 46	65	1835	7.17	–	1.11	0.57	1.7
ESO 482- G 035	SBab	1883	16.4	118	0.438	0.13	2.08
03 41 15.0 -23 50 10	49	1884	12.8	118	4.883	0.2	3.4
03 41 14.7 -23 50 11	185	1890	14.8	115	20.78	0.054	1.28
ESO 548- G 021	SBdm	1690	20	87.7	0.425	0.14	1.36
03 27 35.3 -21 13 42	80	1691	13.4	87.7	0.507	–	3
03 27 35.2 -21 13 41.7	64	1668	–	83.3	11.99	0.5	1.49
ESO 548- G 036	S?	–	–	–	0.257	0.13	–
03 33 27.6 -21 33 53	–	1507	6.7	–	4.482	–	7.31
03 33 28 -21 33 55.1	–	1480	–	60.5	–	0.034	–
ESO 548- G 049	S?	1533	14.9	71	0.296	0.34	1.69
03 35 28.1 -21 13 01	71	1533	6.72	–	–	1.4	8.36
03 35 28.4 -21 13 7.01	128	1510	6.27	–	3.93	–	2.22
ESO 548- G 065	SBa	1213	14.4	72.9	0.289	0.24	1.77
03 40 02.7 -19 22 00	80	1243	10.1	–	–	0.78	3.63
03 40 2.53 -19 21 56.8	37	1221	–	64.5	6.214	–	1.43
ESO 548- G 072	S?	2045	8.52	44.3	0.203	0.77	3.56
03 41 00.3 -19 27 19	74	2052	8.74	–	–	–	3.38
03 41 0.795 -19 27 19	51	2034	–	48.0	1.989	–	0.975
ESO 549- G 002	IBm	1110	9	55.9	0.189	0.15	2.97
03 42 57.3 -19 01 12	63	1115	8.74	–	–	0.32	3.15
03 42 57.2 -19 01 11.1	210	1111	–	60.8	3.167	–	1.03
ESO 549- G 018	SABc	1587	15.5	–	0.429	0.094	2.26
03 48 14.1 -21 28 28	56	1576	17.5	–	12.37	0.13	1.79
03 48 14 -21 28 28.9	203	1587	17.5	152	–	0.021	0.89
ESO 549- G 035	Sc	1814	14.7	74.5	0.526	0.98	3.11
03 55 04.0 -20 23 01	56	1768	9.41	74.5	–	–	7.57
03 55 4.39 -20 23 0.92	30	1778	–	81.3	6.057	–	1.56
IC 1952	SBbc	1820	19.7	134	0.825	0.11	2.72
03 33 26.7 -23 42 46	71	1823	17.5	134	9.599	0.23	3.44
03 33 26.4 -23 42 46.1	319	1812	22.4	122	36.12	0.052	1.13

IC 1953	SBd	1863	21.3	150	1.46	0.12	4.11
03 33 41.9 -21 28 43	37	1863	18.8	150	20.97	0.2	5.27
03 33 42.2 -21 28 39.3	129	1867	24.2	142	48.78	0.042	1.13
IC 1962	SBdm	1806	26.6	82.3	0.855	0.33	1.54
03 35 37.4 -21 17 33	80	1811	18.1	–	0.7401	1.2	3.31
03 35 37.8 -21 17 38	358	1806	18.4	69.1	14.26	0.69	1.47
MCG -03-10-041	SBdm	1207	19.2	110	0.938	–	3.25
03 43 35.5 -16 00 52	57	1217	13.4	110	2.112	0.77	6.61
03 43 35.4 -16 0 51.3	343	1215	13.9	109	18.9	0.27	1.43
NGC 1309	SAbc	2134	24.1	164	3.33	0.22	7.28
03 22 06.5 -15 24 00	20	2134	14.8	164	16.44	0.53	19.4
03 22 5.89 -15 23 59.9	210	2135	13.4	168	46.35	0.12	1.63
NGC 1325	SAbc	1593	44	158	3.14	0.15	2.06
03 24 25.6 -21 32 39	71	1594	31.6	158	27.49	0.27	4.01
03 24 25.6 -21 32 35.9	232	1589	38.5	169	91.69	0.069	1.39
NGC 1345	SBc	1530	23.9	116	1.57	0.64	3.51
03 29 31.7 -17 46 43	34	1536	10.1	116	2.766	1.3	19.7
03 29 31.8 -17 46 40.3	88	1529	8.51	112	15.87	0.34	2.37
NGC 1347	SBcd	1758	12.9	96.9	0.438	0.14	3.35
03 29 41.8 -22 16 45	26	1784	7.06	96.9	3.364	0.38	11.2
03 29 41.7 -22 16 44.7	328	1759	8.51	122	7.685	0.078	1.83
NGC 1359	SBcm	1973	–	–	3.44	0.37	–
03 33 47.7 -19 29 31	53	1980	–	–	5.816	1	–
03 33 47.2 -19 29 19.1	325	1966	17.9	108	–	0.35	–
NGC 1371	SABa	1467	61	260	4.2	0.18	1.44
03 35 01.4 -24 55 58	49	1469	37.6	260	61.55	0.24	3.78
03 35 1.89 -24 55 58.6	136	1471	34.5	246	295.1	0.041	1.62
NGC 1385	SBcd	1493	19.8	138	2.67	0.093	8.69
03 37 28.3 -24 30 05	40	1503	22.8	138	33.66	0.18	6.51
03 37 27.8 -24 30 6.68	181	1493	30.5	140	50.77	0.048	0.866
NGC 1390	SB0/a	1207	15.2	118	0.312	0.15	1.72
03 37 52.2 -19 00 30	60	1221	9.41	118	1.845	0.38	4.49
03 37 52.1 -19 0 29.6	24	1207	8.96	97.2	15.27	0.1	1.62
NGC 1414	SBbc	1695	19.9	78.1	0.577	0.19	1.85
03 40 57.0 -21 42 47	80	1660	11.6	78.1	1.4	1.6	5.44
03 40 57.3 -21 42 49.3	357	1681	11.2	95.4	8.226	0.25	1.71
NGC 1415	SAB0/a	1585	–	158	1.11	0.13	–
03 40 56.8 -22 33 52	69	1576	–	158	36.34	0.089	–
03 40 57 -22 33 49.7	332	1585	32.7	167	–	0.018	–

NGC 1422	SBab	1630	15.4	73.8	0.312	0.07	1.68
03 41 31.2 -21 40 53	80	1660	14.8	–	3.722	0.34	1.82
03 41 31.2 -21 40 54.4	65	1637	18.4	54.2	9.34	0.05	1.04
NGC 1481	S0	–	3.4	–	0.079	0.06	8.8
03 54 29.0 -20 25 38	45	–	6.7	–	2.2	–	2.3
	129	1733	–	–	–	0.02	0.51
NGC 1482	S0/a	–	9.0	–	0.428	0.07	5.0
03 54 38.9 -20 30 08	59	–	16.8	–	28.0	–	1.45
	105	1916	–	–	–	0.01	0.54
UGCA 068	SABcdm	1852	16.9	87.6	0.638	0.21	2.84
03 23 47.2 -19 45 15	34	1843	11.4	87.6	0.931	0.97	6.22
03 23 47.1 -19 45 15.2	35	1838	10.3	84.1	10.17	0.41	1.48
UGCA 077	SBdm	1963	22.1	77.9	1.28	0.87	3.34
03 32 19.3 -17 43 07	66	1956	11.4	77.9	–	2.5	12.4
03 32 19.1 -17 43 10.2	149	1961	12.1	74.5	8.042	–	1.93
SGC 0321.2-1929	IBm	1552	13.1	56.4	0.341	–	2.53
03 23 25.1 -19 17 04	24	1556	–	56.4	–	5.3	–
03 23 25.2 -19 17 5.33	175	1545	–	54.7	–	–	–

The results are also presented in the form of an atlas. The layout of the atlas is shown in Fig. 3.12. The channel images are shown separately followed by the atlas. The high resolution images ($20'' - 30''$) are presented in this atlas. The contents of the different panels in the atlas are described below:

Total H I image The contours of the total H I map in column density units are overlaid upon a gray scale image of the galaxy from *Digitized Sky Survey (DSS)*. The contour starts at 10^{20} cm^{-2} with increments of 2×10^{20} cm^{-2}. The first contour is in white, and the rest of them are in black. The contours become progressively thicker (appearing darker) in steps starting from a value 1.2×10^{21} cm^{-2} till 2×10^{21} cm^{-2}, and then beyond the column densities of 2×10^{21} cm^{-2}. The beam is shown at the bottom left hand corner. A bar of length 5 kpc is drawn near the upper left hand corner of the map.

Velocity field The velocity field of a galaxy is shown as iso-velocity contours overlaid upon the DSS image. The white contours are for velocities in the approaching half of the galaxy and dark contours are for velocities in the receding half of the galaxy. The thick dark contour line which is almost a straight line near the centre of a galaxy represents the systemic velocity of the galaxy. The coordinates are in the J 2000 epoch. A similar bar and circle as marked in the total H I image are also marked in this panel.

H I Global profile The H I global profile is shown as a function of the Heliocentric velocity (optical definition). The dark points in the profile are locations at which measurements are carried out. Occasionally, single point with either very high or very low value as compared to the noise are seen in the spectrum. These points are due to bad channels. The systemic velocity of the galaxy estimated from the tilted ring fit is written near the top left hand corner of the panel.

H I mass surface density The face-on H I mass surface density is shown in this panel. The values in the approaching and receding halves are drawn by open and filled circles respectively. The average profile is shown as a thick line. The abscissa is galacto-centric radius in kpc and the ordinate is average surface density in units of $M_\odot$ pc^{-2}. An arrow is marked along the abscissa at a position corresponding to the optical radius estimated at 25 mag arcsec^{-2} B-band isophotal level from the RC3 catalog.

Position-Velocity diagrams The contour images of position-Velocity or PV diagrams are shown along the major and minor axis of the galaxy. The first two contour are at 3 mJy/beam and 5 mJy/beam. The next contours starts from 7 mJy/beam with increments of 4 mJy/beam. The

velocities are Heliocentric and optical. The vertical dotted line marks the dynamical centre of the galaxy determined from the tilted ring fit. Similarly a horizontal dotted line marks the systemic velocity determined from the tilted ring fit. The abscissa is distance in arcsec from the dynamical centre.

Axial parameters and rotation curve The axial parameters (PA, and INCL) determined from the tilted ring fits are plotted in the upper two panels of this figure. The thin lines in these two panels are showing the final adopted trend of the variation of PA and INCL. The values of PA and INCL determined from the optical images are marked in the respective panels by an asterisk sign. The rotation curve (after adjustments using PV diagrams) is shown in the bottom panel. The approaching and receding halves are plotted separately with open and filled symbols respectively. The average rotation curve is drawn by a thin line. The maximum rotation velocity determined from the H I width at 50% level corrected for inclination, instrumental and random motions is shown by an asterisk near the right hand side of the plot. The abscissa is galacto-centric radius in kpc.

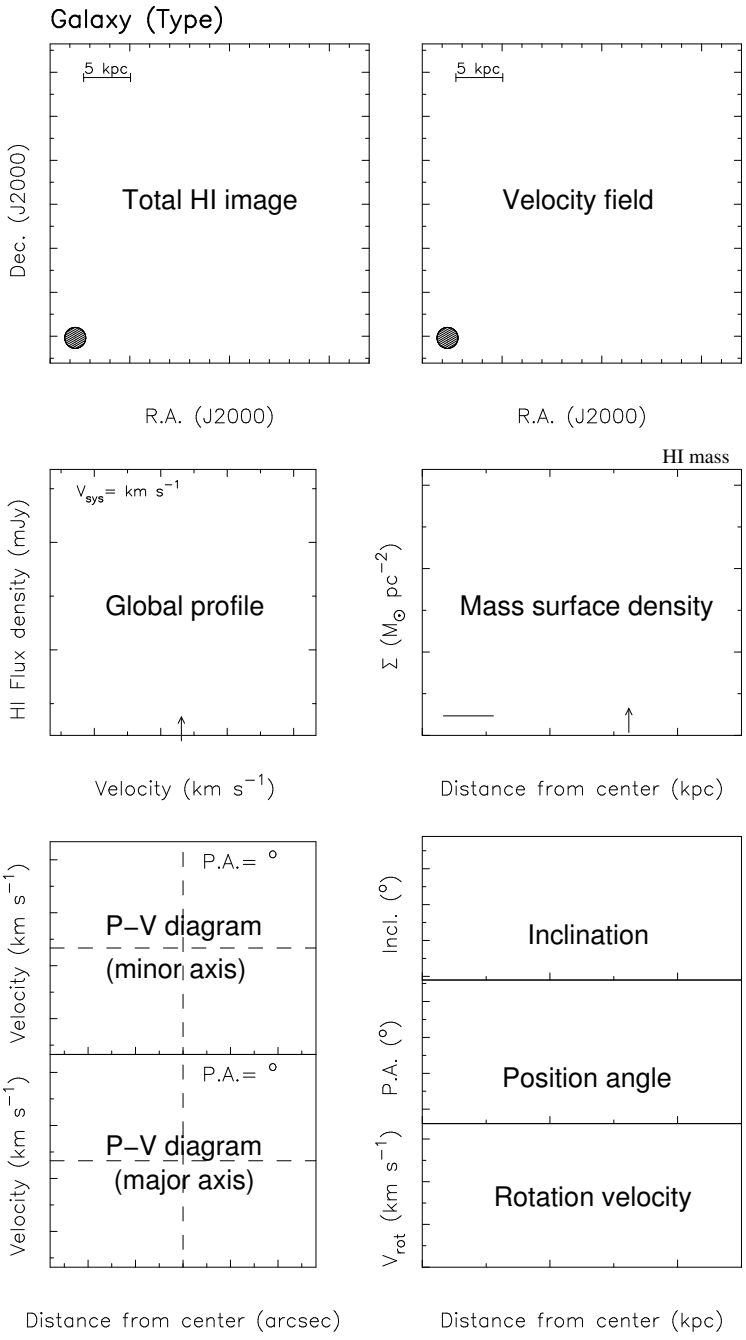

Figure 3.12: The layout of the atlas

Bibliography

[1] Begeman, K. 1989, *A&A*, **223**, 47

[2] Bosma, A., 1978, *PhD Thesis*, (Groningen Univ.)

[3] Bottinelli, L., Gouguenheim, L., Fouque, P., & Paturel, G. 1990, *A&A Supl.*, **82**, 391

[4] Broeils, A. H., & Rhee, M.-H. 1997, *A&A*, **324**, 877

[5] Freeman, K.C 1970, *ApJ*, **160**, 811

[6] Haynes, M. P., & Giovanelli, R. 1984, *AJ*, **89**, 758

[7] Rubin, V.C., Kenny, J.D., Boss, A.P., & Ford, W.K. 1989, *AJ*, **98**, 1246

[8] Rupen, M. P. 1999, *In Synthesis imaging in radio astronomy, ASP conf. Ser.*, **180**, 229

[9] Ryle, M., & Hewish, A. 1960, *MNRAS*, **120**, 220

[10] Sancisi, R., & Allen, R. J. 1979, *A&A*, **74**, 73

[11] Spitzer, L. Jr. 1978, *In Physical processes in the Interstellar medium*, (Wiley-interscience publication)

[12] Swarup, G., Ananthakrishnan, S., Kapahi, V.K. et al. 1991, *Curr. Sci.*, **60**, 95

[13] Verheijen, M.A.W, $ Sancisi R. 2001, **A&A**, 370, 765

[14] Verheijen, M.A.W. 1997, *PhD Thesis, Groningen Univ.*

[15] Swater, R. 1999, *PhD Thesis*, (Groningen Univ.)

[16] Tully, R. B., & Fouque, P. 1985, *ApJ Supl.*, **58**, 67

H I Channel Images

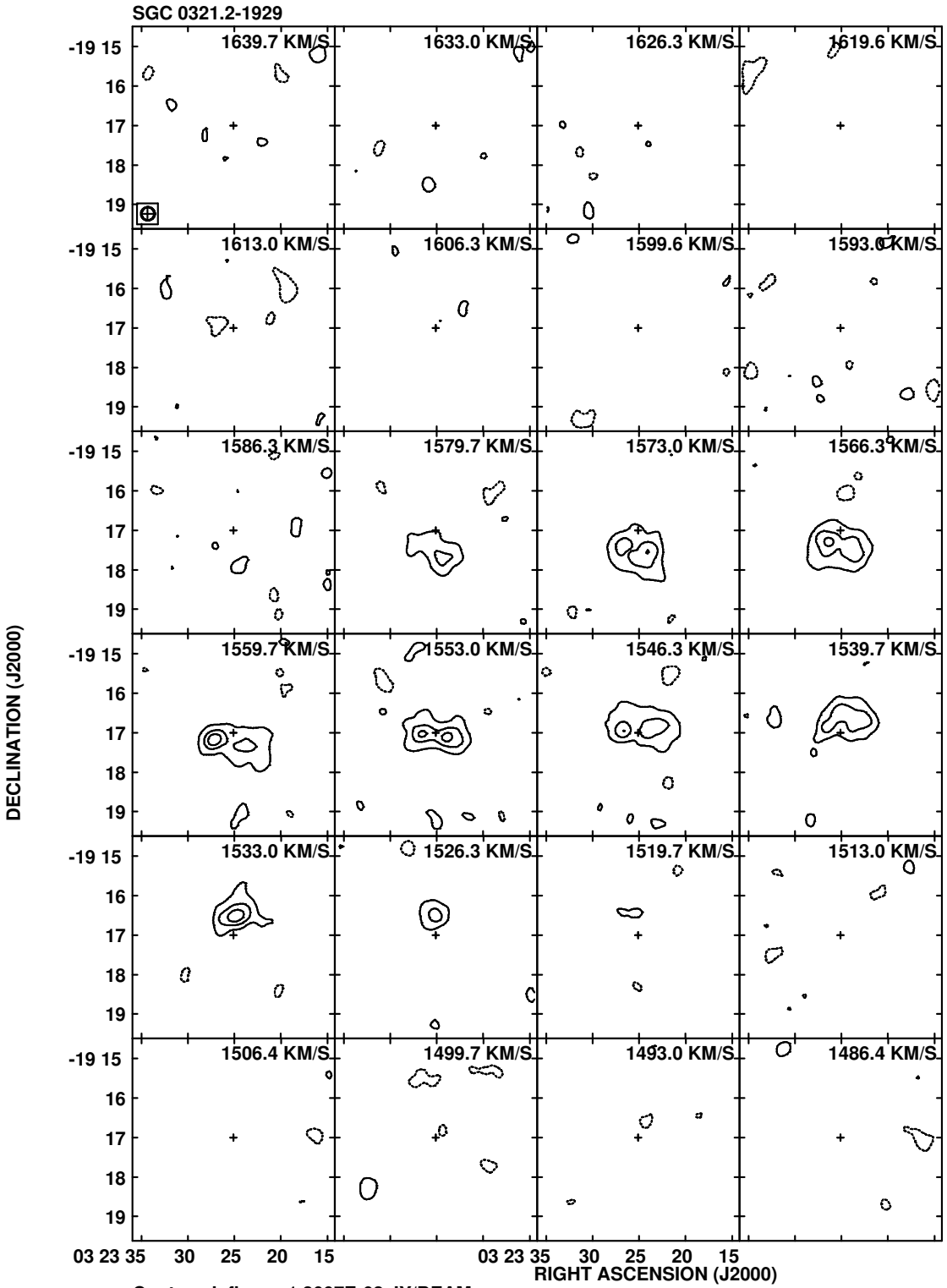

Cont peak flux = 1.3097E-02 JY/BEAM
Levs = 3.350E-03 * (-5, -4, -3, -2, -1, 1, 2, 3, 4, 5, 6, 7, 8, 9, 10, 11, 12, 13, 14, 15)

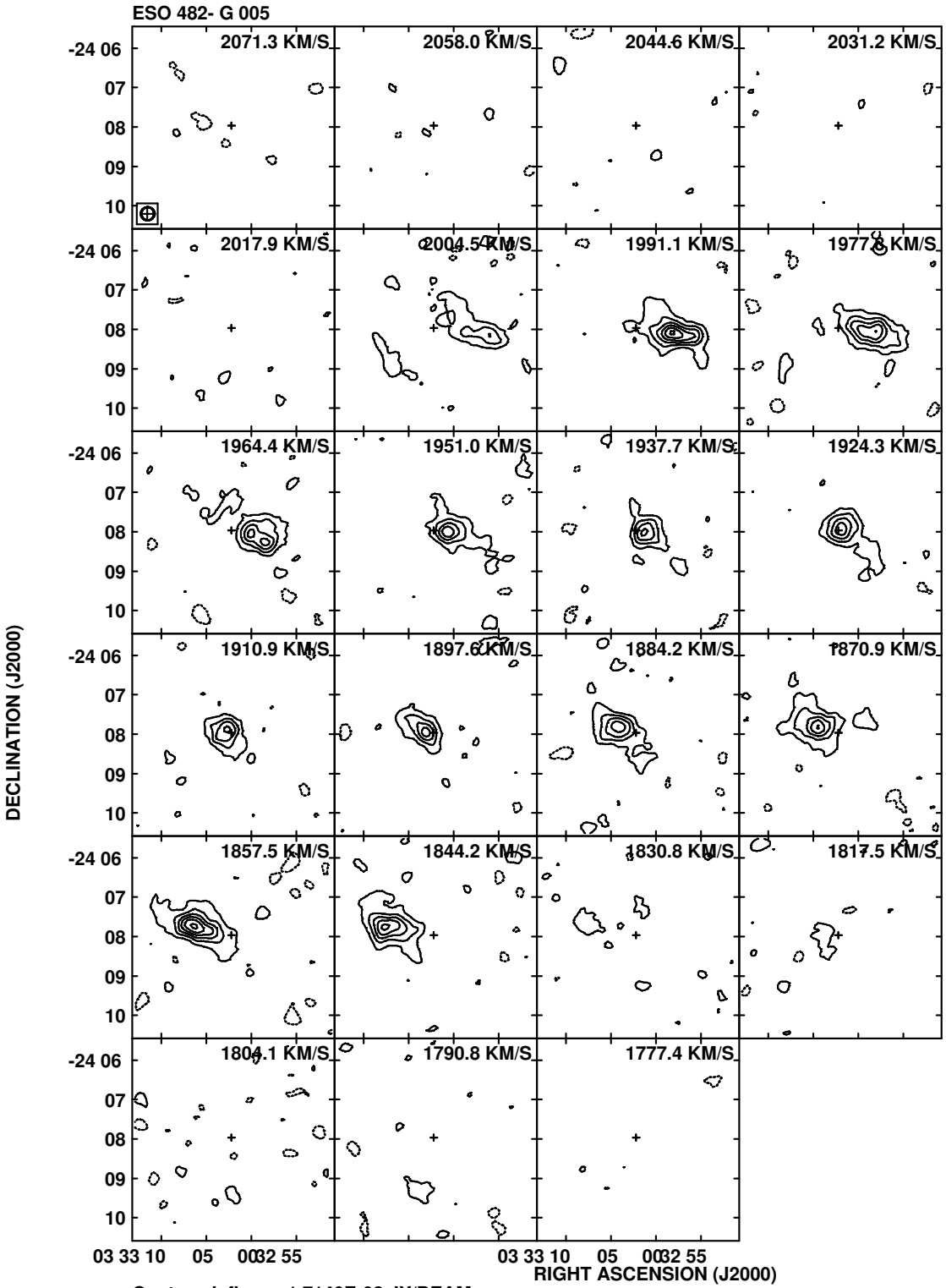

Cont peak flux = 1.7140E-02 JY/BEAM
Levs = 2.770E-03 * (-5, -4, -3, -2, -1, 1, 2, 3, 4, 5, 6, 7, 8, 9, 10, 11, 12, 13, 14, 15)

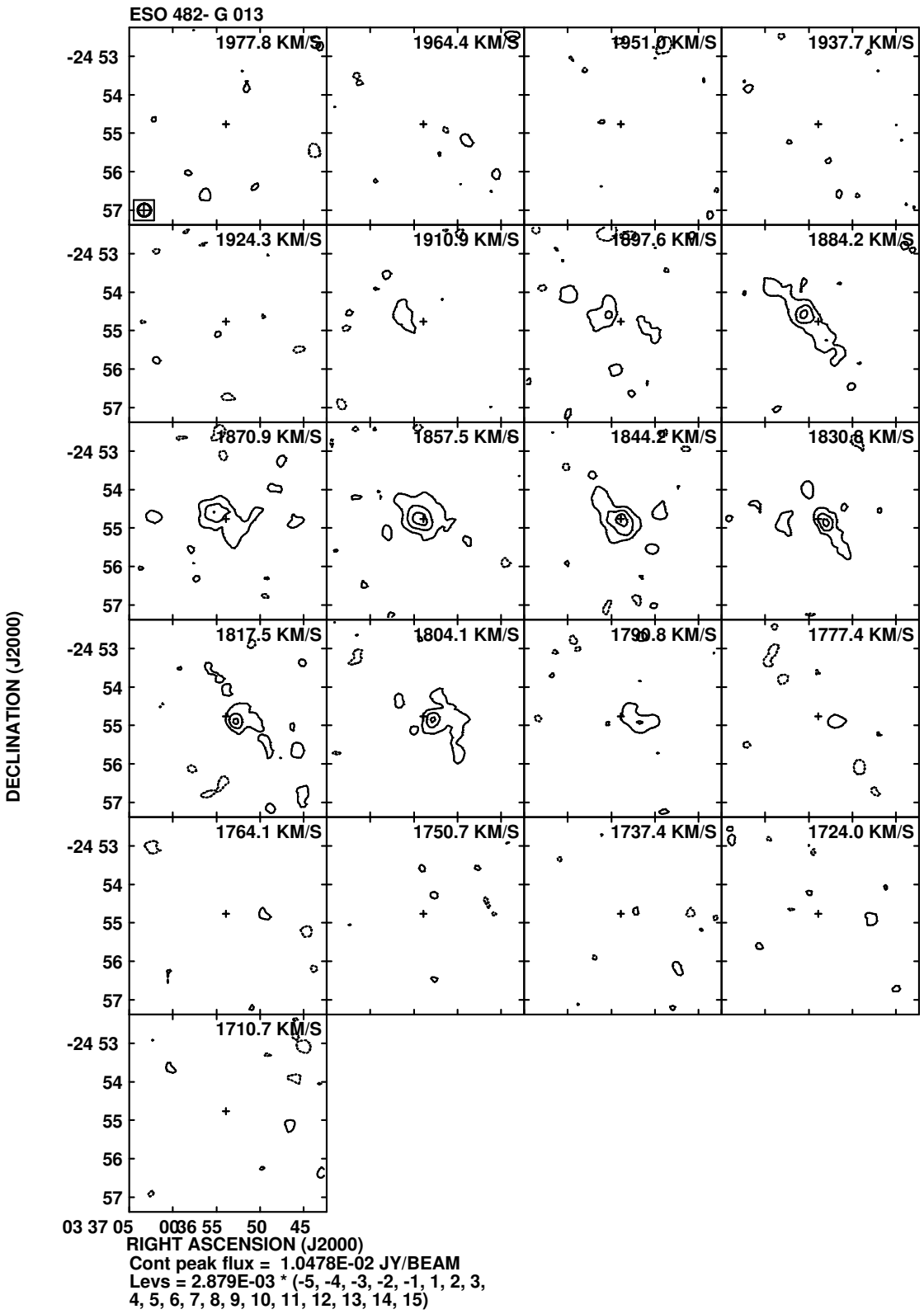
ESO 482- G 013
1977.8 KM/S
1964.4 KM/S
1951.0 KM/S
1937.7 KM/S
1924.3 KM/S
1910.9 KM/S
1897.6 KM/S
1884.2 KM/S
1870.9 KM/S
1857.5 KM/S
1844.2 KM/S
1830.8 KM/S
1817.5 KM/S
1804.1 KM/S
1790.8 KM/S
1777.4 KM/S
1764.1 KM/S
1750.7 KM/S
1737.4 KM/S
1724.0 KM/S
1710.7 KM/S
-24 53
54
55
56
57
03 37 05
00
36 55
50
45
DECLINATION (J2000)
RIGHT ASCENSION (J2000)
Cont peak flux = 1.0478E-02 JY/BEAM
Levs = 2.879E-03 * (-5, -4, -3, -2, -1, 1, 2, 3, 4, 5, 6, 7, 8, 9, 10, 11, 12, 13, 14, 15)

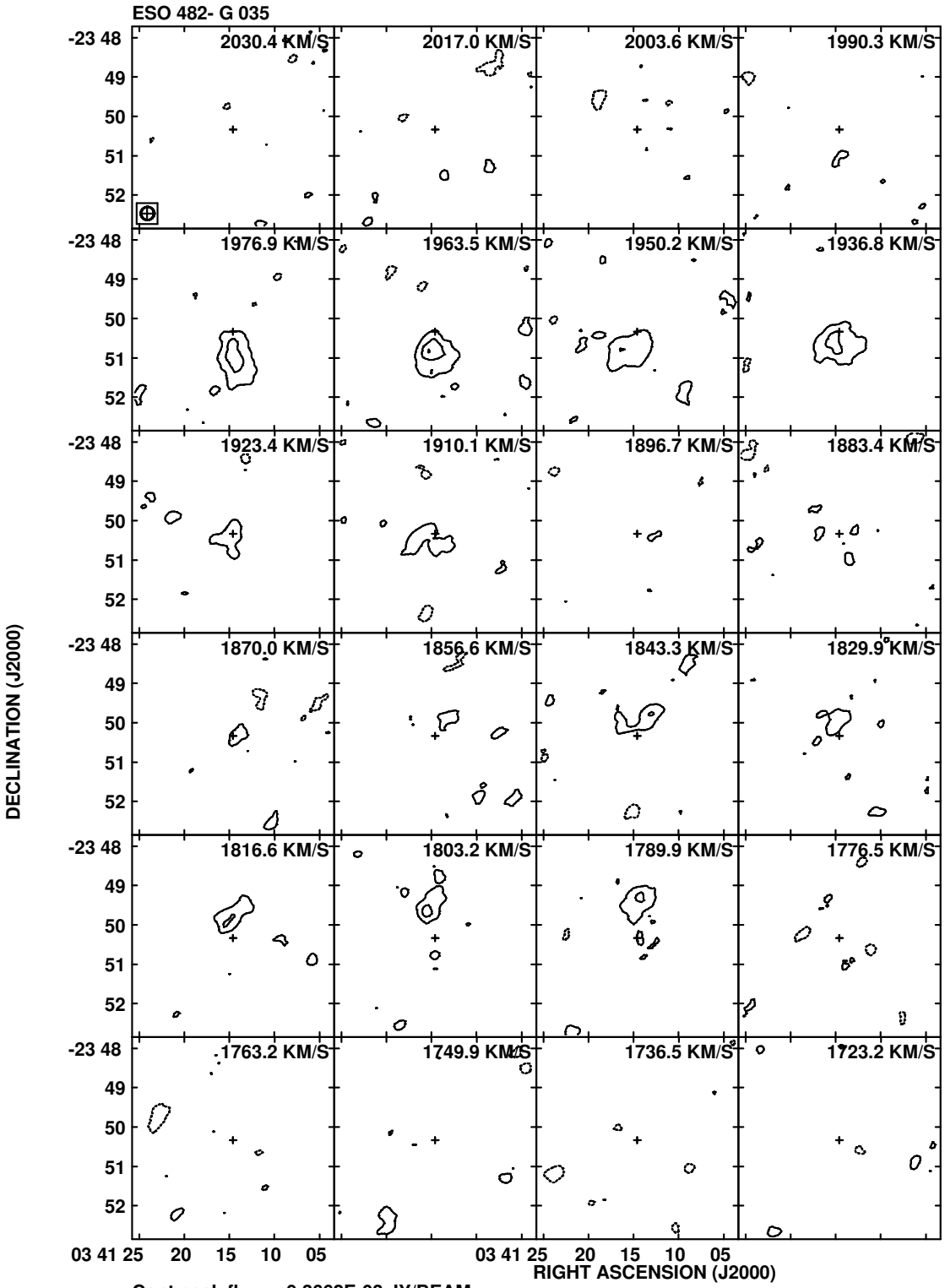

Cont peak flux = 9.3662E-03 JY/BEAM
Levs = 3.078E-03 * (-5, -4, -3, -2, -1, 1, 2, 3, 4, 5, 6, 7, 8, 9, 10, 11, 12, 13, 14, 15)

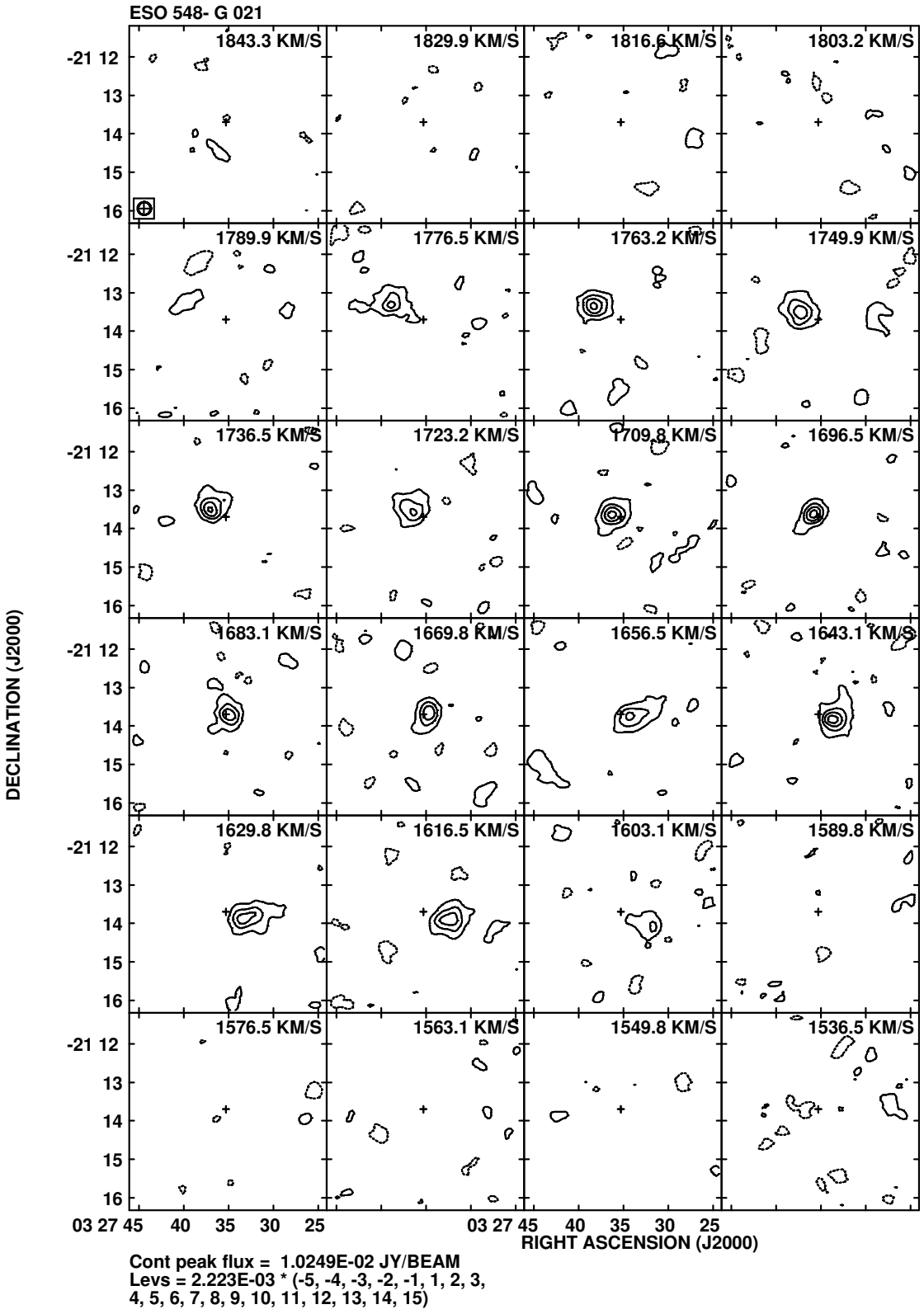

Cont peak flux = 1.0249E-02 JY/BEAM
Levs = 2.223E-03 * (-5, -4, -3, -2, -1, 1, 2, 3, 4, 5, 6, 7, 8, 9, 10, 11, 12, 13, 14, 15)

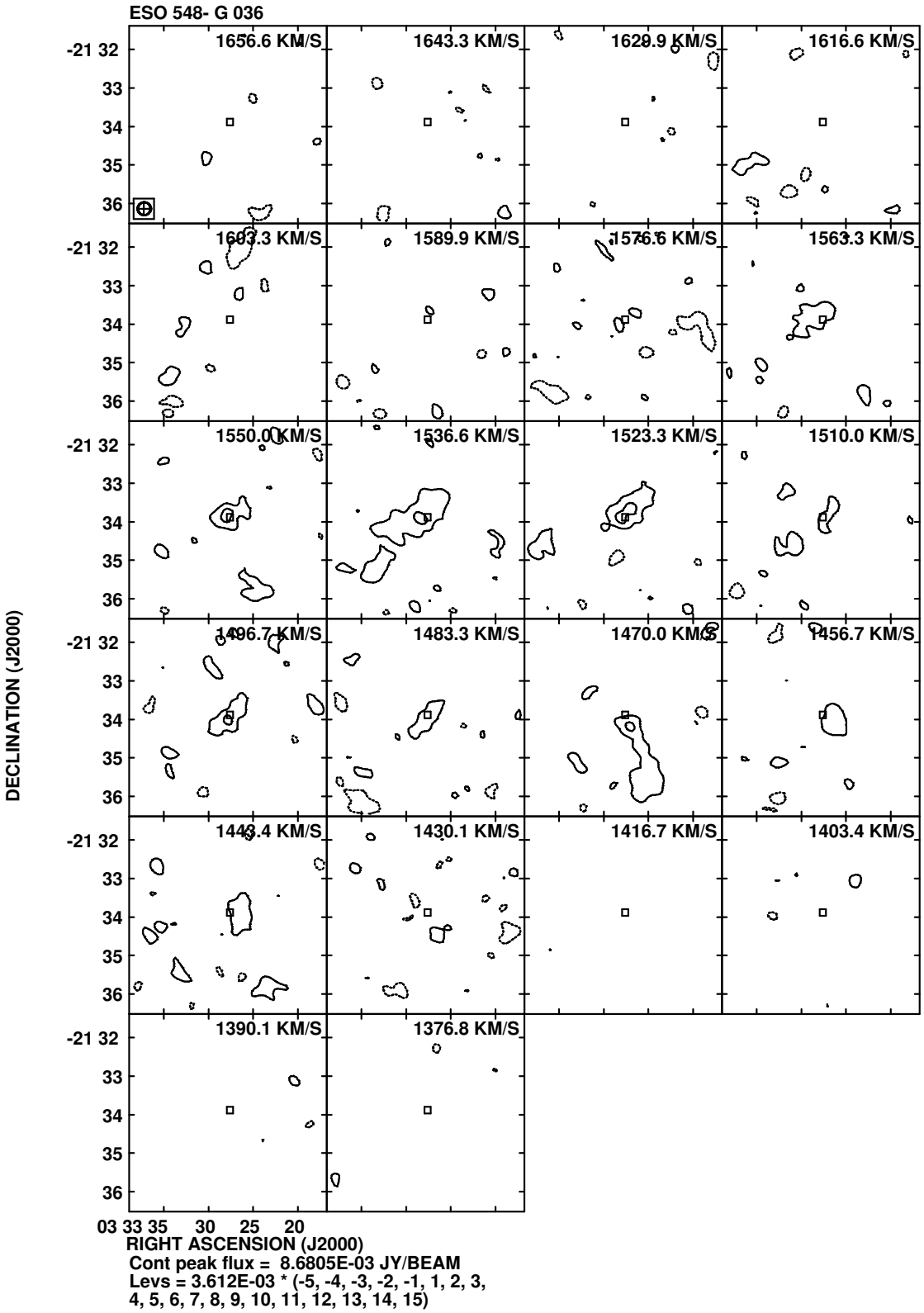
ESO 548- G 036
1656.6 KM/S
1643.3 KM/S
1629.9 KM/S
1616.6 KM/S
1603.3 KM/S
1589.9 KM/S
1576.6 KM/S
1563.3 KM/S
1550.0 KM/S
1536.6 KM/S
1523.3 KM/S
1510.0 KM/S
1496.7 KM/S
1483.3 KM/S
1470.0 KM/S
1456.7 KM/S
1443.4 KM/S
1430.1 KM/S
1416.7 KM/S
1403.4 KM/S
1390.1 KM/S
1376.8 KM/S
-21 32
33
34
35
36
03 33 35 30 25 20
DECLINATION (J2000)
RIGHT ASCENSION (J2000)
Cont peak flux = 8.6805E-03 JY/BEAM
Levs = 3.612E-03 * (-5, -4, -3, -2, -1, 1, 2, 3, 4, 5, 6, 7, 8, 9, 10, 11, 12, 13, 14, 15)

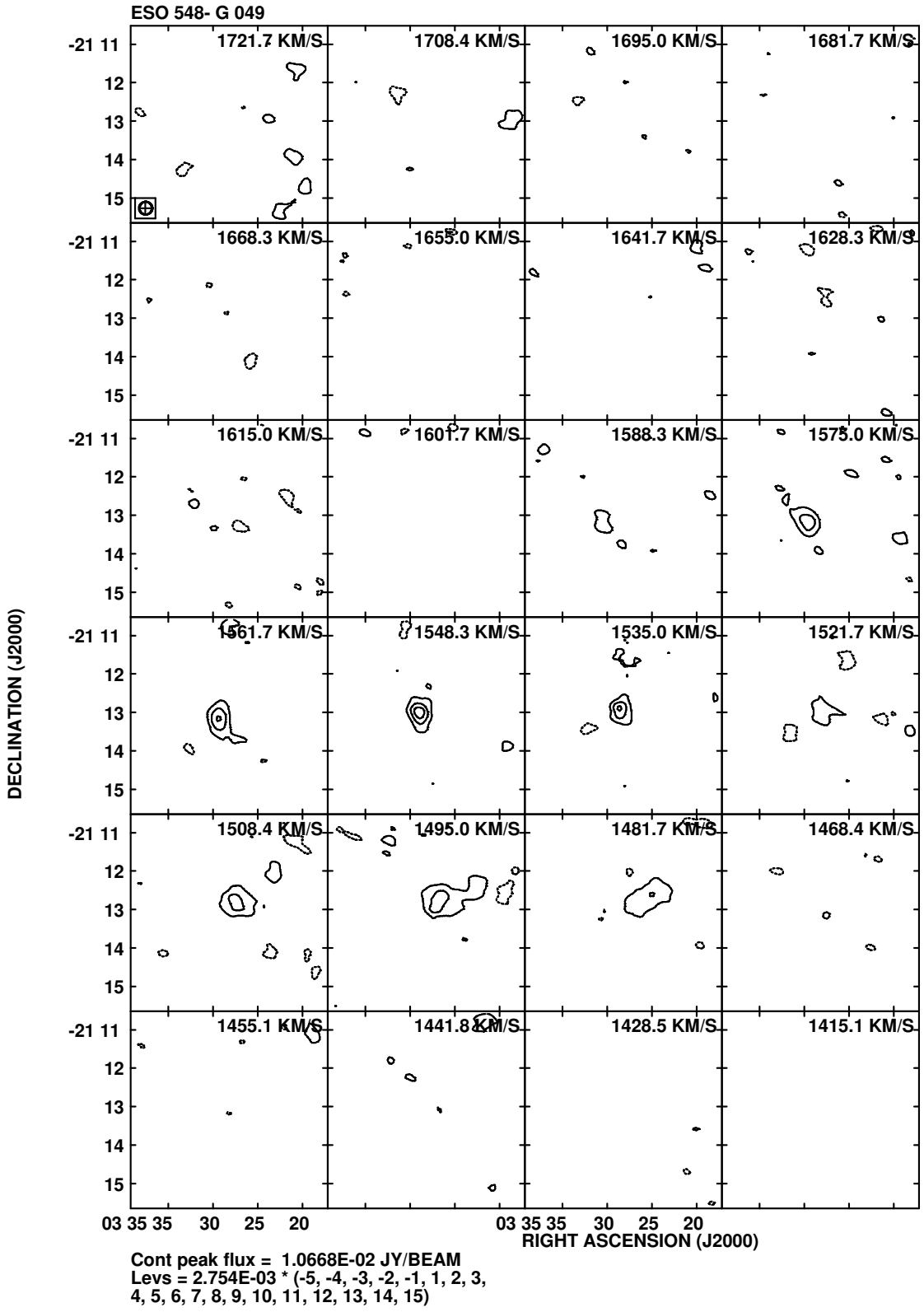

Cont peak flux = 1.0668E-02 JY/BEAM
Levs = 2.754E-03 * (-5, -4, -3, -2, -1, 1, 2, 3, 4, 5, 6, 7, 8, 9, 10, 11, 12, 13, 14, 15)

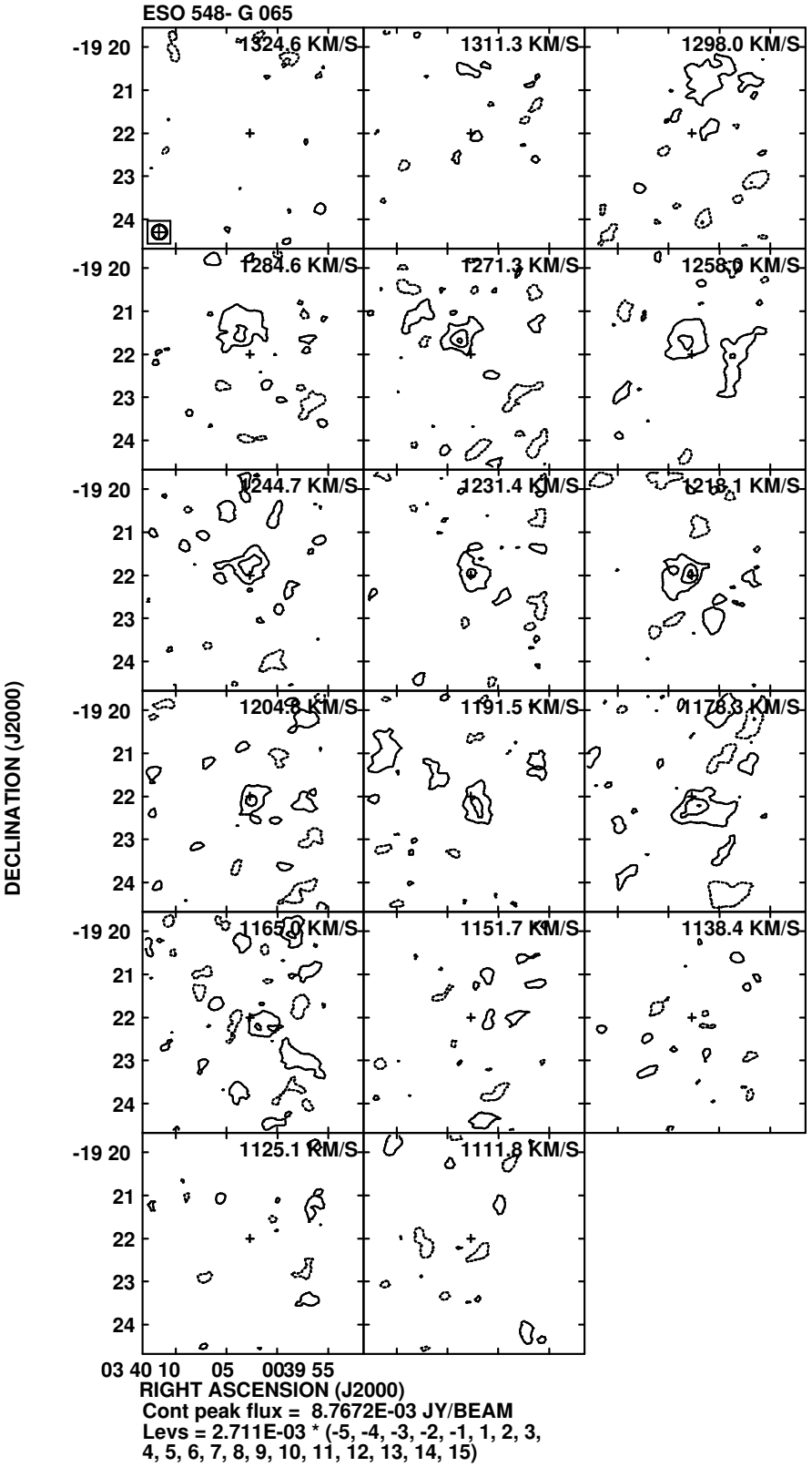
ESO 548- G 065
1324.6 KM/S
1311.3 KM/S
1298.0 KM/S
1284.6 KM/S
1271.3 KM/S
1258.0 KM/S
1244.7 KM/S
1231.4 KM/S
1218.1 KM/S
1204.8 KM/S
1191.5 KM/S
1178.3 KM/S
1165.0 KM/S
1151.7 KM/S
1138.4 KM/S
1125.1 KM/S
1111.8 KM/S
-19 20
21
22
23
24
DECLINATION (J2000)
03 40 10 05 0039 55
RIGHT ASCENSION (J2000)
Cont peak flux = 8.7672E-03 JY/BEAM
Levs = 2.711E-03 * (-5, -4, -3, -2, -1, 1, 2, 3, 4, 5, 6, 7, 8, 9, 10, 11, 12, 13, 14, 15)

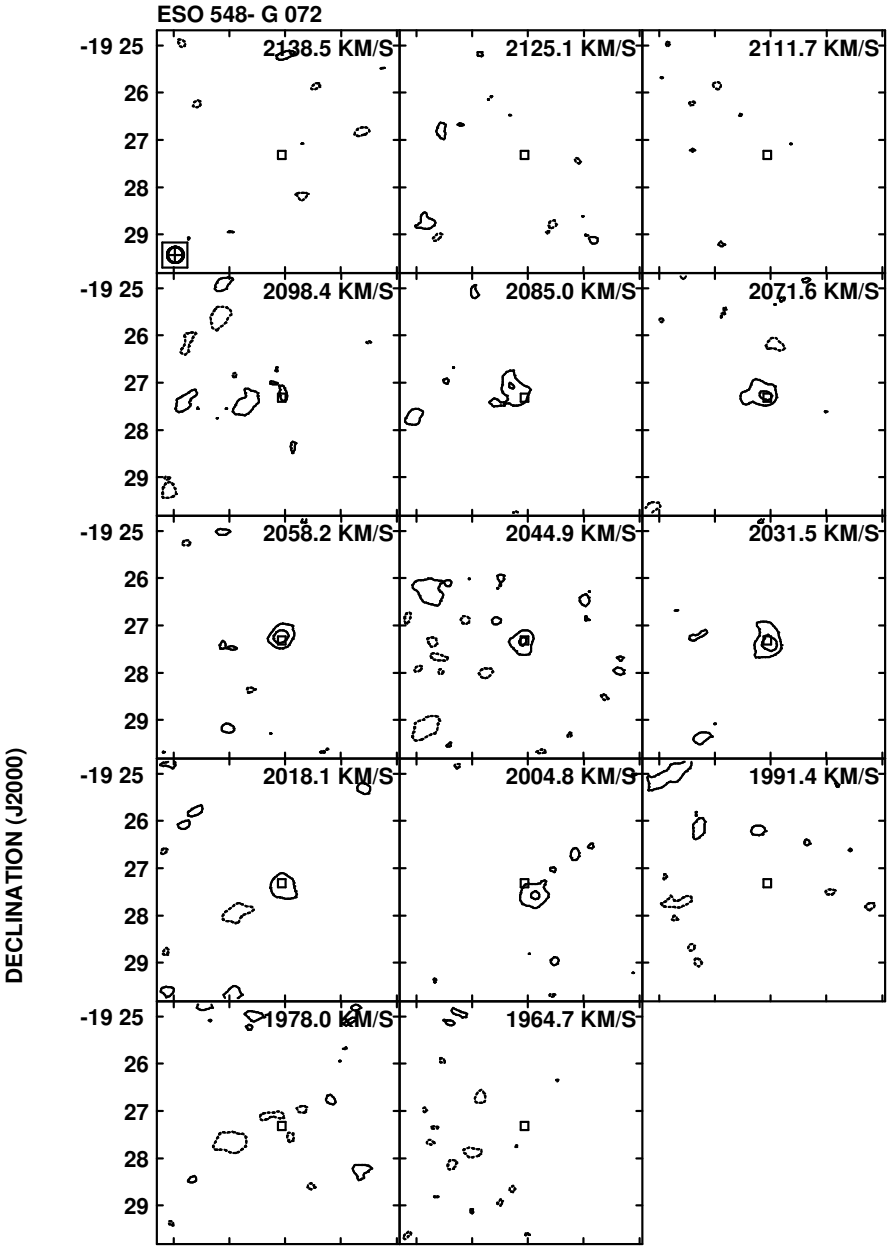

Cont peak flux = 9.4210E-03 JY/BEAM
Levs = 3.245E-03 * (-5, -4, -3, -2, -1, 1, 2, 3, 4, 5, 6, 7, 8, 9, 10, 11, 12, 13, 14, 15)

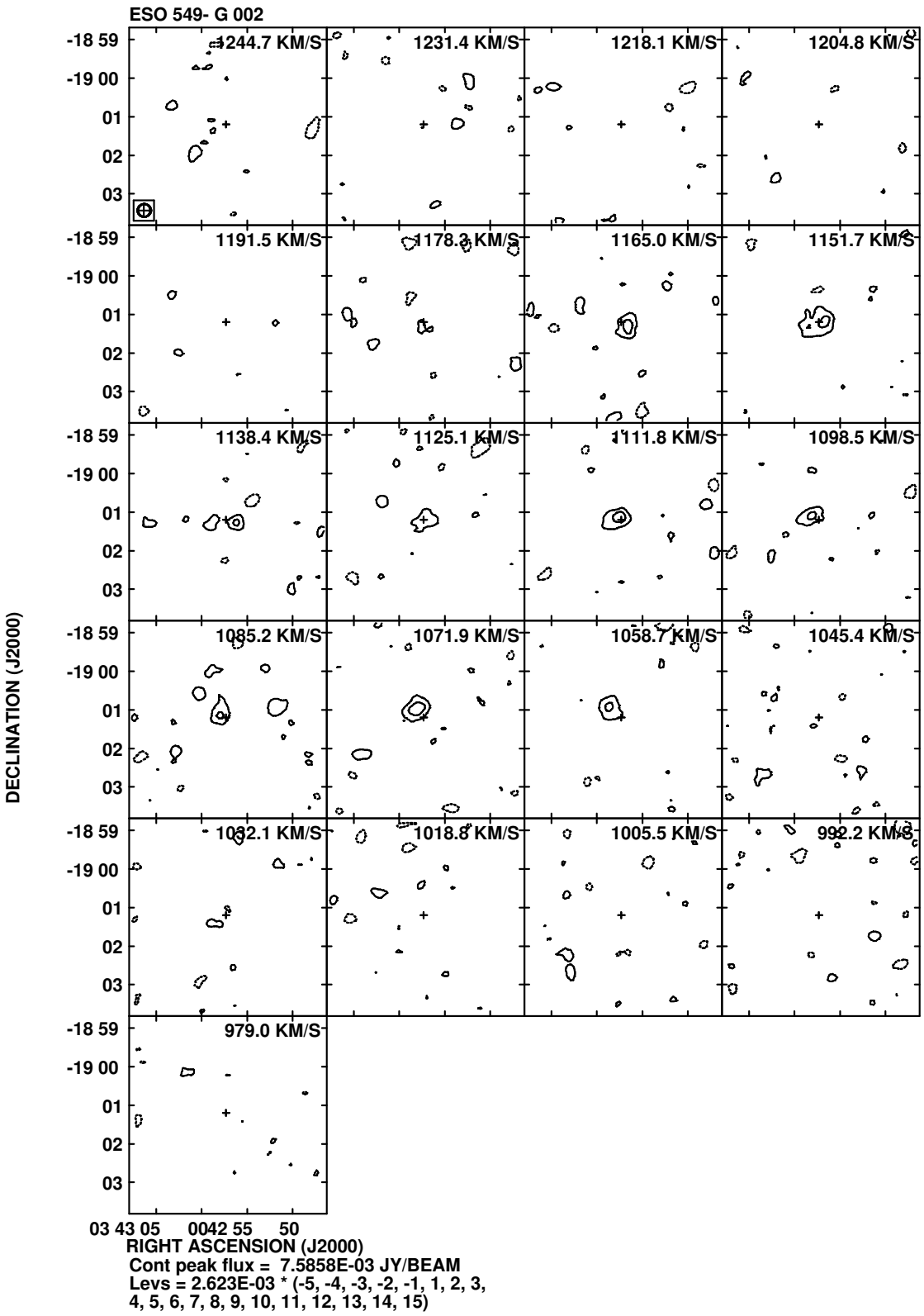
ESO 549- G 002
1244.7 KM/S
1231.4 KM/S
1218.1 KM/S
1204.8 KM/S
1191.5 KM/S
1178.3 KM/S
1165.0 KM/S
1151.7 KM/S
1138.4 KM/S
1125.1 KM/S
1111.8 KM/S
1098.5 KM/S
1085.2 KM/S
1071.9 KM/S
1058.7 KM/S
1045.4 KM/S
1032.1 KM/S
1018.8 KM/S
1005.5 KM/S
992.2 KM/S
979.0 KM/S
-18 59
-19 00
01
02
03
DECLINATION (J2000)
03 43 05
0042 55
50
RIGHT ASCENSION (J2000)
Cont peak flux = 7.5858E-03 JY/BEAM
Levs = 2.623E-03 * (-5, -4, -3, -2, -1, 1, 2, 3, 4, 5, 6, 7, 8, 9, 10, 11, 12, 13, 14, 15)

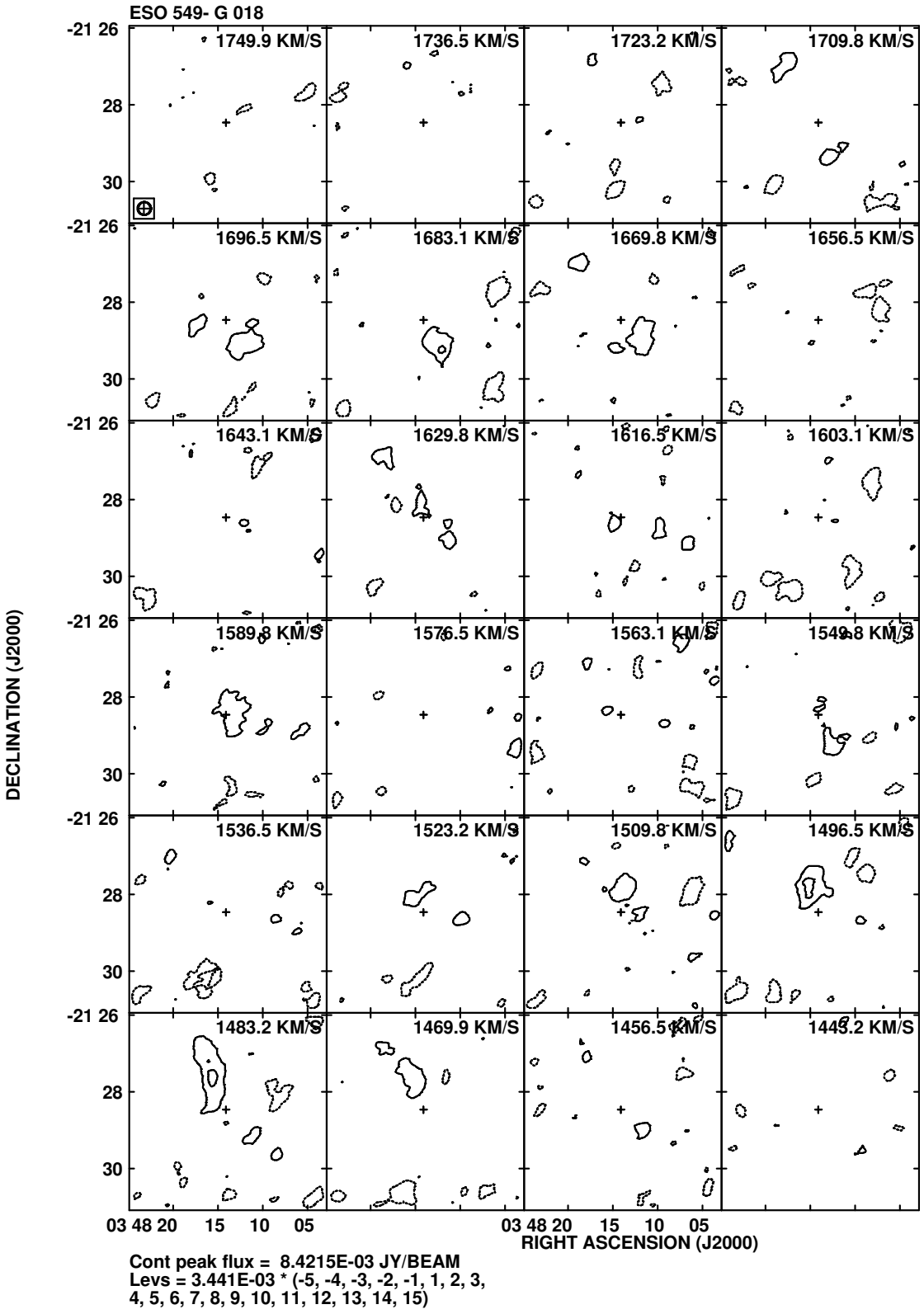

Cont peak flux = 8.4215E-03 JY/BEAM
Levs = 3.441E-03 * (-5, -4, -3, -2, -1, 1, 2, 3, 4, 5, 6, 7, 8, 9, 10, 11, 12, 13, 14, 15)

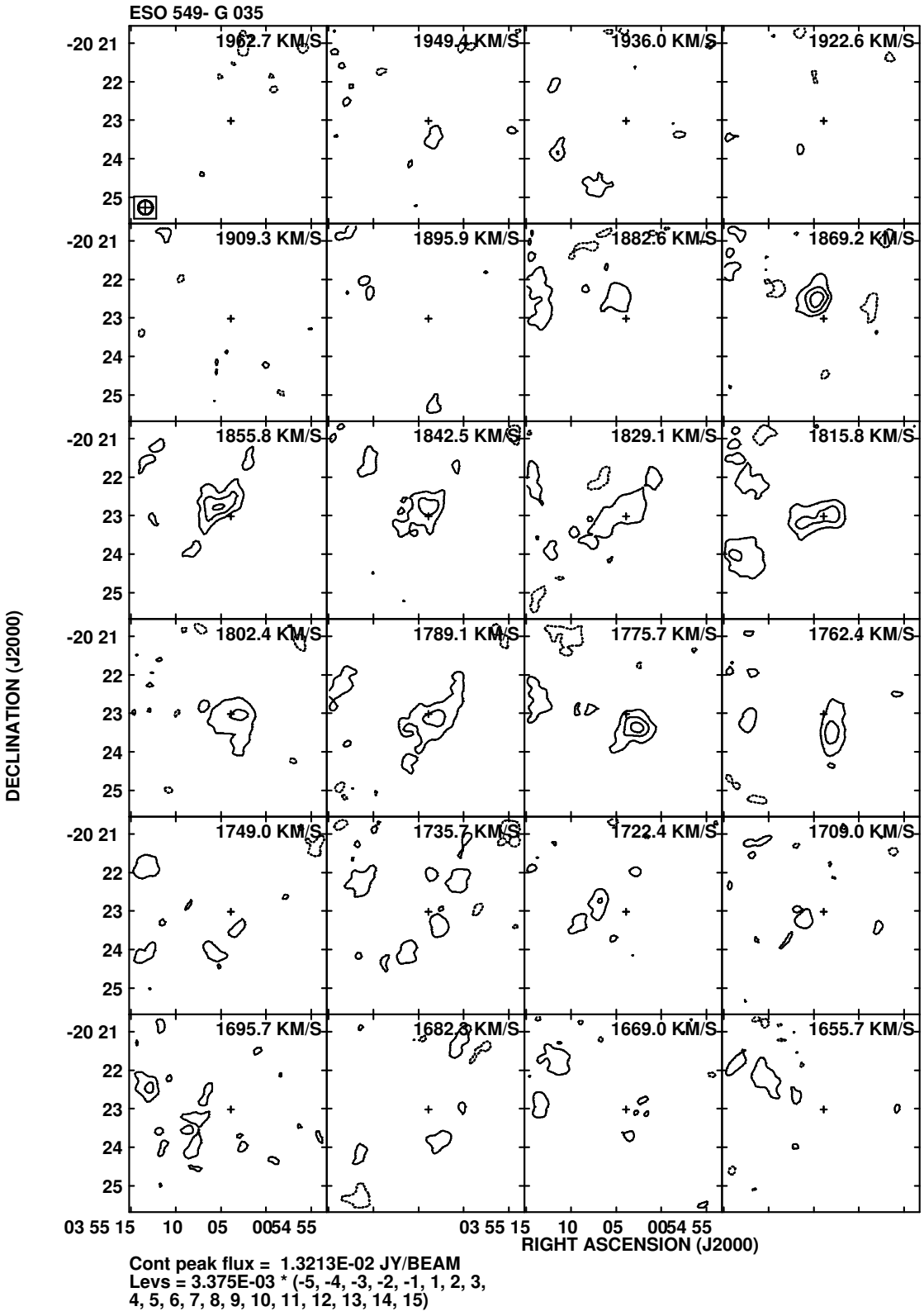

Cont peak flux = 1.3213E-02 JY/BEAM
Levs = 3.375E-03 * (-5, -4, -3, -2, -1, 1, 2, 3, 4, 5, 6, 7, 8, 9, 10, 11, 12, 13, 14, 15)

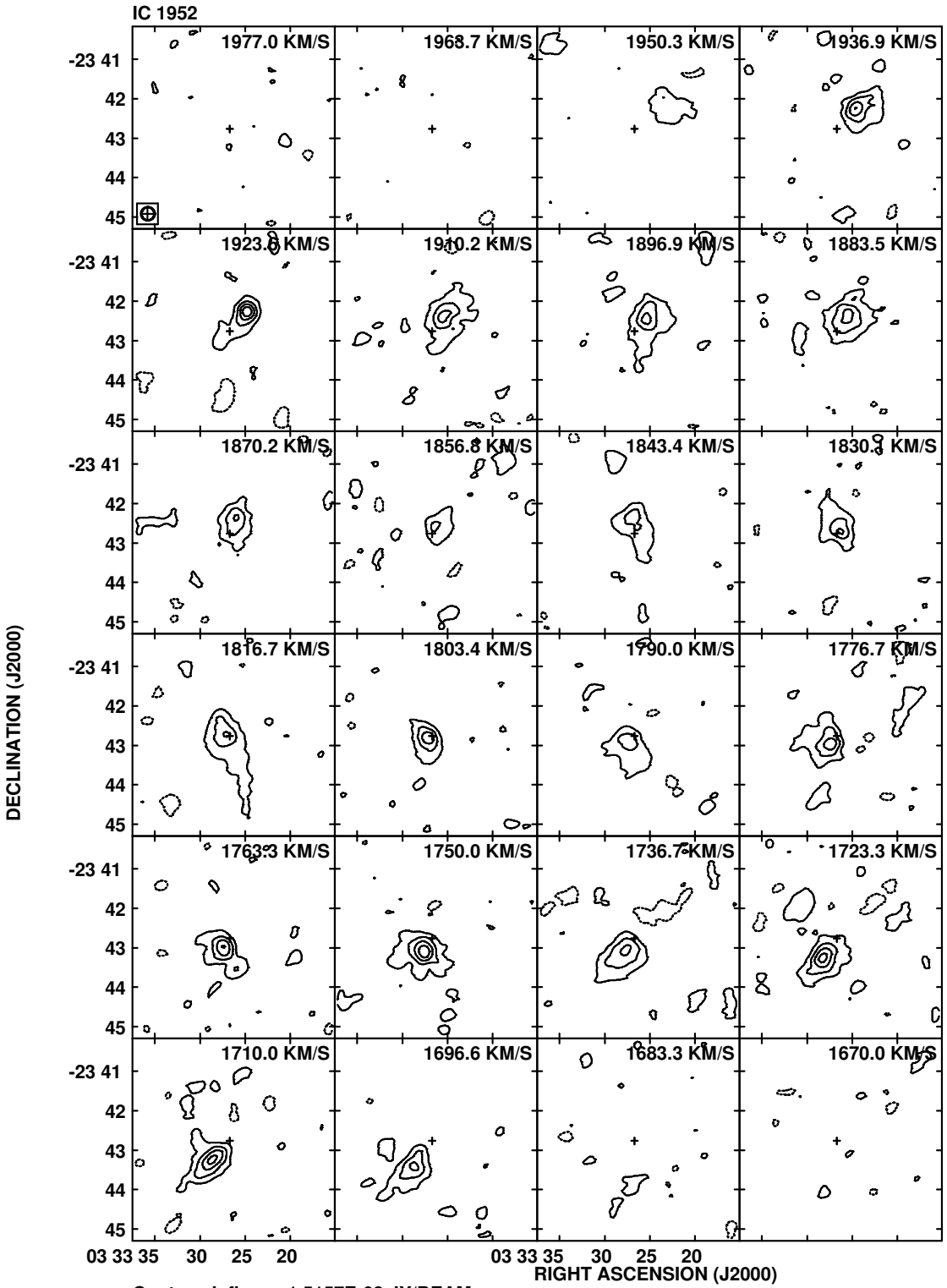
IC 1952
1977.0 KM/S
1963.7 KM/S
1950.3 KM/S
1936.9 KM/S
1923.6 KM/S
1910.2 KM/S
1896.9 KM/S
1883.5 KM/S
1870.2 KM/S
1856.8 KM/S
1843.4 KM/S
1830.1 KM/S
1816.7 KM/S
1803.4 KM/S
1790.0 KM/S
1776.7 KM/S
1763.3 KM/S
1750.0 KM/S
1736.7 KM/S
1723.3 KM/S
1710.0 KM/S
1696.6 KM/S
1683.3 KM/S
1670.0 KM/S
-23 41
42
43
44
45
03 33 35 30 25 20
DECLINATION (J2000)
RIGHT ASCENSION (J2000)
Cont peak flux = 1.5157E-02 JY/BEAM
Levs = 3.104E-03 * (-5, -4, -3, -2, -1, 1, 2, 3, 4, 5, 6, 7, 8, 9, 10, 11, 12, 13, 14, 15)

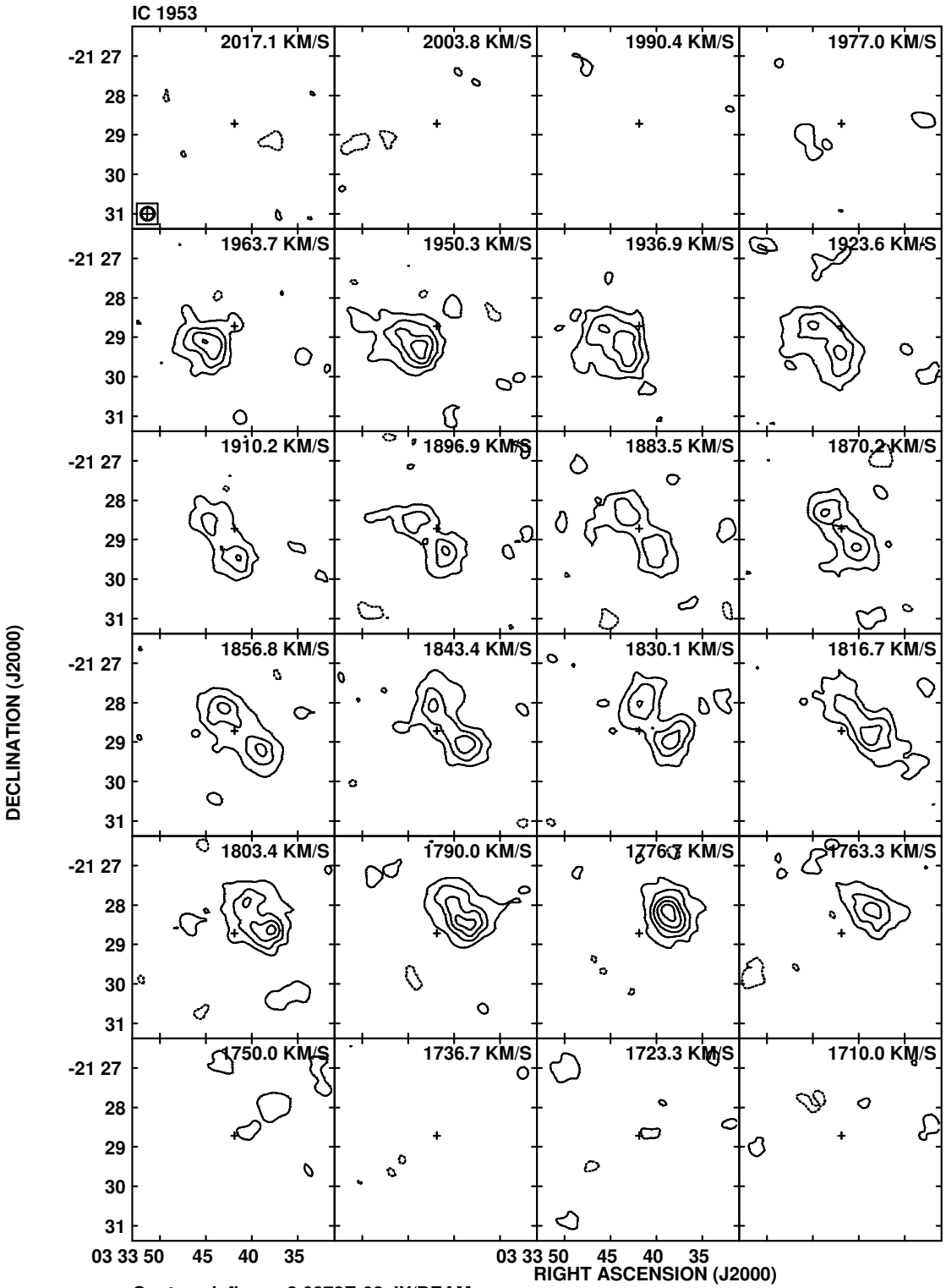

Cont peak flux = 2.0873E-02 JY/BEAM
Levs = 3.674E-03 * (-5, -4, -3, -2, -1, 1, 2, 3, 4, 5, 6, 7, 8, 9, 10, 11, 12, 13, 14, 15)

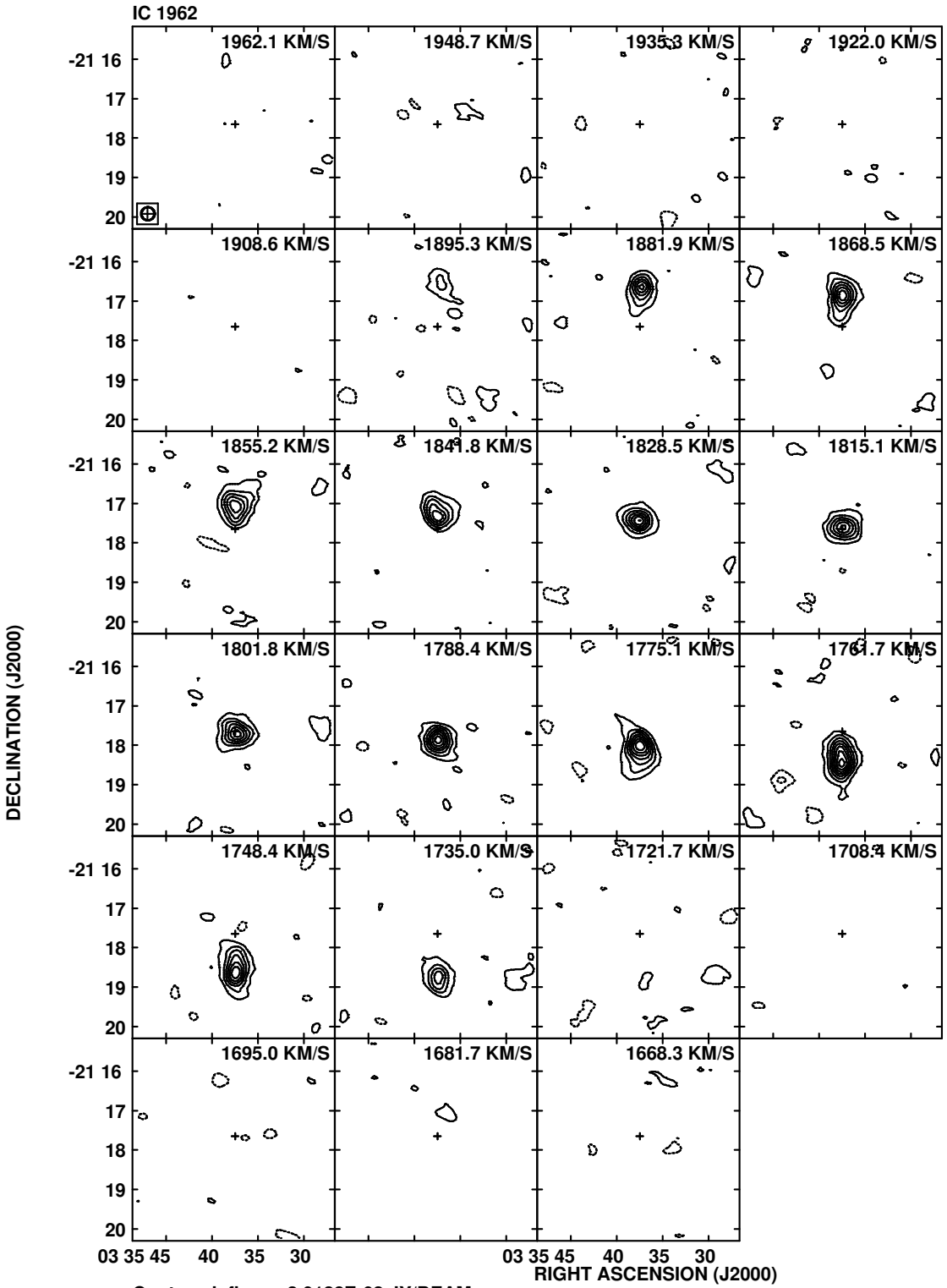

Cont peak flux = 2.0128E-02 JY/BEAM
Levs = 2.369E-03 * (-5, -4, -3, -2, -1, 1, 2, 3, 4, 5, 6, 7, 8, 9, 10, 11, 12, 13, 14, 15)

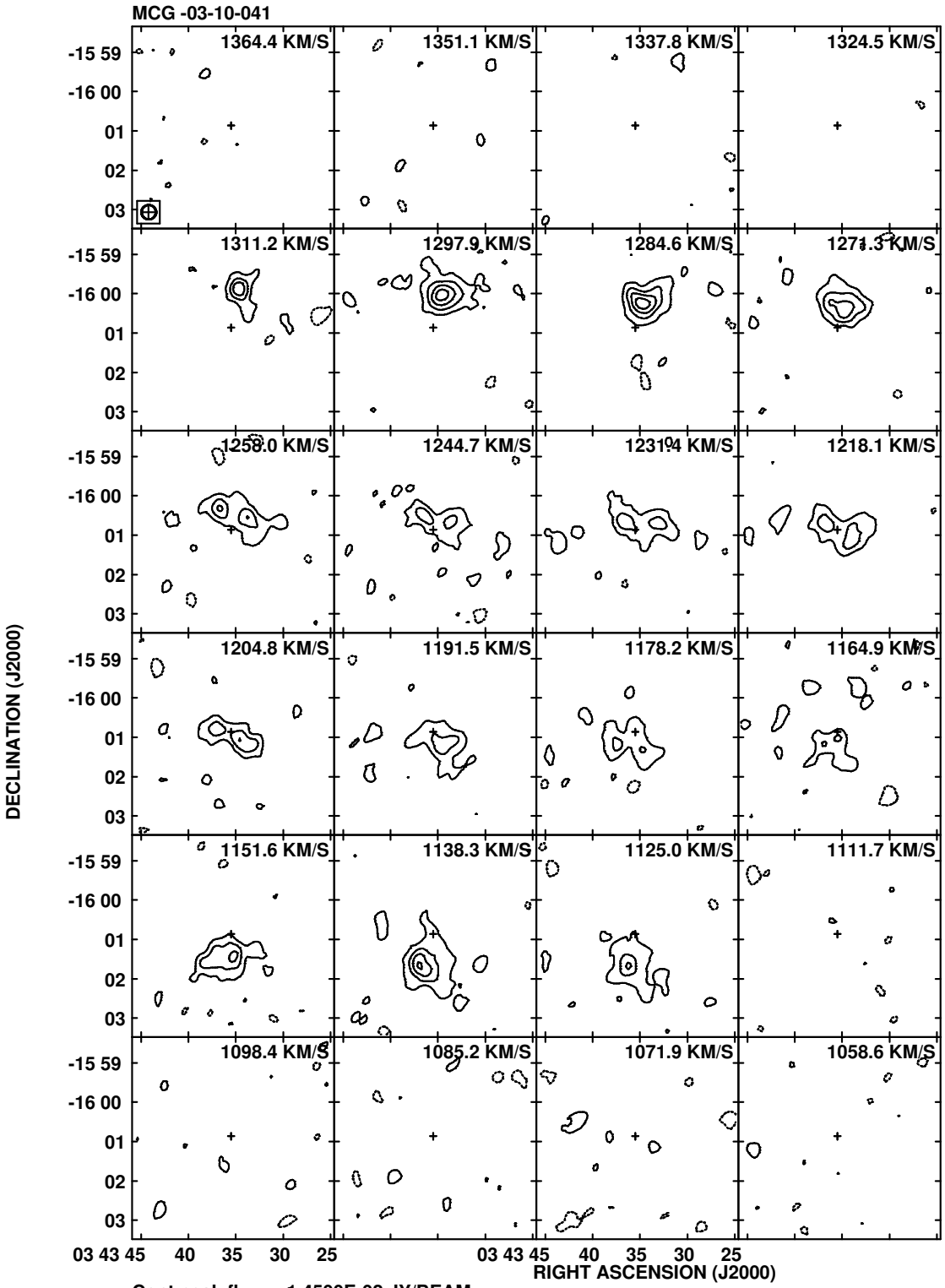

Cont peak flux = 1.4500E-02 JY/BEAM
Levs = 3.113E-03 * (-5, -4, -3, -2, -1, 1, 2, 3, 4, 5, 6, 7, 8, 9, 10, 11, 12, 13, 14, 15)

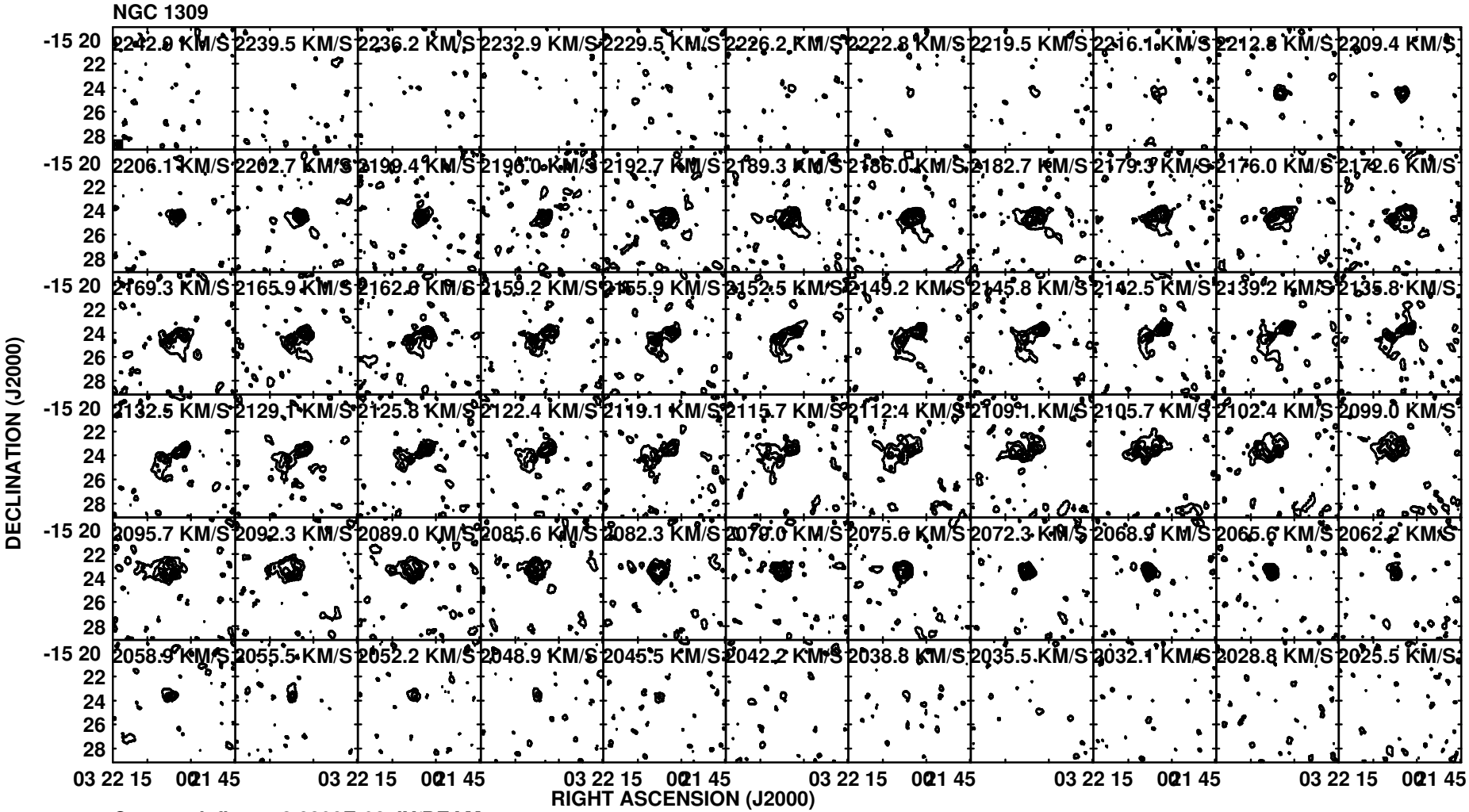

Cont peak flux = 2.8398E-02 JY/BEAM
Levs = 4.164E-03 * (-5, -4, -3, -2, -1, 1, 2, 3, 4, 5, 6, 7, 8, 9, 10, 11, 12, 13, 14, 15)

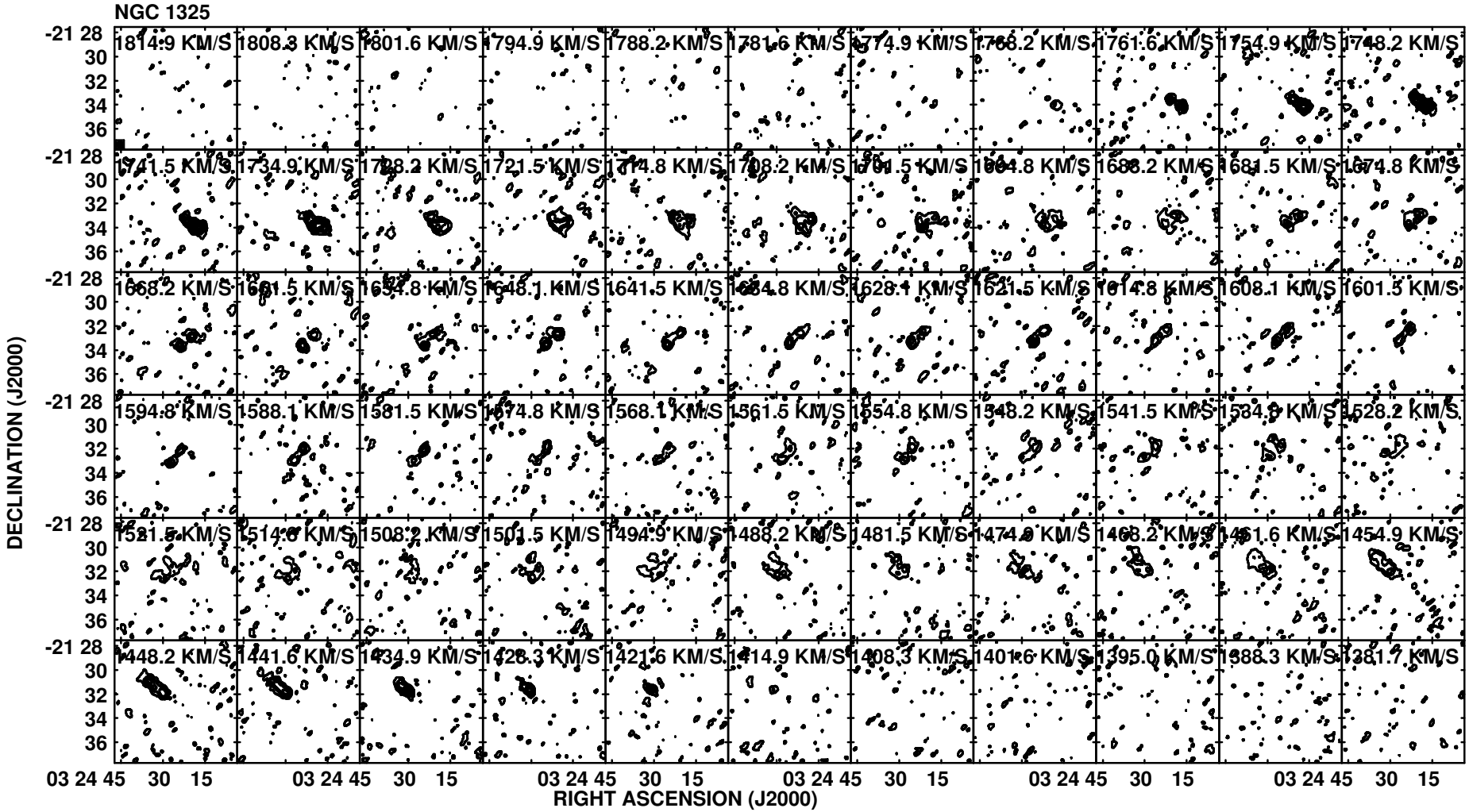

Cont peak flux = 4.0091E-02 JY/BEAM
Levs = 4.656E-03 * (-5, -4, -3, -2, -1, 1, 2, 3, 4, 5, 6, 7, 8, 9, 10, 11, 12, 13, 14, 15)

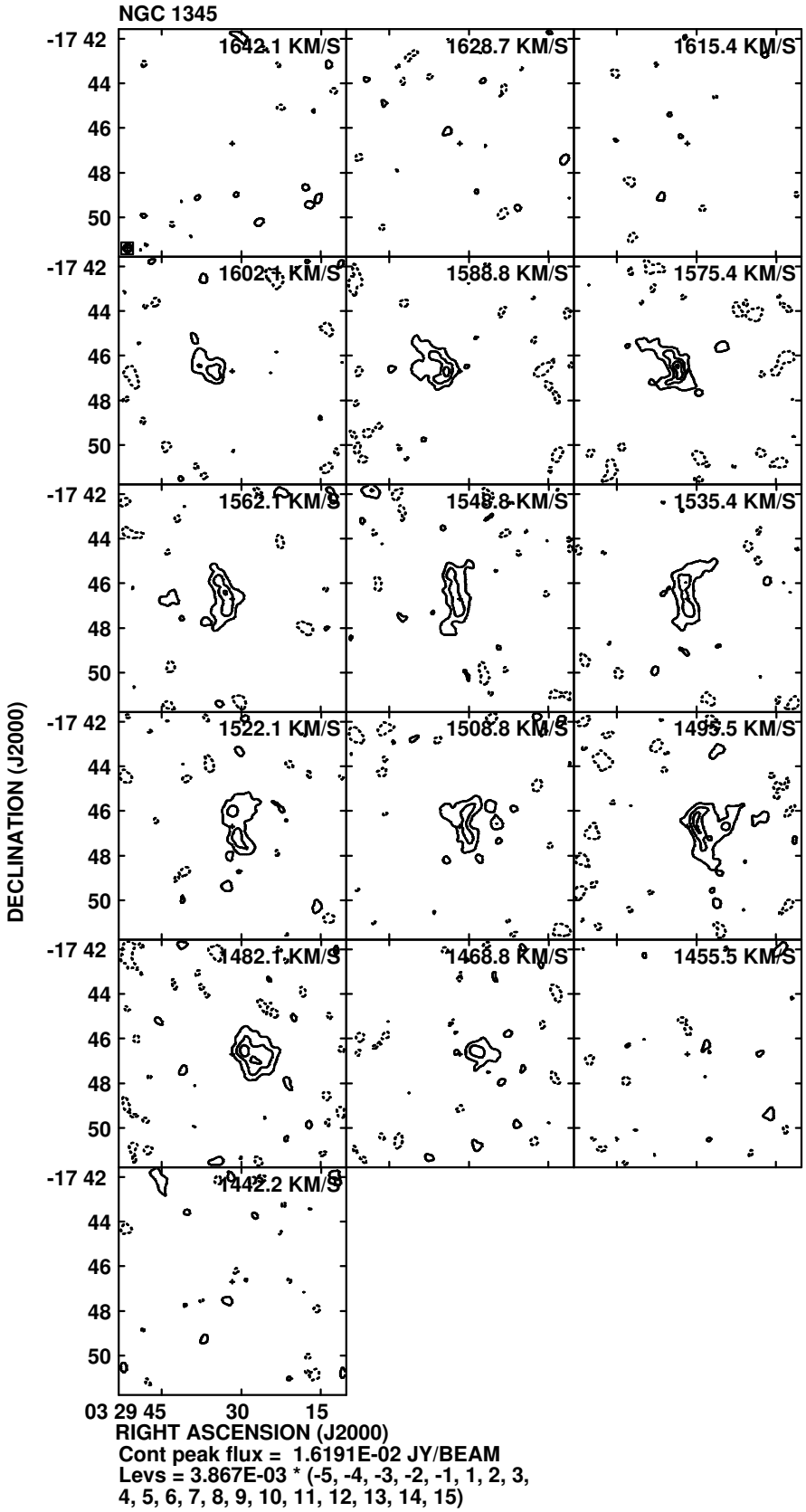
NGC 1345
1642.1 KM/S
1628.7 KM/S
1615.4 KM/S
1602.1 KM/S
1588.8 KM/S
1575.4 KM/S
1562.1 KM/S
1548.8 KM/S
1535.4 KM/S
1522.1 KM/S
1508.8 KM/S
1495.5 KM/S
1482.1 KM/S
1468.8 KM/S
1455.5 KM/S
1442.2 KM/S
-17 42
44
46
48
50
03 29 45
30
15
DECLINATION (J2000)
RIGHT ASCENSION (J2000)
Cont peak flux = 1.6191E-02 JY/BEAM
Levs = 3.867E-03 * (-5, -4, -3, -2, -1, 1, 2, 3, 4, 5, 6, 7, 8, 9, 10, 11, 12, 13, 14, 15)

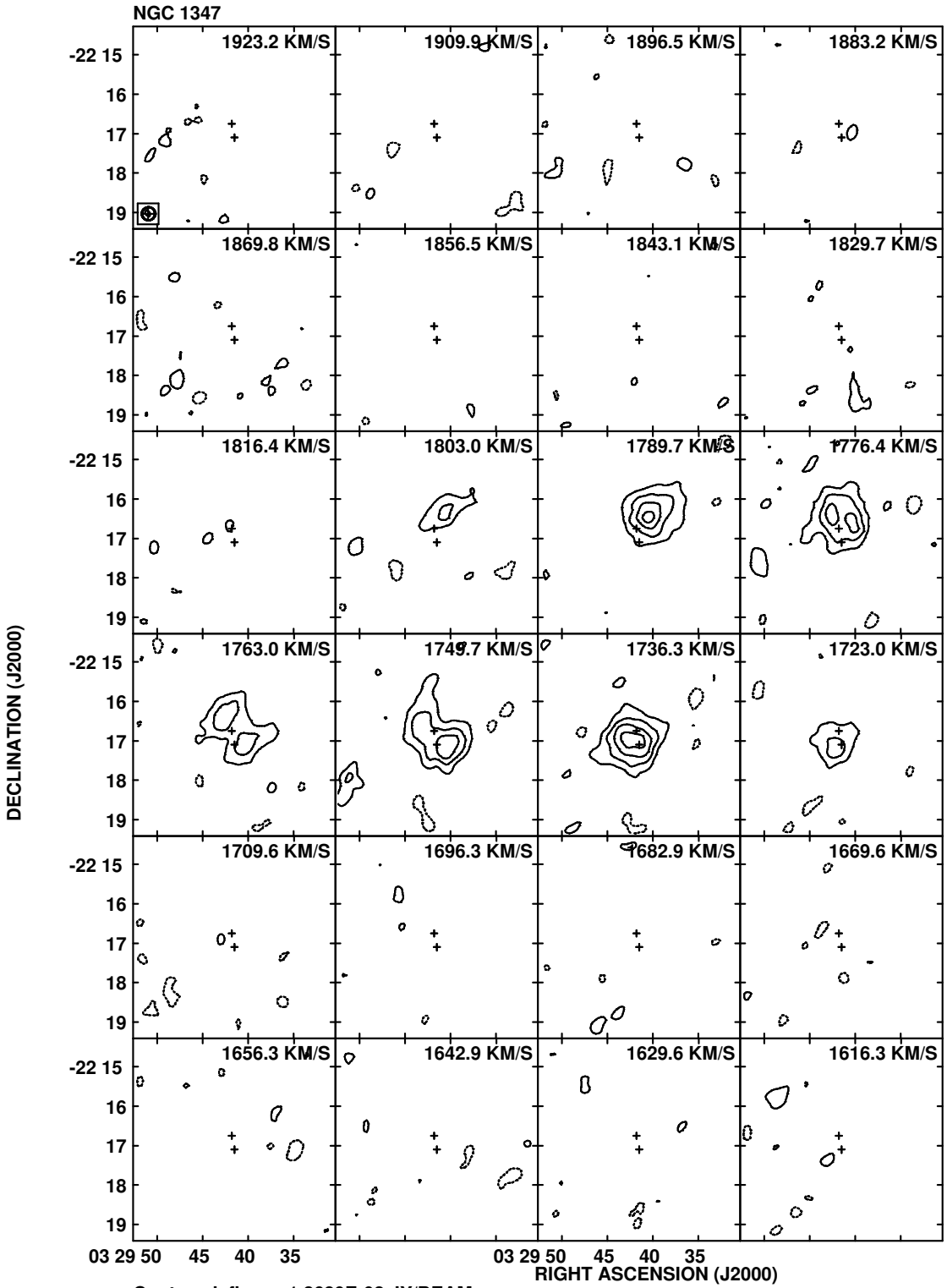

Cont peak flux = 1.3689E-02 JY/BEAM
Levs = 3.007E-03 * (-5, -4, -3, -2, -1, 1, 2, 3, 4, 5, 6, 7, 8, 9, 10, 11, 12, 13, 14, 15)

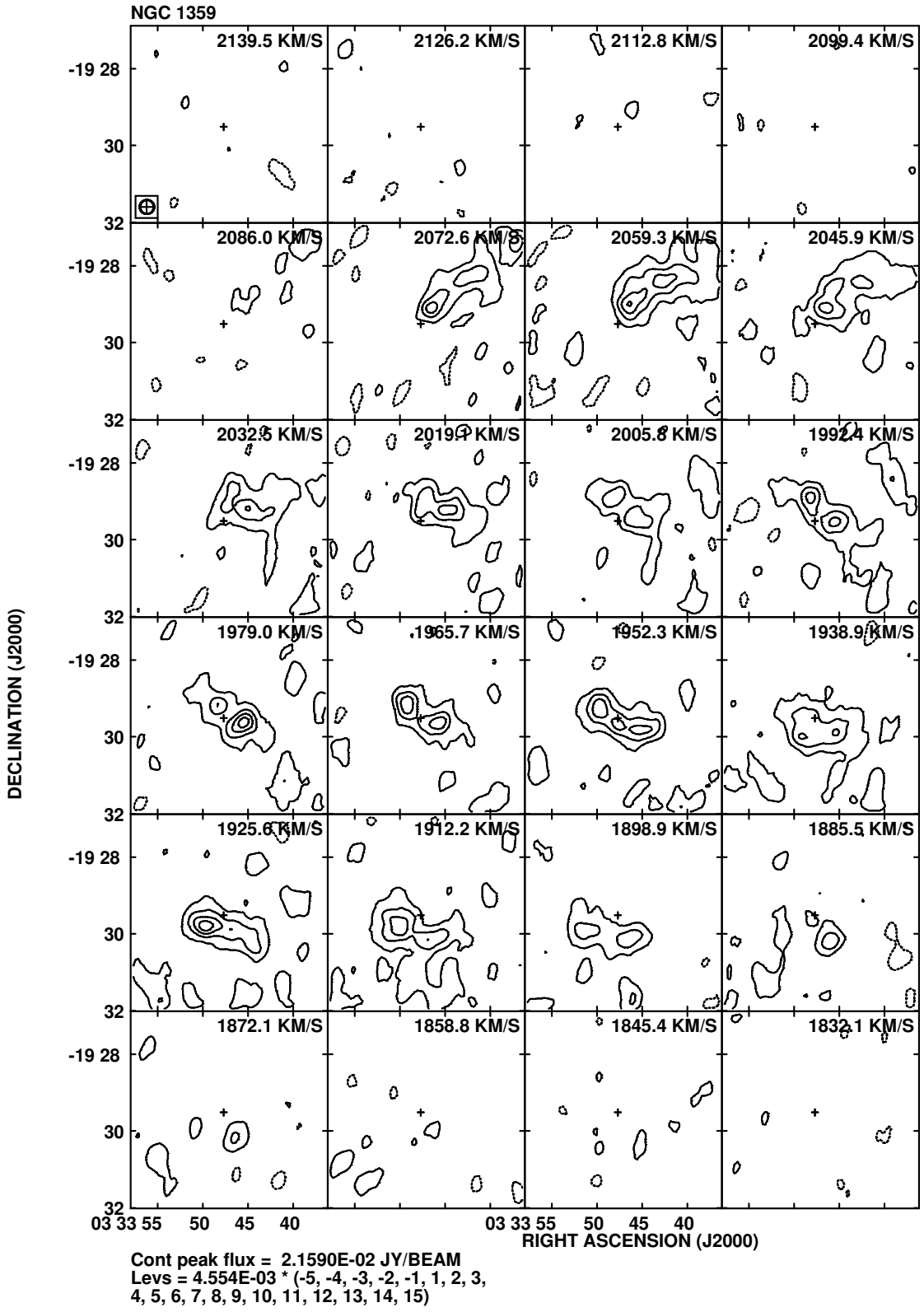

Cont peak flux = 2.1590E-02 JY/BEAM
Levs = 4.554E-03 * (-5, -4, -3, -2, -1, 1, 2, 3, 4, 5, 6, 7, 8, 9, 10, 11, 12, 13, 14, 15)

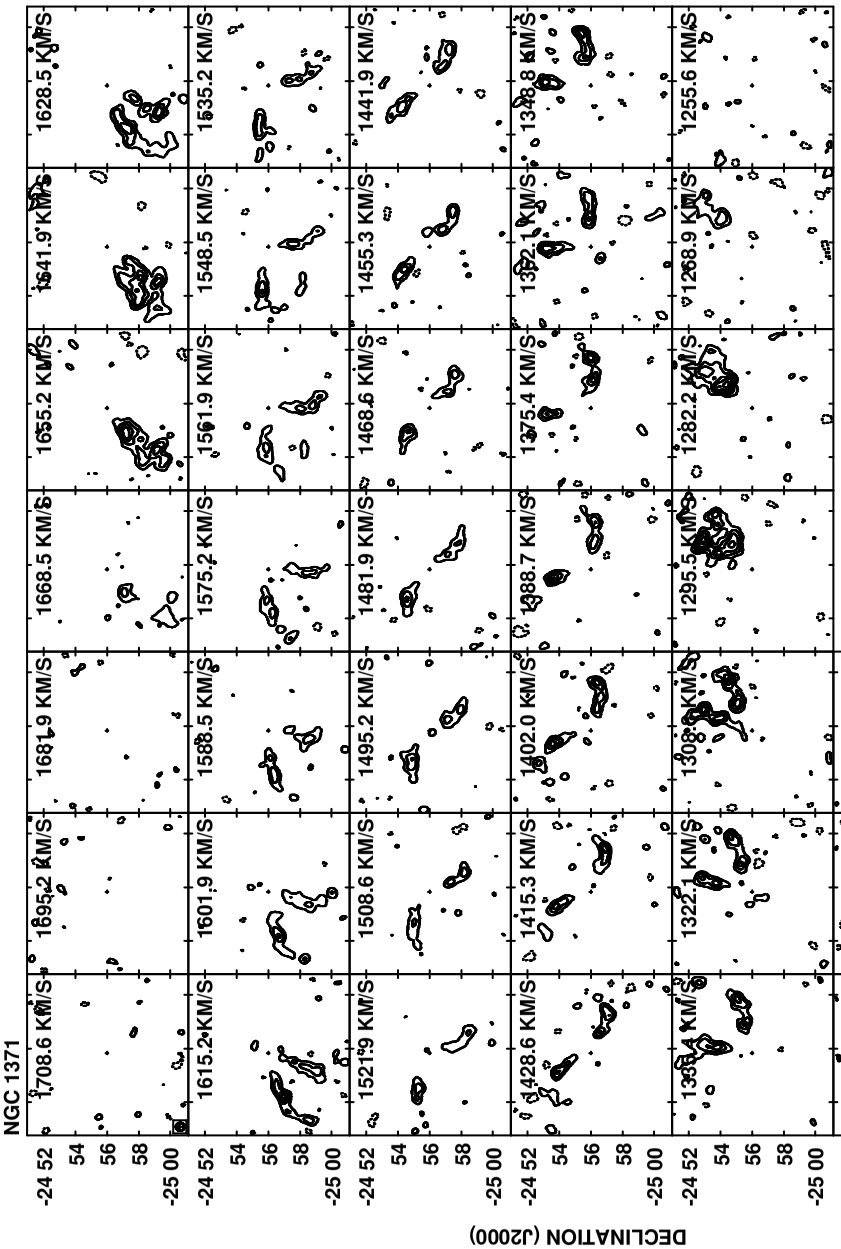
NGC 1371
1708.6 KM/S
1695.2 KM/S
1681.9 KM/S
1668.5 KM/S
1655.2 KM/S
1641.9 KM/S
1628.5 KM/S
1615.2 KM/S
1601.9 KM/S
1588.5 KM/S
1575.2 KM/S
1561.9 KM/S
1548.5 KM/S
1535.2 KM/S
1521.9 KM/S
1508.6 KM/S
1495.2 KM/S
1481.9 KM/S
1468.6 KM/S
1455.3 KM/S
1441.9 KM/S
1428.6 KM/S
1415.3 KM/S
1402.0 KM/S
1388.7 KM/S
1375.4 KM/S
1362.1 KM/S
1348.8 KM/S
1335.4 KM/S
1322.1 KM/S
1308.8 KM/S
1295.5 KM/S
1282.2 KM/S
1268.9 KM/S
1255.6 KM/S
1242.3 KM/S
1229.0 KM/S
1215.7 KM/S
-24 52
54
56
58
-25 00
03 35 15
0034 45
DECLINATION (J2000)
RIGHT ASCENSION (J2000)
Cont peak flux = 1.8066E-02 JY/BEAM
Levs = 3.337E-03 * (-5, -4, -3, -2, -1, 1, 2, 3,
4, 5, 6, 7, 8, 9, 10, 11, 12, 13, 14, 15)

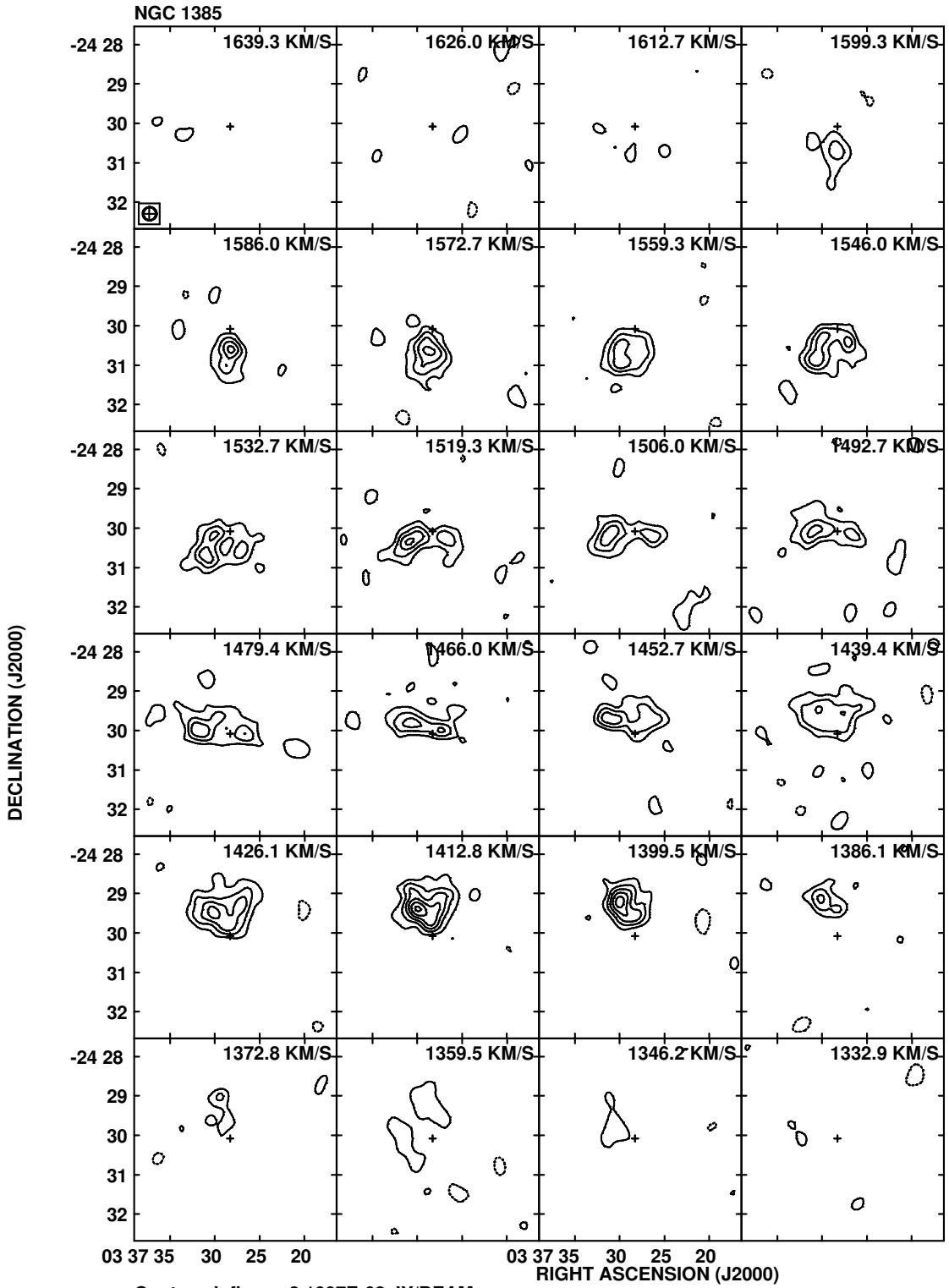

Cont peak flux = 2.1097E-02 JY/BEAM
Levs = 3.361E-03 * (-5, -4, -3, -2, -1, 1, 2, 3, 4, 5, 6, 7, 8, 9, 10, 11, 12, 13, 14, 15)

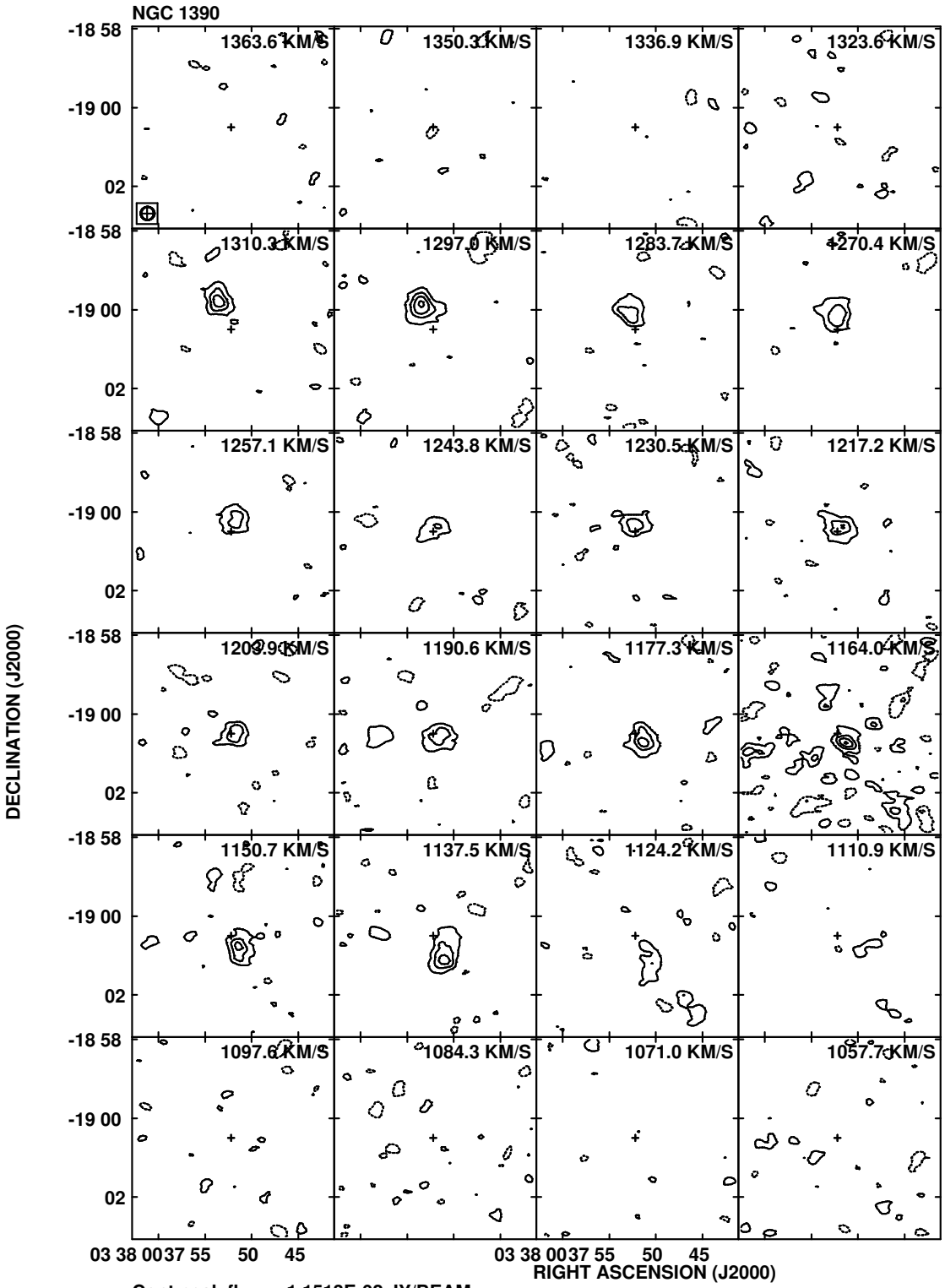

Cont peak flux = 1.1513E-02 JY/BEAM
Levs = 2.726E-03 * (-5, -4, -3, -2, -1, 1, 2, 3, 4, 5, 6, 7, 8, 9, 10, 11, 12, 13, 14, 15)

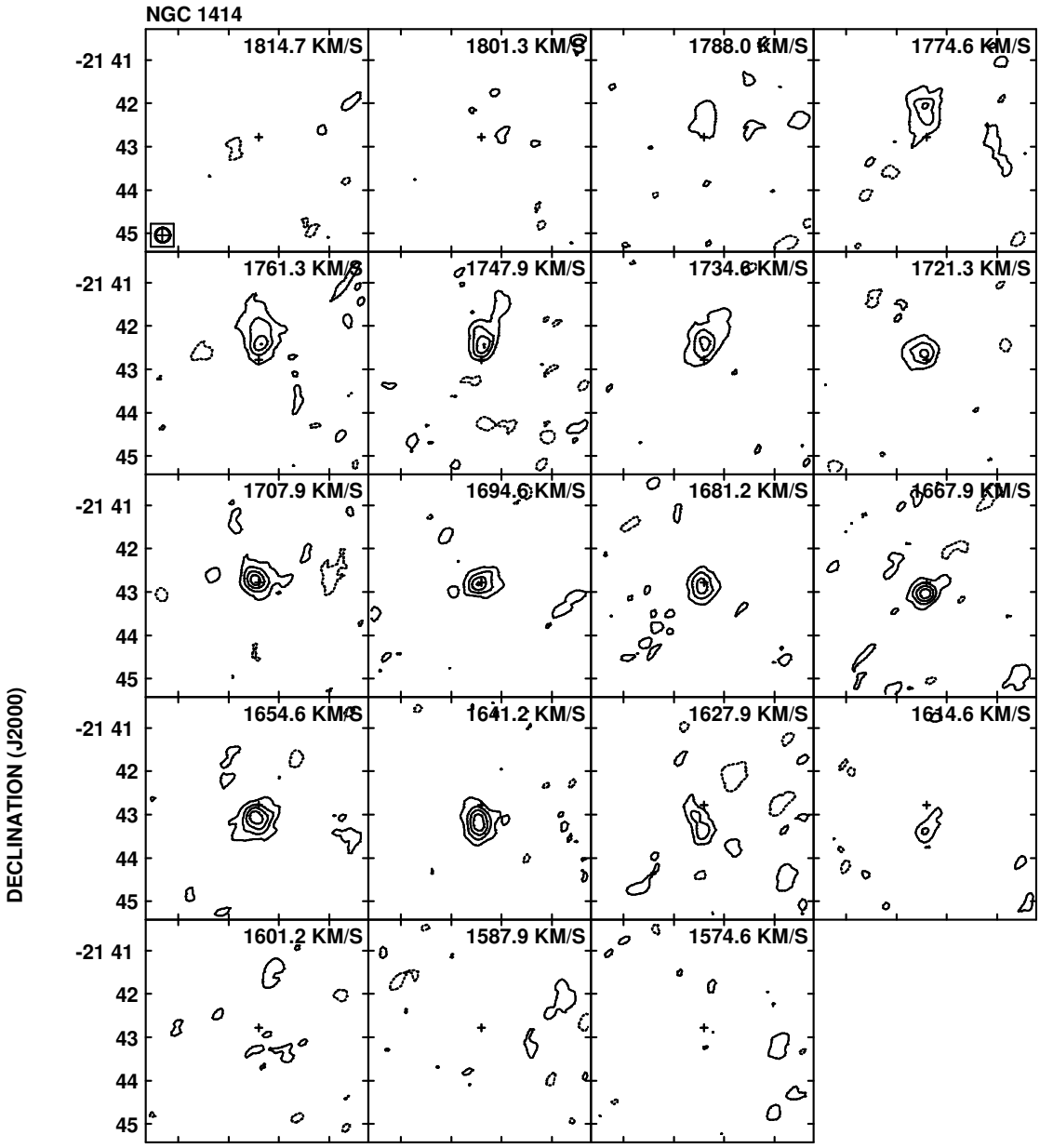

Cont peak flux = 1.1460E-02 JY/BEAM
Levs = 2.343E-03 * (-5, -4, -3, -2, -1, 1, 2, 3, 4, 5, 6, 7, 8, 9, 10, 11, 12, 13, 14, 15)

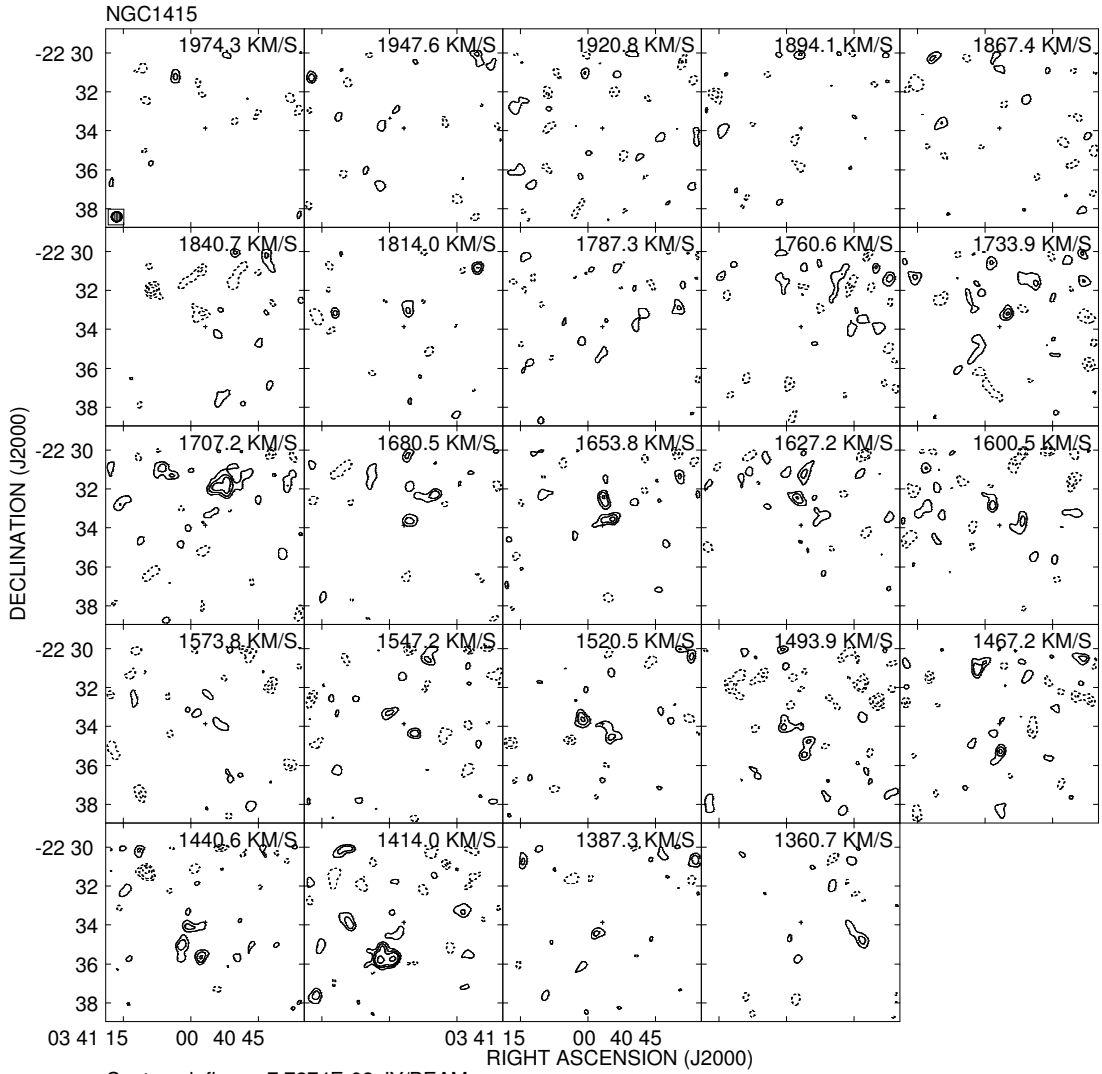

Cont peak flux = 7.7274E-03 JY/BEAM
Levs = 2.289E-03 * (-3, -2, -1.50, -1, 1, 1.500, 2, 3, 4, 6, 8, 12)

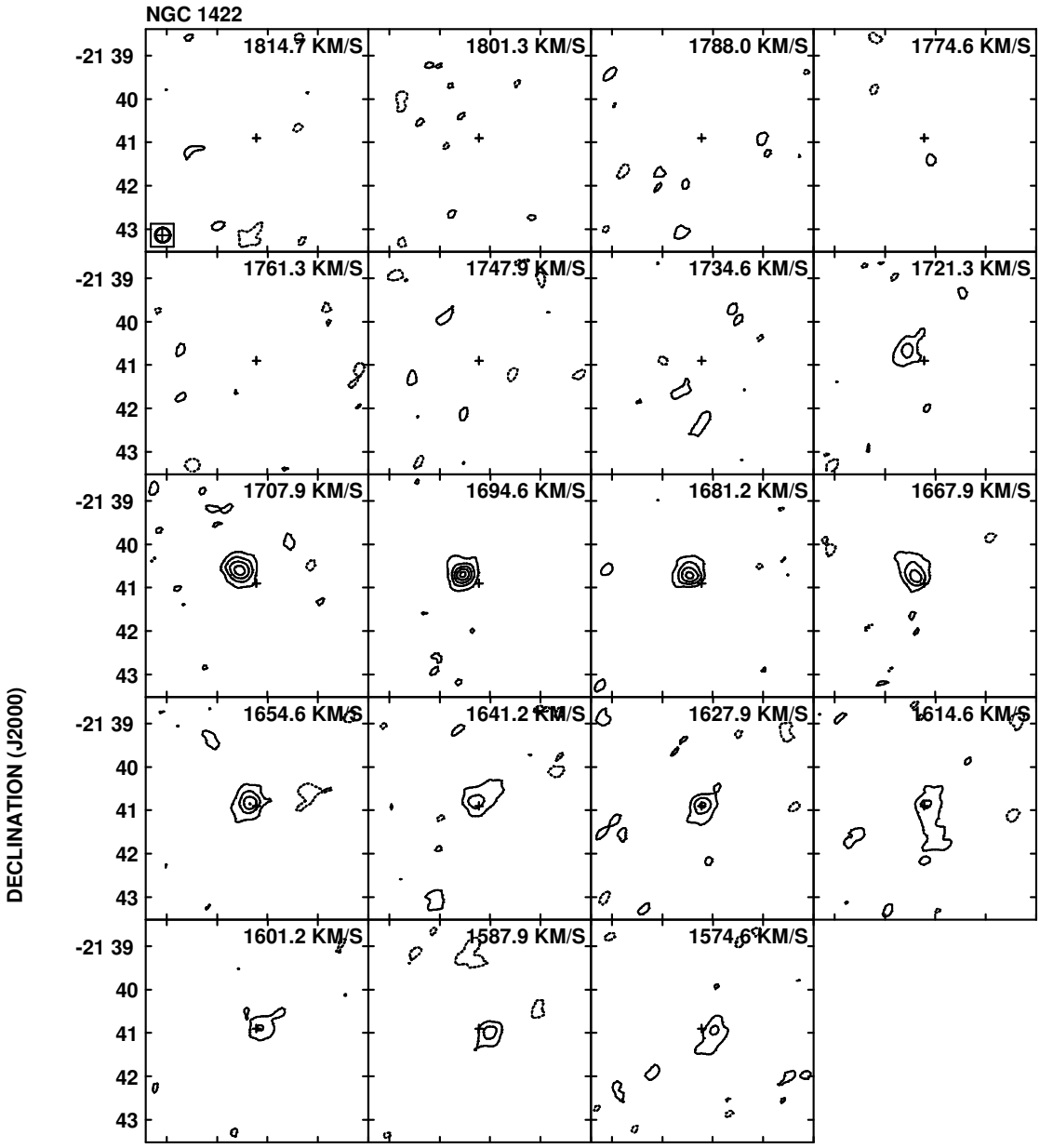

Cont peak flux = 1.4029E-02 JY/BEAM
Levs = 2.623E-03 * (-5, -4, -3, -2, -1, 1, 2, 3, 4, 5, 6, 7, 8, 9, 10, 11, 12, 13, 14, 15)

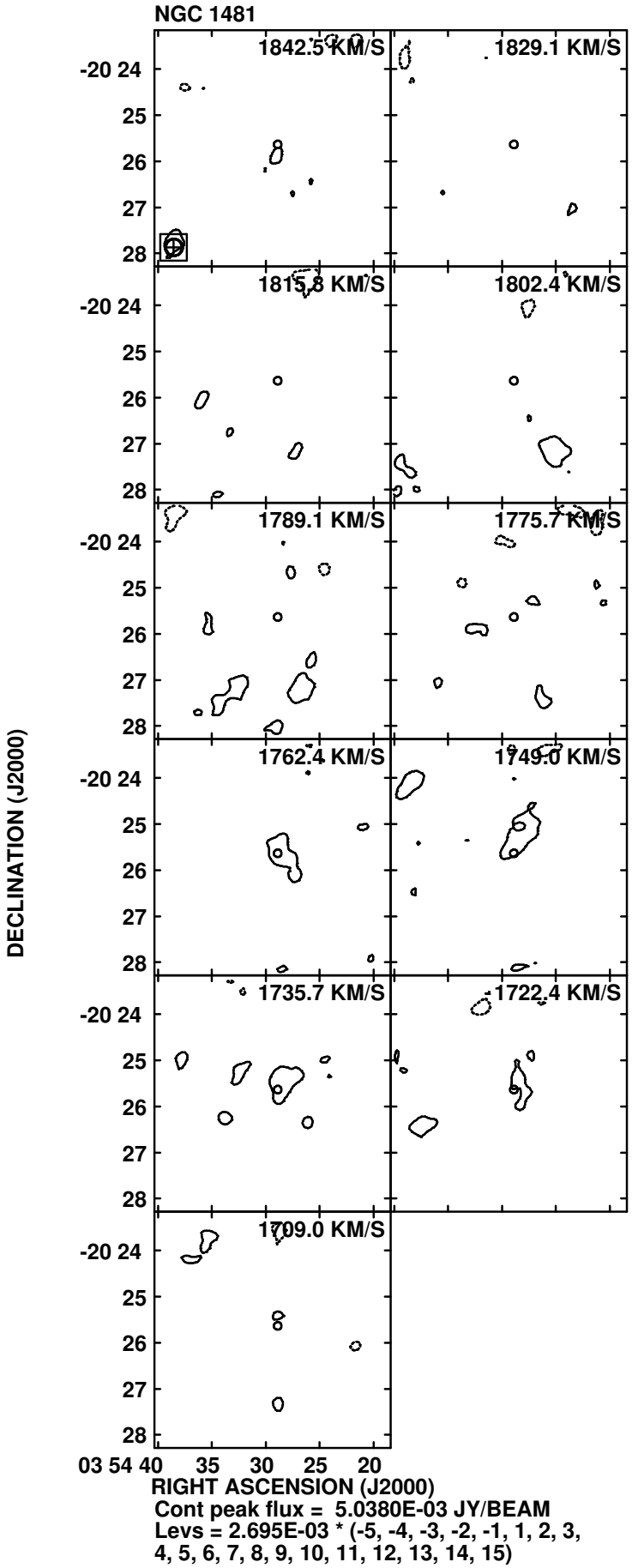
NGC 1481
1842.5 KM/S
1829.1 KM/S
1815.8 KM/S
1802.4 KM/S
1789.1 KM/S
1775.7 KM/S
1762.4 KM/S
1749.0 KM/S
1735.7 KM/S
1722.4 KM/S
1709.0 KM/S
-20 24
25
26
27
28
DECLINATION (J2000)
03 54 40 35 30 25 20
RIGHT ASCENSION (J2000)
Cont peak flux = 5.0380E-03 JY/BEAM
Levs = 2.695E-03 * (-5, -4, -3, -2, -1, 1, 2, 3, 4, 5, 6, 7, 8, 9, 10, 11, 12, 13, 14, 15)

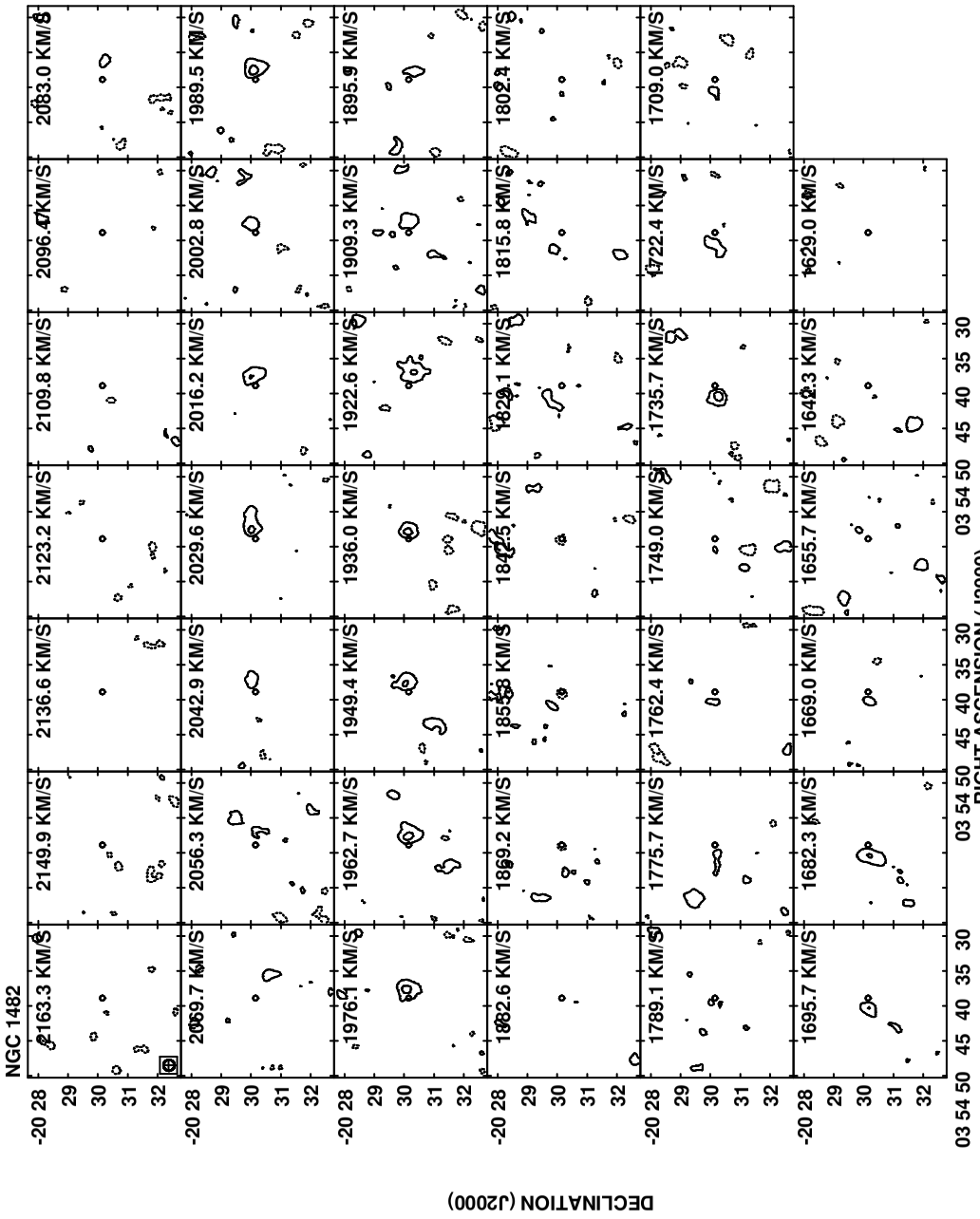
NGC 1482
2163.3 KM/S
2149.9 KM/S
2136.6 KM/S
2123.2 KM/S
2109.8 KM/S
2096.4 KM/S
2083.0 KM/S
2069.7 KM/S
2056.3 KM/S
2042.9 KM/S
2029.6 KM/S
2016.2 KM/S
2002.8 KM/S
1989.5 KM/S
1976.1 KM/S
1962.7 KM/S
1949.4 KM/S
1936.0 KM/S
1922.6 KM/S
1909.3 KM/S
1895.9 KM/S
1882.6 KM/S
1869.2 KM/S
1855.8 KM/S
1842.5 KM/S
1829.1 KM/S
1815.8 KM/S
1802.4 KM/S
1789.1 KM/S
1775.7 KM/S
1762.4 KM/S
1749.0 KM/S
1735.7 KM/S
1722.4 KM/S
1709.0 KM/S
1695.7 KM/S
1682.3 KM/S
1669.0 KM/S
1655.7 KM/S
1642.3 KM/S
1629.0 KM/S
-20 28
29
30
31
32
03 54 50
45
40
35
30
DECLINATION (J2000)
RIGHT ASCENSION (J2000)
Cont peak flux = 7.2960E-03 JY/BEAM
Levs = 2.609E-03 * (-5, -4, -3, -2, -1, 1, 2, 3,
4, 5, 6, 7, 8, 9, 10, 11, 12, 13, 14, 15)

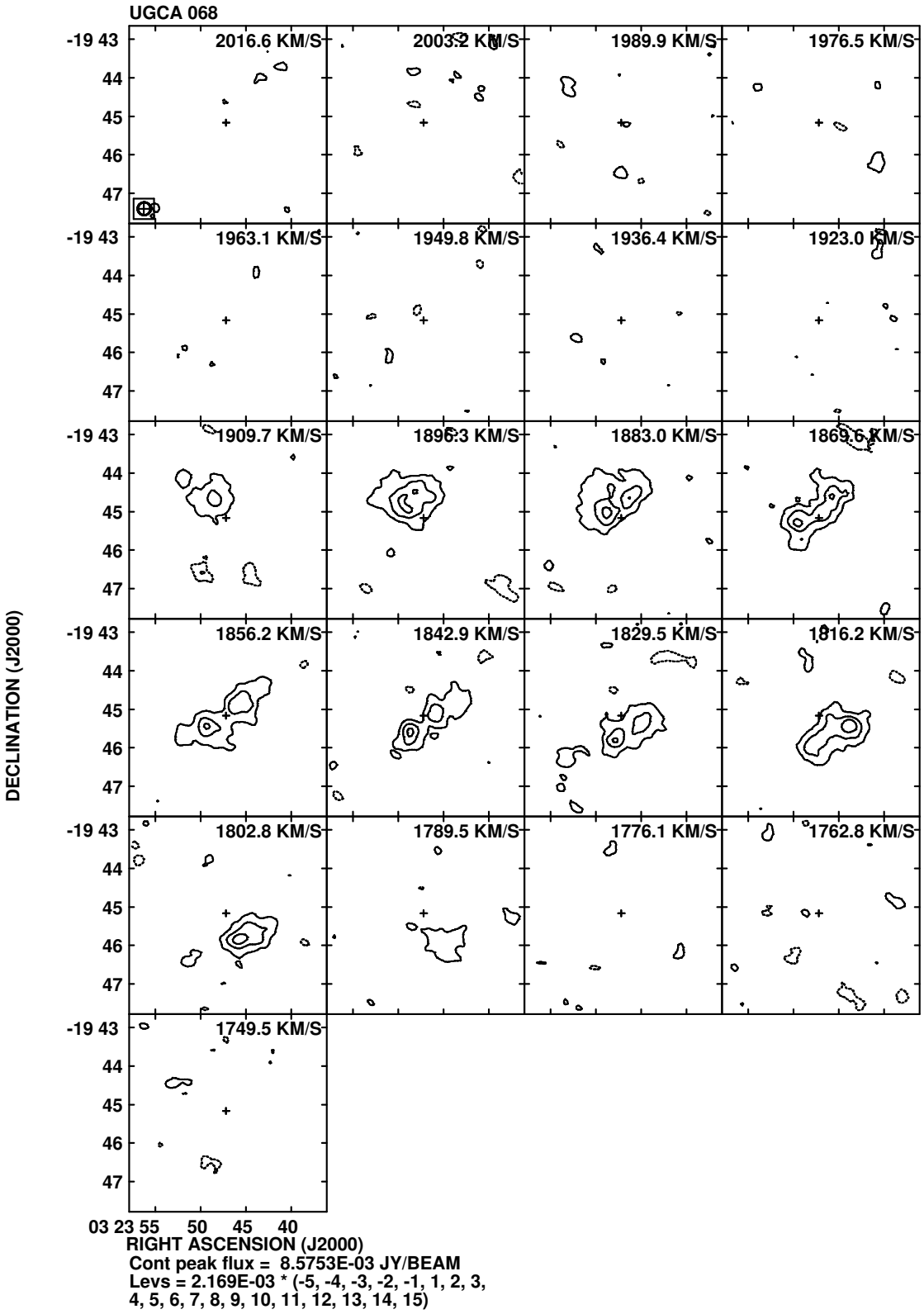
UGCA 068
2016.6 KM/S
2003.2 KM/S
1989.9 KM/S
1976.5 KM/S
1963.1 KM/S
1949.8 KM/S
1936.4 KM/S
1923.0 KM/S
1909.7 KM/S
1896.3 KM/S
1883.0 KM/S
1869.6 KM/S
1856.2 KM/S
1842.9 KM/S
1829.5 KM/S
1816.2 KM/S
1802.8 KM/S
1789.5 KM/S
1776.1 KM/S
1762.8 KM/S
1749.5 KM/S
-19 43
44
45
46
47
03 23 55 50 45 40
DECLINATION (J2000)
RIGHT ASCENSION (J2000)
Cont peak flux = 8.5753E-03 JY/BEAM
Levs = 2.169E-03 * (-5, -4, -3, -2, -1, 1, 2, 3, 4, 5, 6, 7, 8, 9, 10, 11, 12, 13, 14, 15)

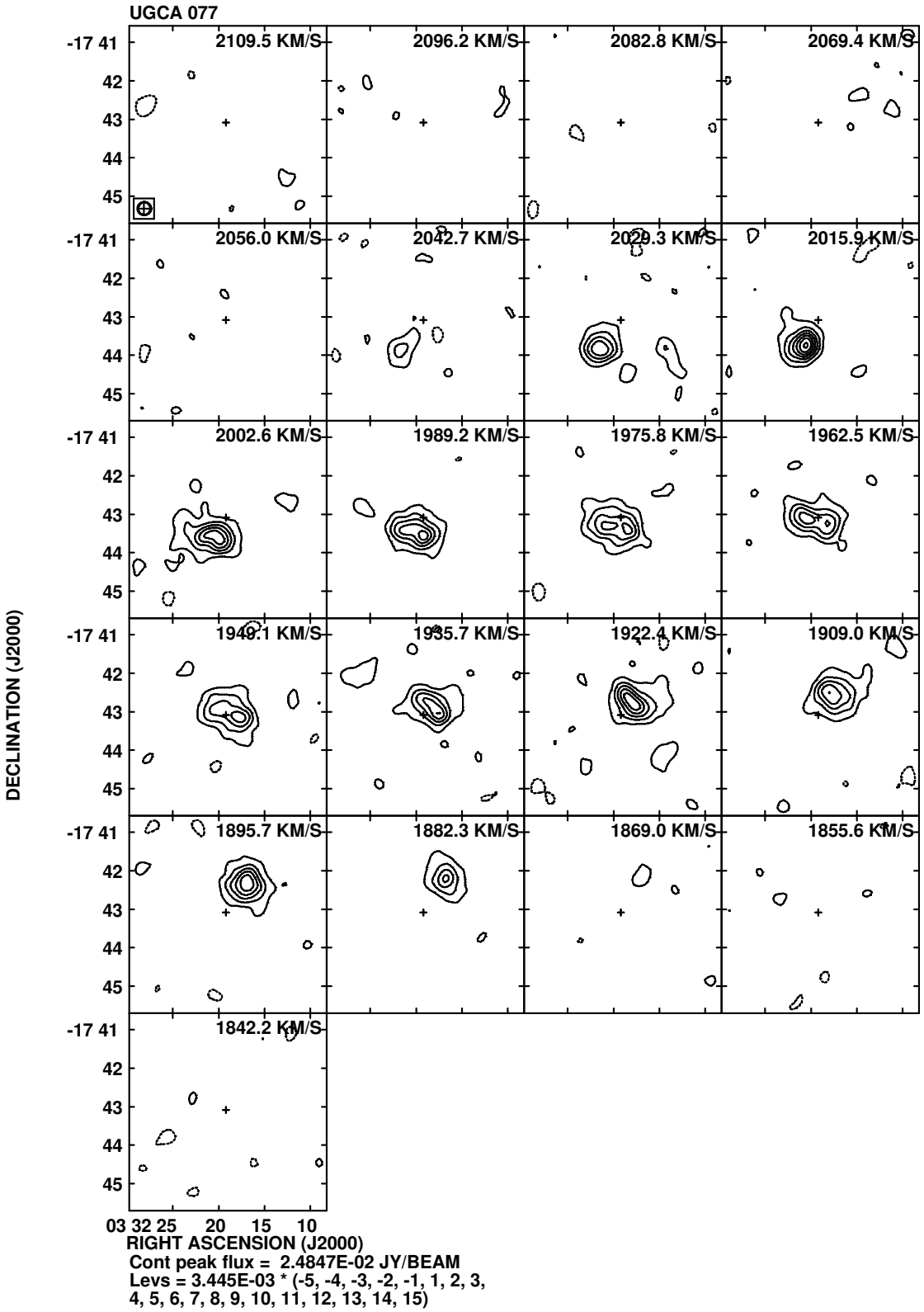
UGCA 077
2109.5 KM/S
2096.2 KM/S
2082.8 KM/S
2069.4 KM/S
2056.0 KM/S
2042.7 KM/S
2029.3 KM/S
2015.9 KM/S
2002.6 KM/S
1989.2 KM/S
1975.8 KM/S
1962.5 KM/S
1949.1 KM/S
1935.7 KM/S
1922.4 KM/S
1909.0 KM/S
1895.7 KM/S
1882.3 KM/S
1869.0 KM/S
1855.6 KM/S
1842.2 KM/S
-17 41
42
43
44
45
DECLINATION (J2000)
03 32 25 20 15 10
RIGHT ASCENSION (J2000)
Cont peak flux = 2.4847E-02 JY/BEAM
Levs = 3.445E-03 * (-5, -4, -3, -2, -1, 1, 2, 3, 4, 5, 6, 7, 8, 9, 10, 11, 12, 13, 14, 15)

The H I Atlas

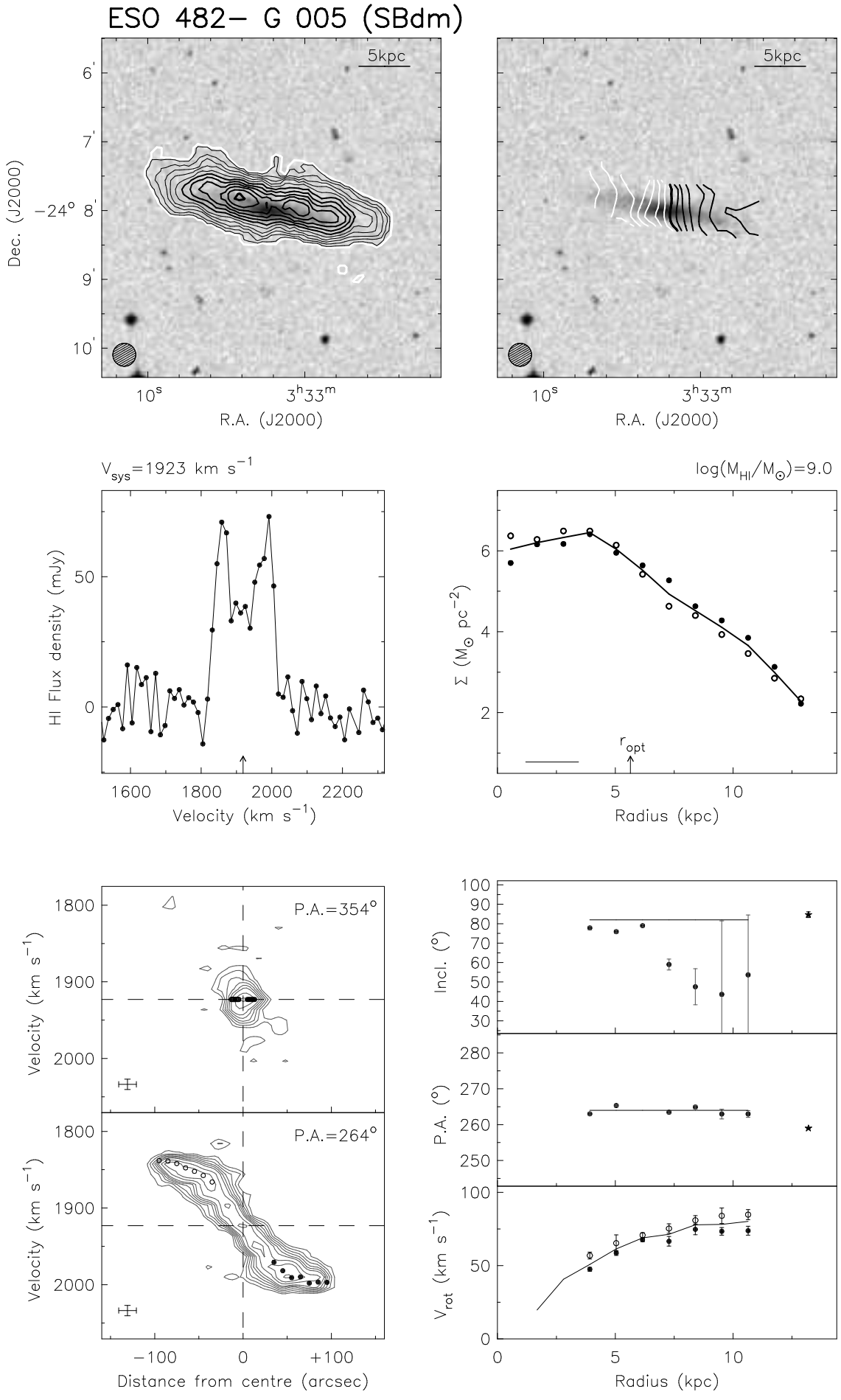
ESO 482− G 005 (SBdm)
5kpc
Dec. (J2000)
−24° 6′
7′
8′
9′
10′
10s
3h33m
R.A. (J2000)
5kpc
10s
3h33m
R.A. (J2000)
Vsys=1923 km s−1
HI Flux density (mJy)
50
0
1600
1800
2000
2200
Velocity (km s−1)
log(MHI/M⊙)=9.0
Σ (M⊙ pc−2)
6
4
2
ropt
0
5
10
Radius (kpc)
P.A.=354°
P.A.=264°
Velocity (km s−1)
1800
1900
2000
−100
0
+100
Distance from centre (arcsec)
Incl. (°)
100
90
80
70
60
50
40
30
P.A. (°)
280
270
260
250
Vrot (km s−1)
100
50
0
0
5
10
Radius (kpc)

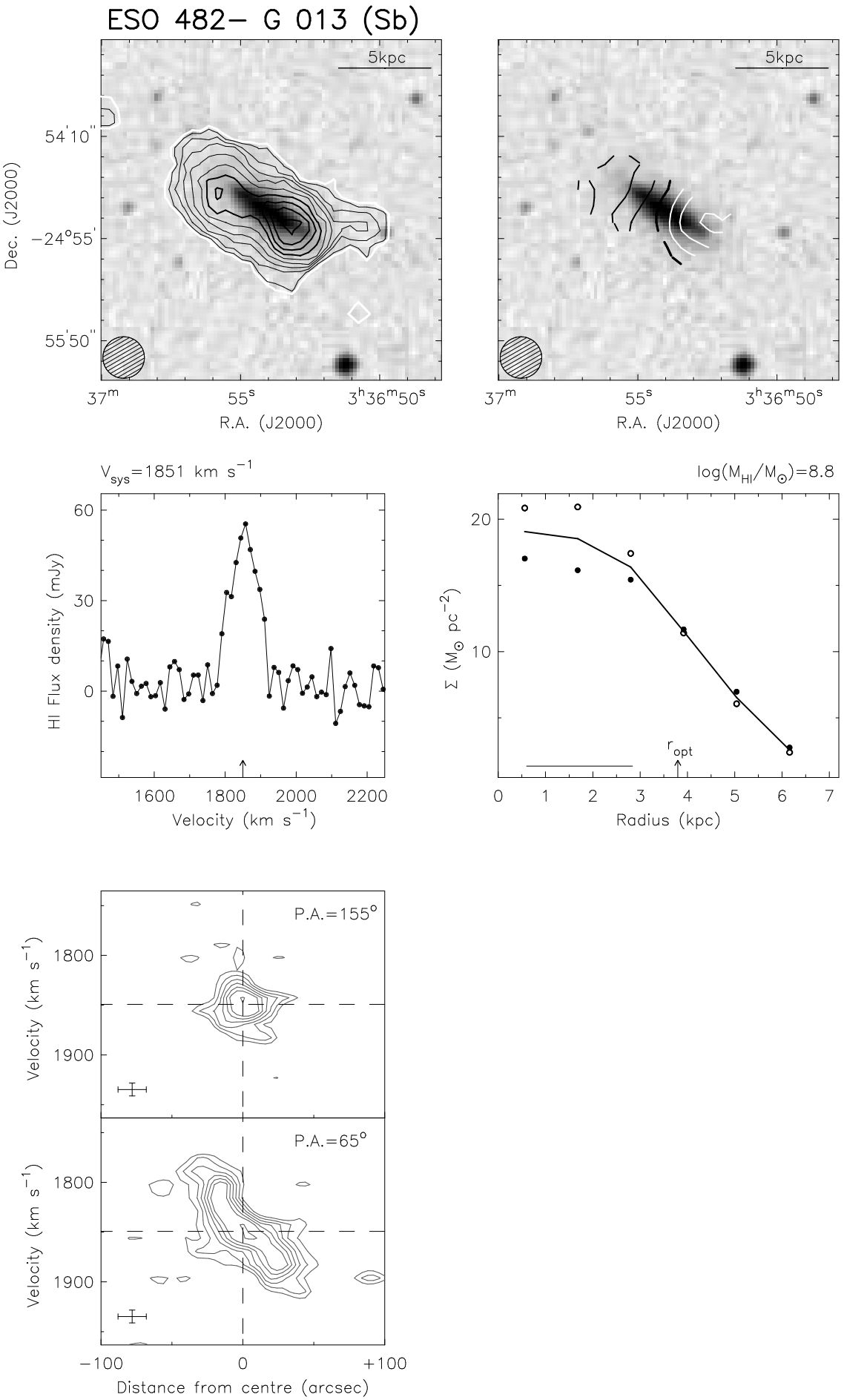
ESO 482− G 013 (Sb)
5kpc
5kpc
54'10"
−24°55'
55'50"
Dec. (J2000)
37m
55s
3h36m50s
R.A. (J2000)
37m
55s
3h36m50s
R.A. (J2000)
Vsys=1851 km s−1
HI Flux density (mJy)
60
30
0
1600
1800
2000
2200
Velocity (km s−1)
log(MHI/M⊙)=8.8
Σ (M⊙ pc−2)
20
10
ropt
0
1
2
3
4
5
6
7
Radius (kpc)
P.A.=155°
Velocity (km s−1)
1800
1900
P.A.=65°
Velocity (km s−1)
1800
1900
−100
0
+100
Distance from centre (arcsec)

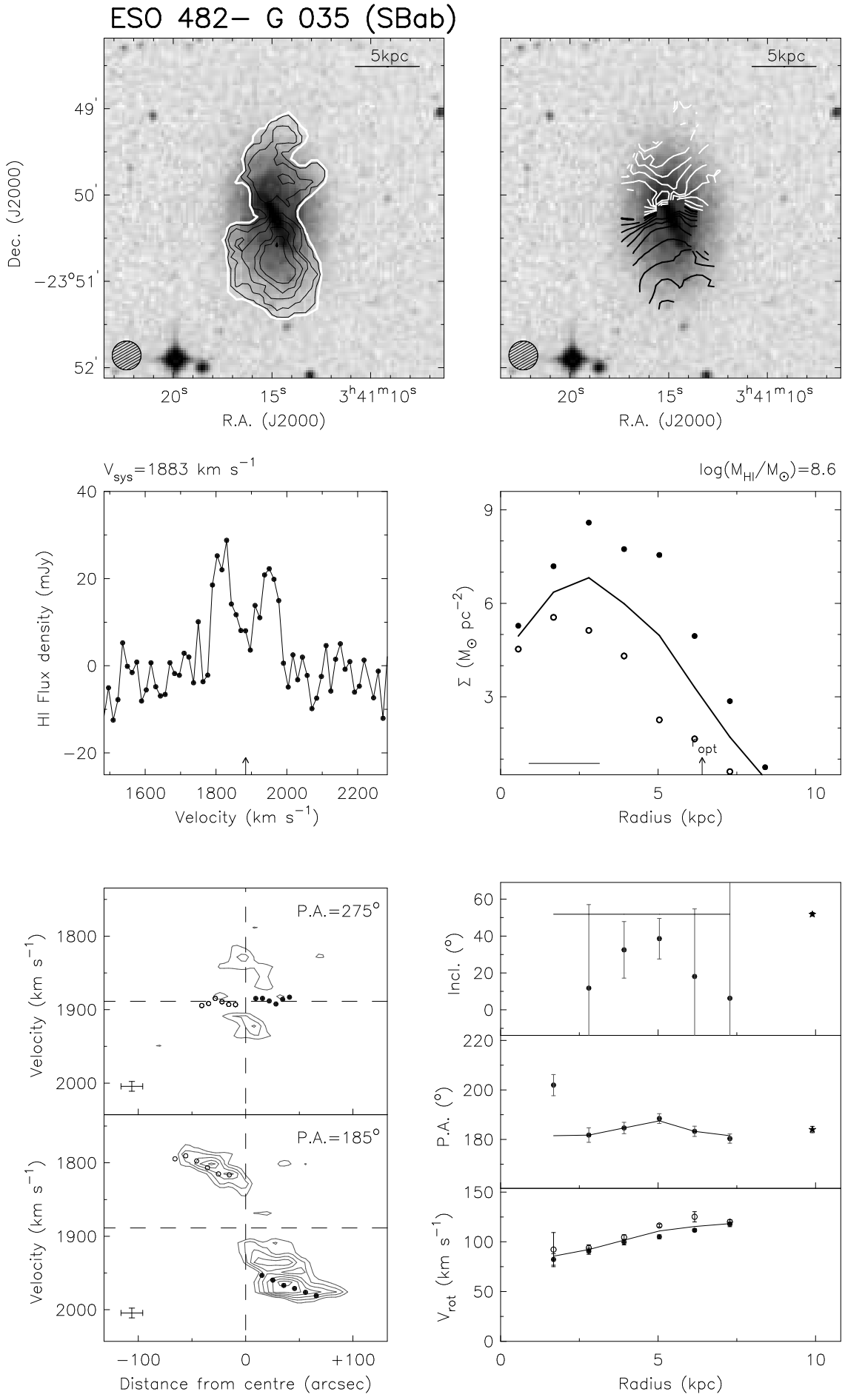
ESO 482− G 035 (SBab)
5kpc
49′
50′
−23°51′
52′
Dec. (J2000)
20s
15s
3h41m10s
R.A. (J2000)
5kpc
20s
15s
3h41m10s
R.A. (J2000)
Vsys=1883 km s−1
HI Flux density (mJy)
Velocity (km s−1)
log(MHI/M⊙)=8.6
Σ (M⊙ pc−2)
ropt
Radius (kpc)
P.A.=275°
P.A.=185°
Velocity (km s−1)
Distance from centre (arcsec)
Incl. (°)
P.A. (°)
Vrot (km s−1)
Radius (kpc)

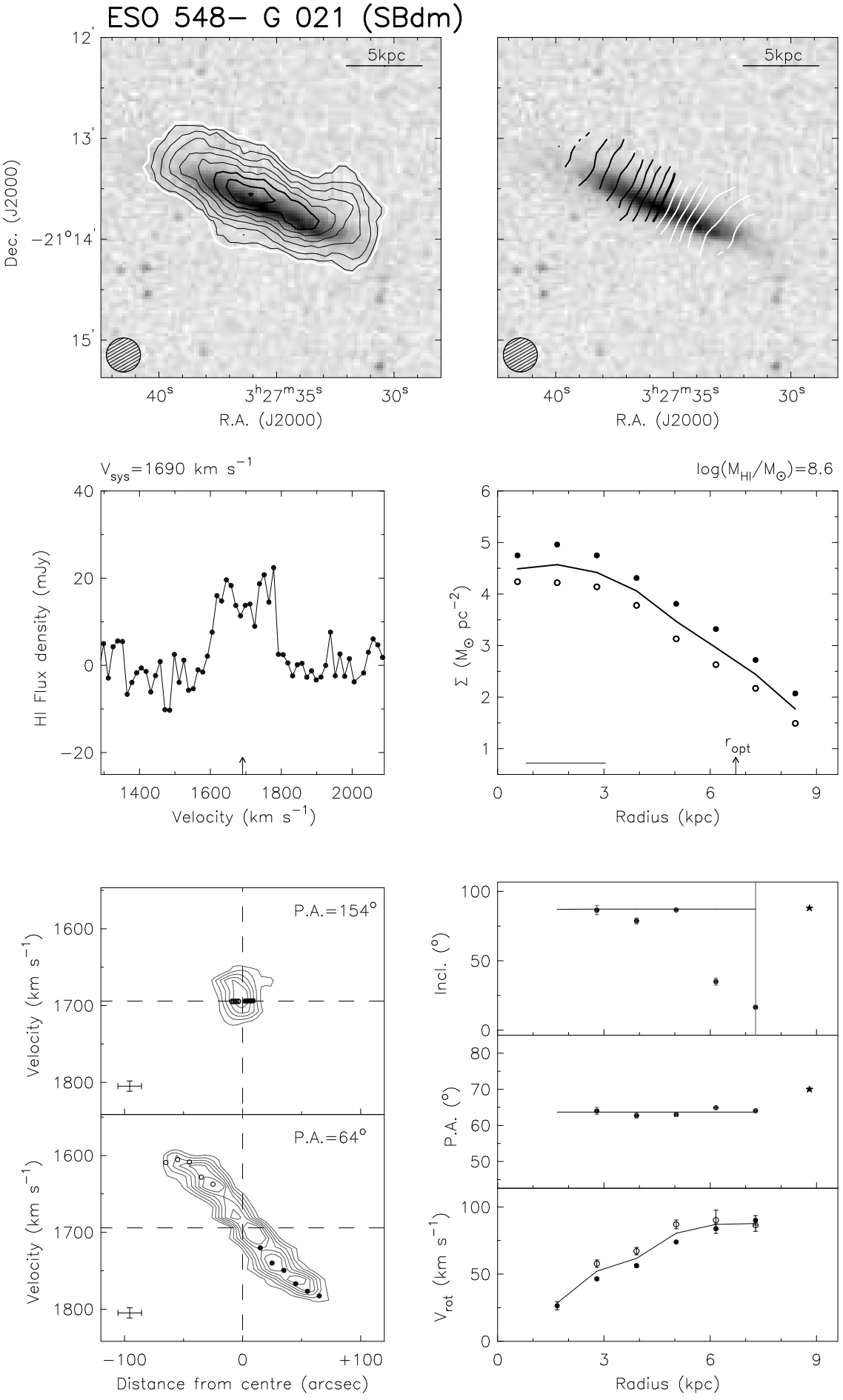
ESO 548− G 021 (SBdm)
5kpc
5kpc
Dec. (J2000)
R.A. (J2000)
R.A. (J2000)
V_{sys}=1690 km s^{-1}
log($M_{HI}/M_\odot$)=8.6
HI Flux density (mJy)
Velocity (km s^{-1})
Σ ($M_\odot$ pc^{-2})
r_{opt}
Radius (kpc)
P.A.=154°
P.A.=64°
Velocity (km s^{-1})
Distance from centre (arcsec)
Incl. (°)
P.A. (°)
V_{rot} (km s^{-1})
Radius (kpc)

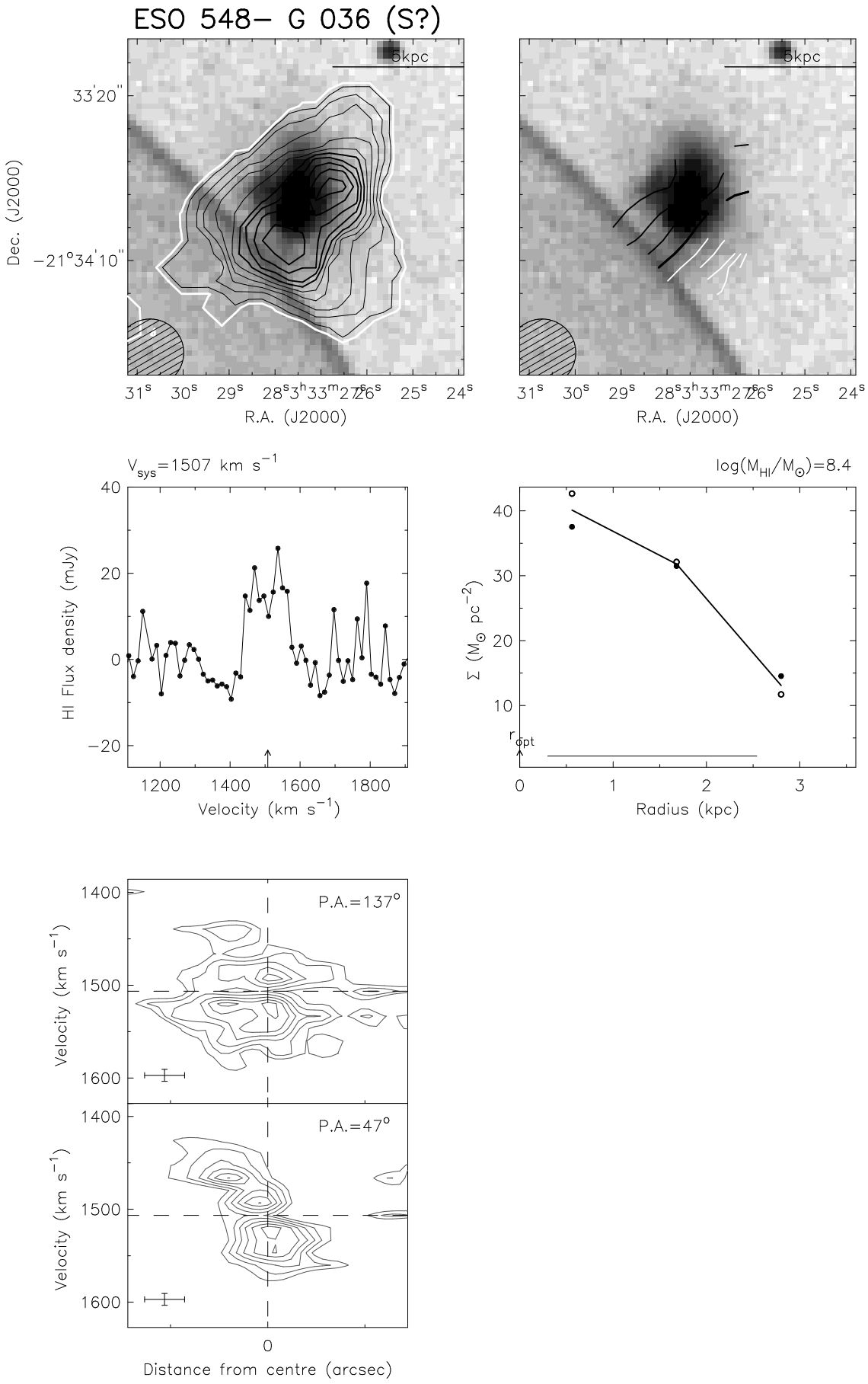
ESO 548– G 036 (S?)
5kpc
33'20"
−21°34'10"
Dec. (J2000)
31s 30s 29s 28s 3h33m27s 26s 25s 24s
R.A. (J2000)
5kpc
31s 30s 29s 28s 3h33m27s 26s 25s 24s
R.A. (J2000)
Vsys=1507 km s−1
HI Flux density (mJy)
40
20
0
−20
1200 1400 1600 1800
Velocity (km s−1)
log(MHI/M⊙)=8.4
Σ (M⊙ pc−2)
40
30
20
10
ropt
0 1 2 3
Radius (kpc)
P.A.=137°
P.A.=47°
Velocity (km s−1)
1400
1500
1600
0
Distance from centre (arcsec)

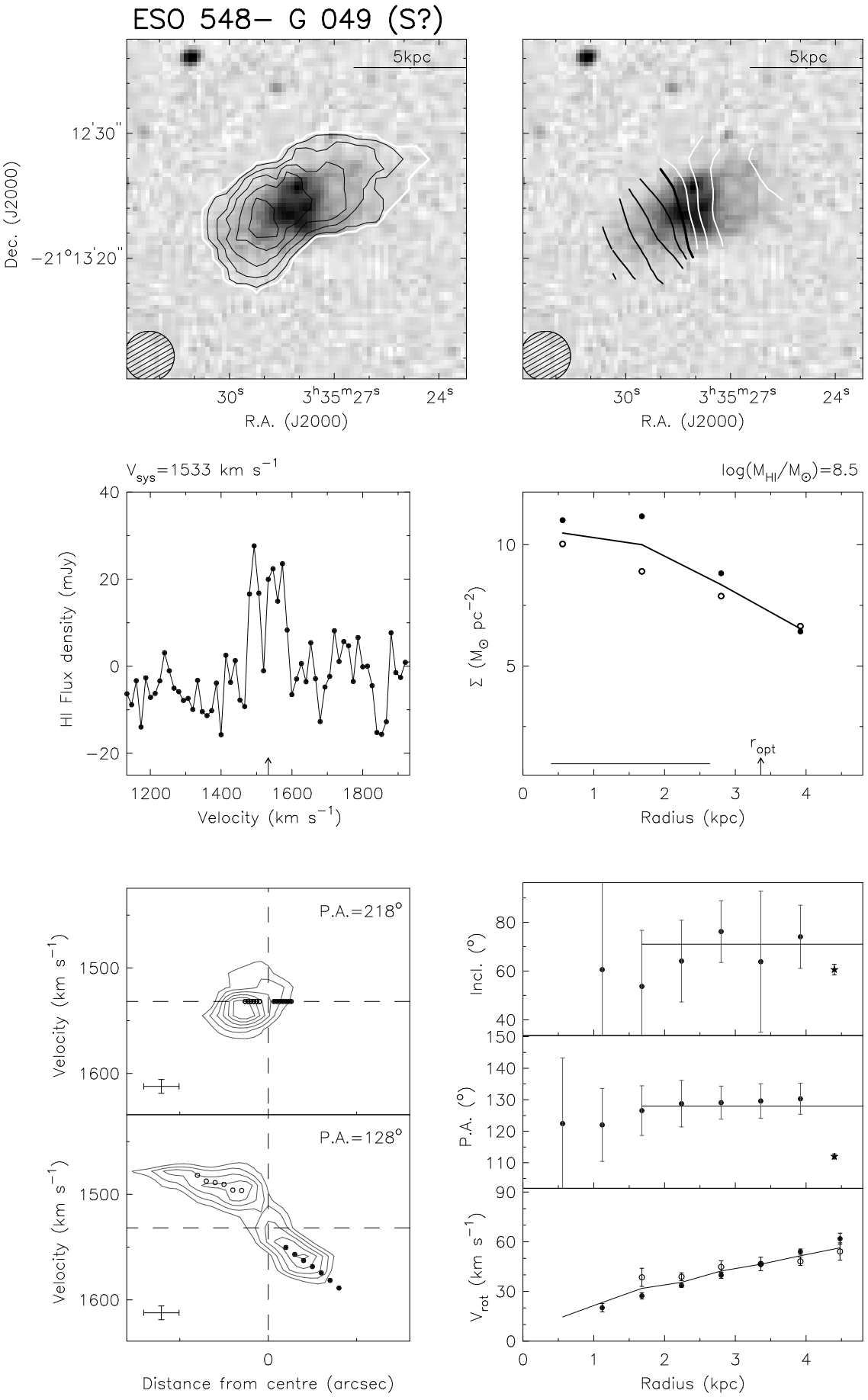
ESO 548− G 049 (S?)
5kpc
12'30"
−21°13'20"
Dec. (J2000)
30s
3h35m27s
24s
R.A. (J2000)
5kpc
30s
3h35m27s
24s
R.A. (J2000)
Vsys=1533 km s−1
HI Flux density (mJy)
Velocity (km s−1)
log(MHI/M⊙)=8.5
Σ (M⊙ pc−2)
ropt
Radius (kpc)
P.A.=218°
P.A.=128°
Velocity (km s−1)
Velocity (km s−1)
Distance from centre (arcsec)
Incl. (°)
P.A. (°)
Vrot (km s−1)
Radius (kpc)

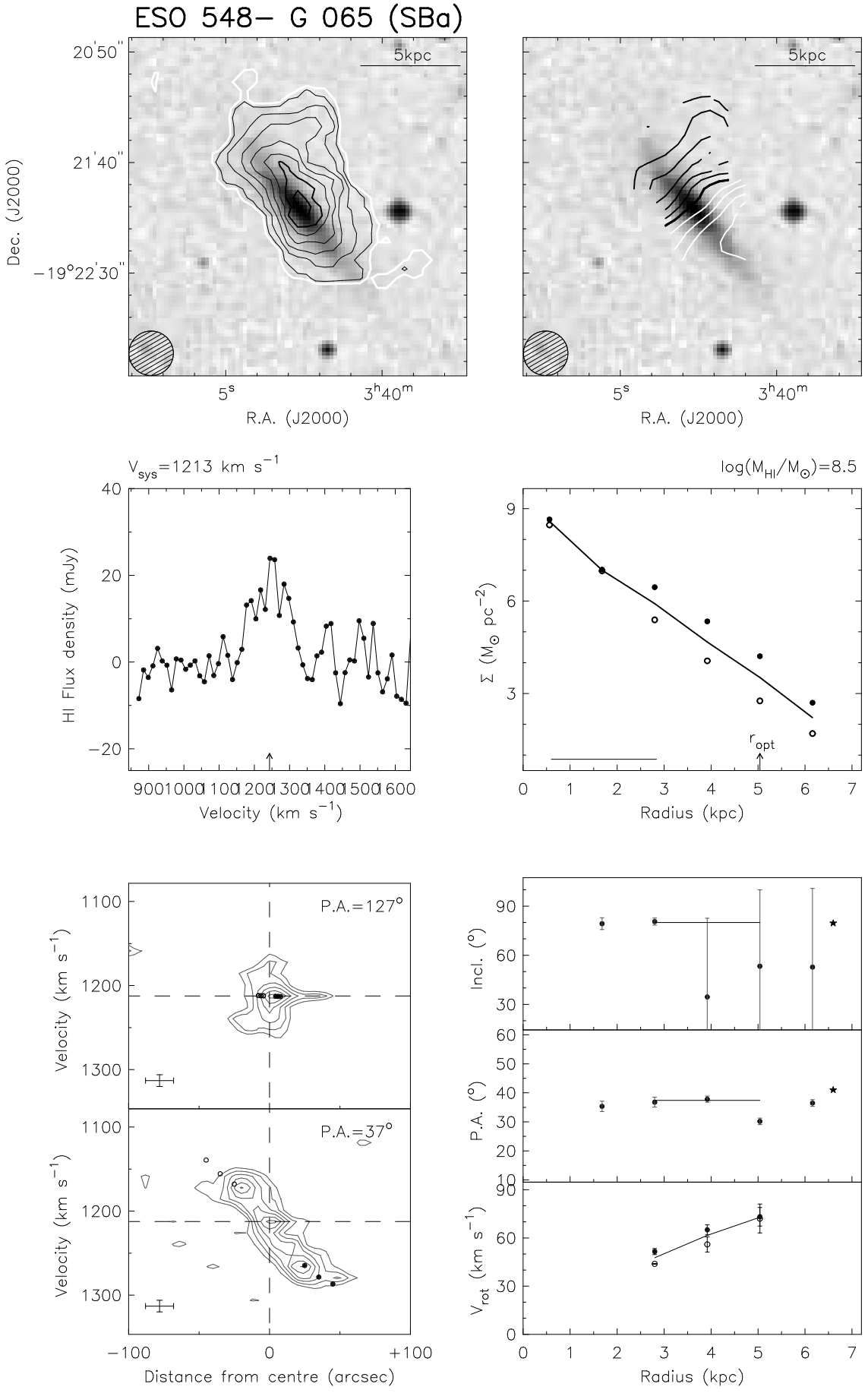
ESO 548− G 065 (SBa)
5kpc
5kpc
20'50"
21'40"
−19°22'30"
Dec. (J2000)
5s
3h40m
R.A. (J2000)
5s
3h40m
R.A. (J2000)
Vsys=1213 km s−1
HI Flux density (mJy)
Velocity (km s−1)
log(MHI/M⊙)=8.5
Σ (M⊙ pc−2)
ropt
Radius (kpc)
P.A.=127°
P.A.=37°
Velocity (km s−1)
Velocity (km s−1)
Distance from centre (arcsec)
Incl. (°)
P.A. (°)
Vrot (km s−1)
Radius (kpc)

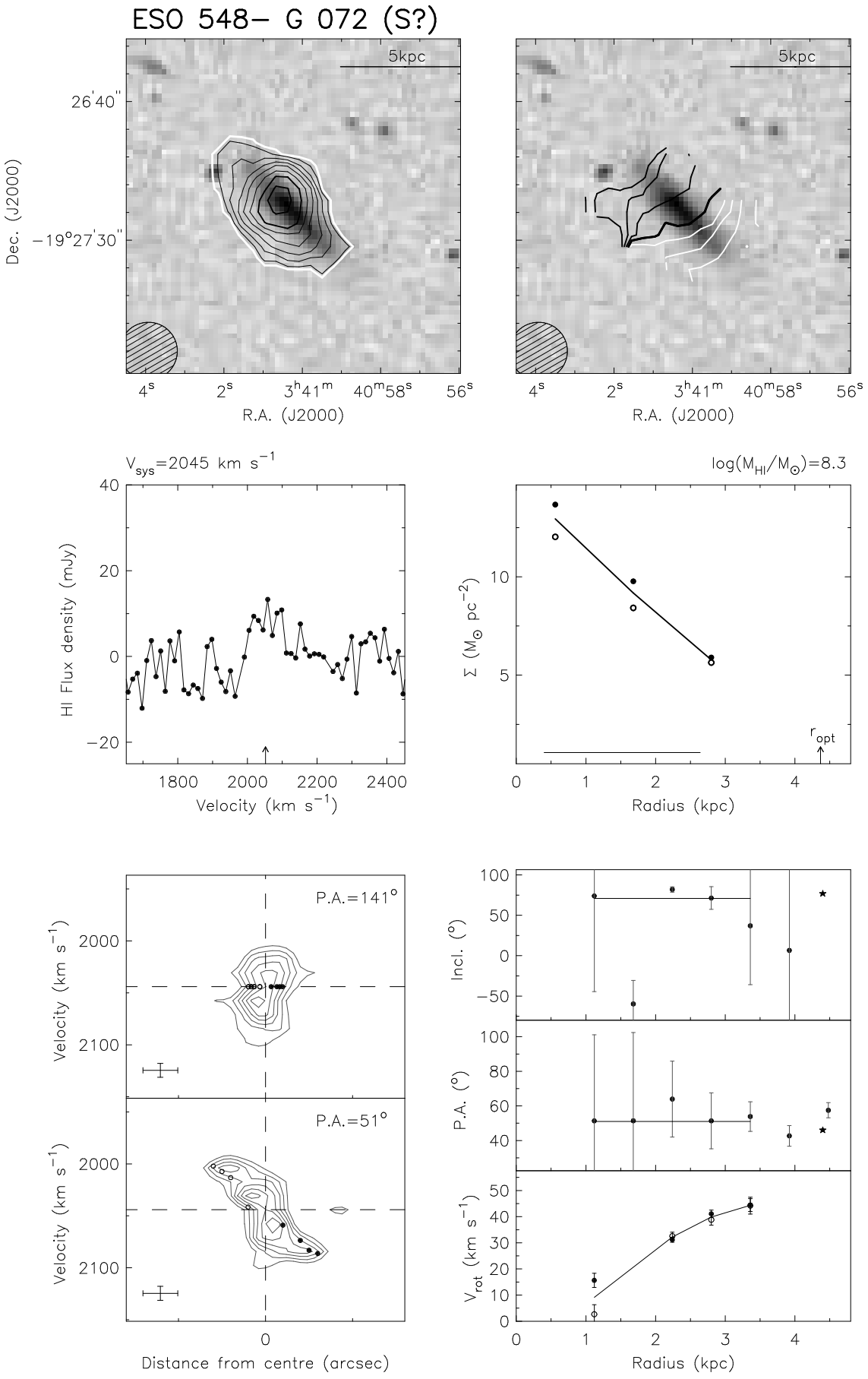
ESO 548– G 072 (S?)
5kpc
5kpc
26'40"
−19°27'30"
Dec. (J2000)
4s
2s
3h41m
40m58s
56s
R.A. (J2000)
Vsys=2045 km s−1
log(MHI/M⊙)=8.3
HI Flux density (mJy)
Velocity (km s−1)
Σ (M⊙ pc−2)
ropt
Radius (kpc)
P.A.=141°
P.A.=51°
Velocity (km s−1)
Distance from centre (arcsec)
Incl. (°)
P.A. (°)
Vrot (km s−1)
Radius (kpc)

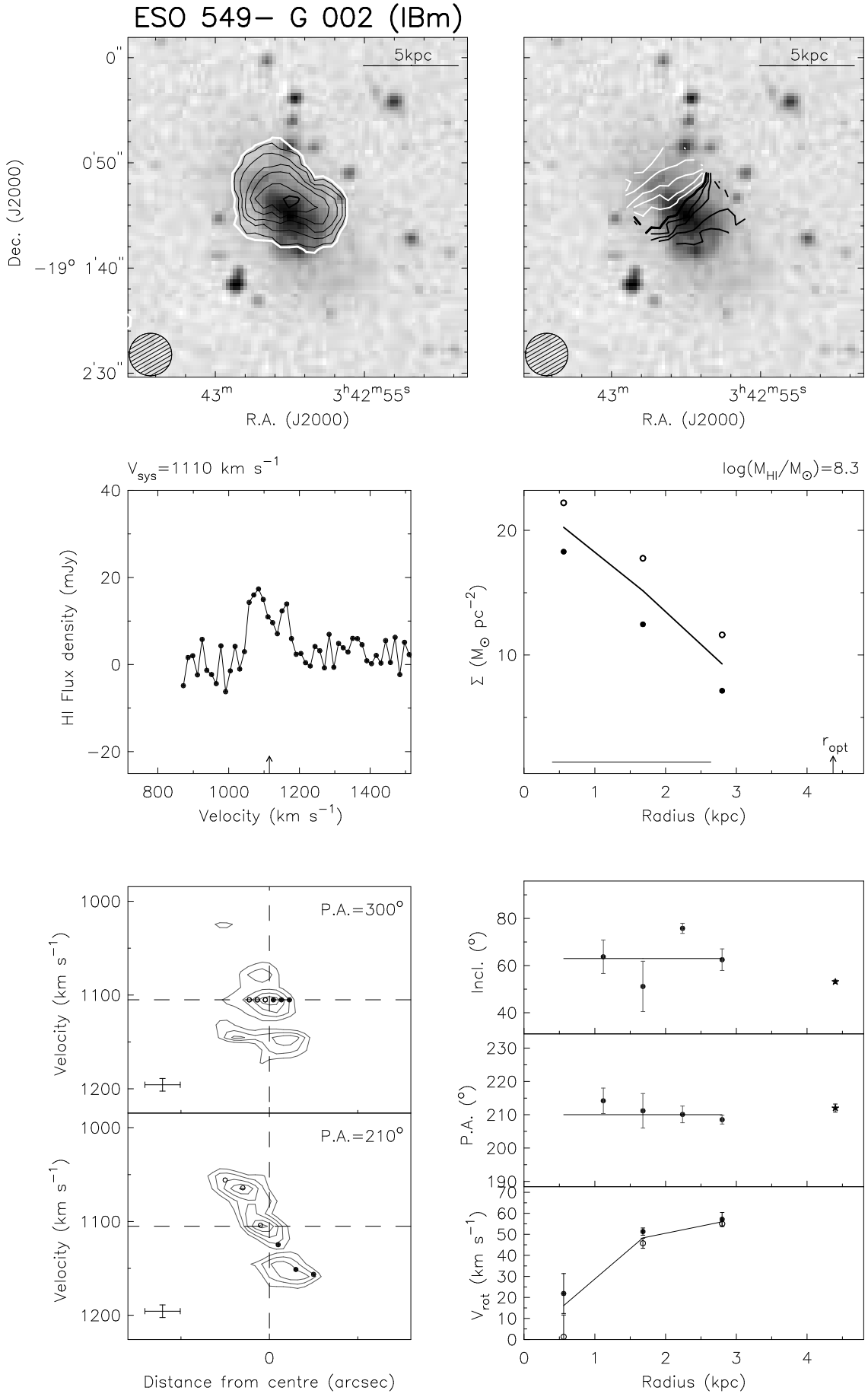
ESO 549− G 002 (IBm)
5kpc
5kpc
Dec. (J2000)
0''
0'50''
−19° 1'40''
2'30''
43m
3h42m55s
R.A. (J2000)
43m
3h42m55s
R.A. (J2000)
Vsys=1110 km s−1
HI Flux density (mJy)
Velocity (km s−1)
log(MHI/M⊙)=8.3
Σ (M⊙ pc−2)
ropt
Radius (kpc)
P.A.=300°
P.A.=210°
Velocity (km s−1)
Distance from centre (arcsec)
Incl. (°)
P.A. (°)
Vrot (km s−1)
Radius (kpc)

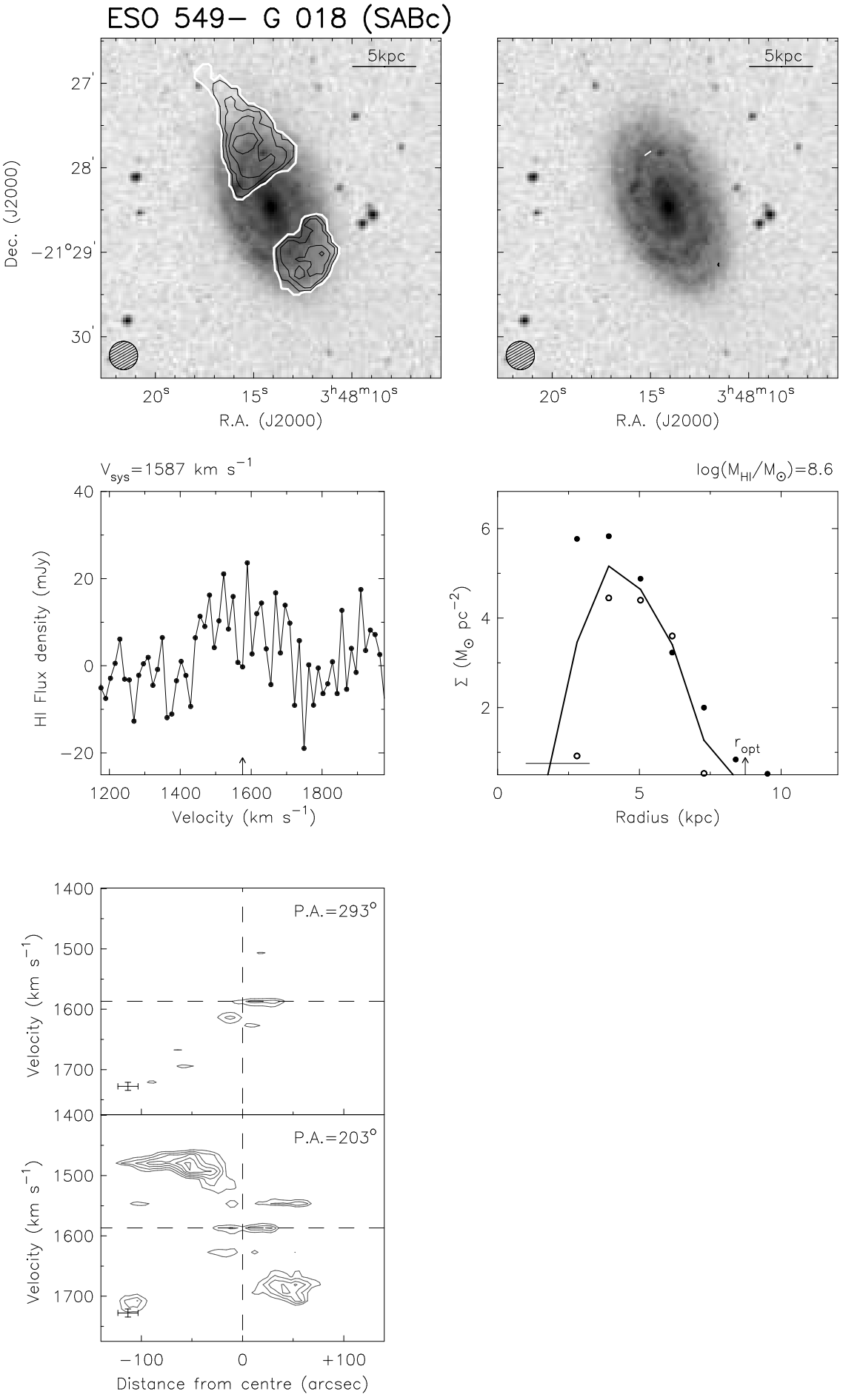
ESO 549− G 018 (SABc)
5kpc
5kpc
Dec. (J2000)
27'
28'
−21°29'
30'
20s
15s
3h48m10s
R.A. (J2000)
20s
15s
3h48m10s
R.A. (J2000)
Vsys=1587 km s−1
HI Flux density (mJy)
40
20
0
−20
1200
1400
1600
1800
Velocity (km s−1)
log(MHI/M⊙)=8.6
Σ (M⊙ pc−2)
6
4
2
ropt
0
5
10
Radius (kpc)
P.A.=293°
P.A.=203°
Velocity (km s−1)
1400
1500
1600
1700
−100
0
+100
Distance from centre (arcsec)

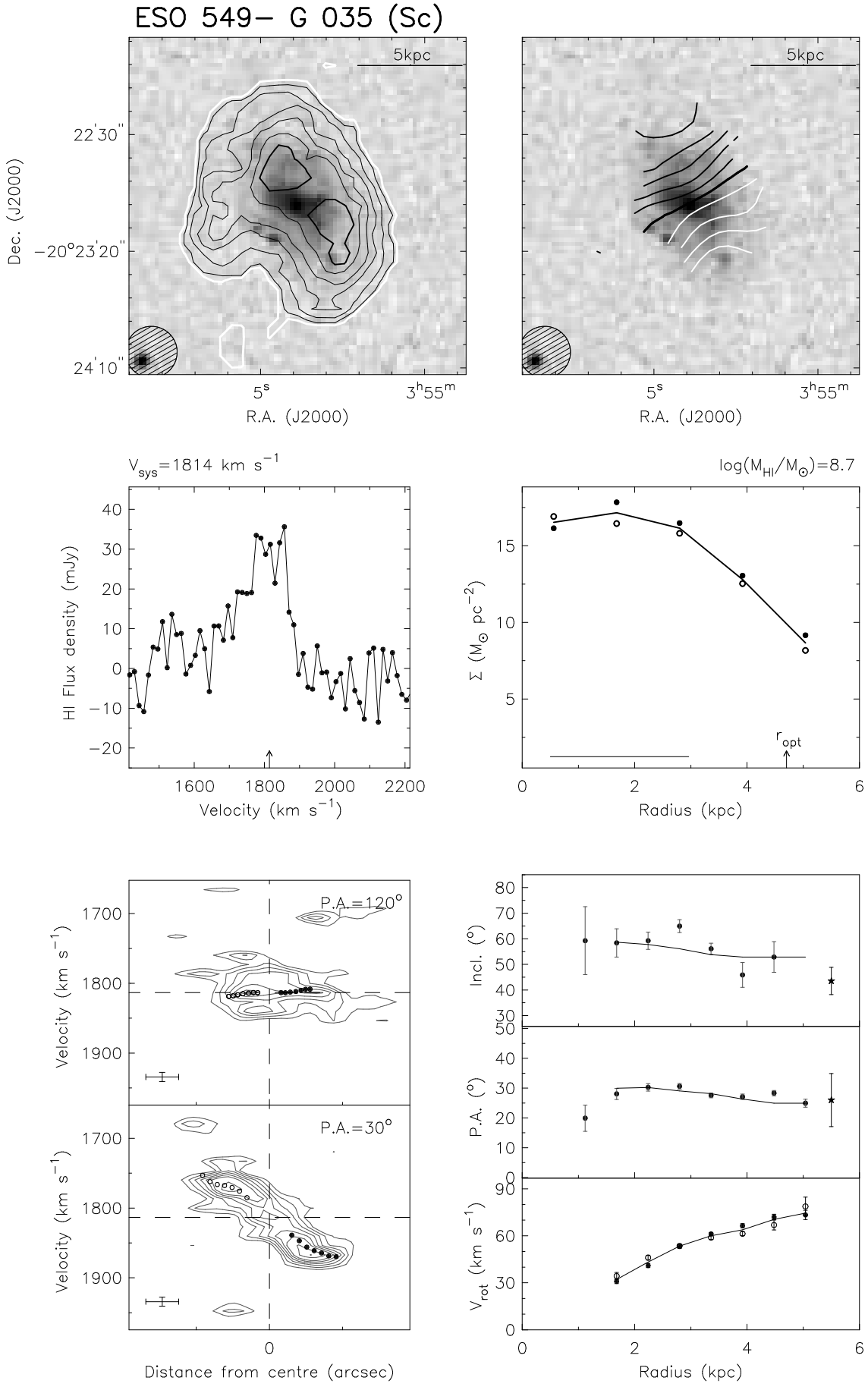
ESO 549– G 035 (Sc)
5kpc
5kpc
Dec. (J2000)
22′30″
−20°23′20″
24′10″
5s
3h55m
R.A. (J2000)
5s
3h55m
R.A. (J2000)
Vsys=1814 km s−1
HI Flux density (mJy)
Velocity (km s−1)
log(MHI/M⊙)=8.7
Σ (M⊙ pc−2)
ropt
Radius (kpc)
P.A.=120°
P.A.=30°
Velocity (km s−1)
Velocity (km s−1)
Distance from centre (arcsec)
Incl. (°)
P.A. (°)
Vrot (km s−1)
Radius (kpc)

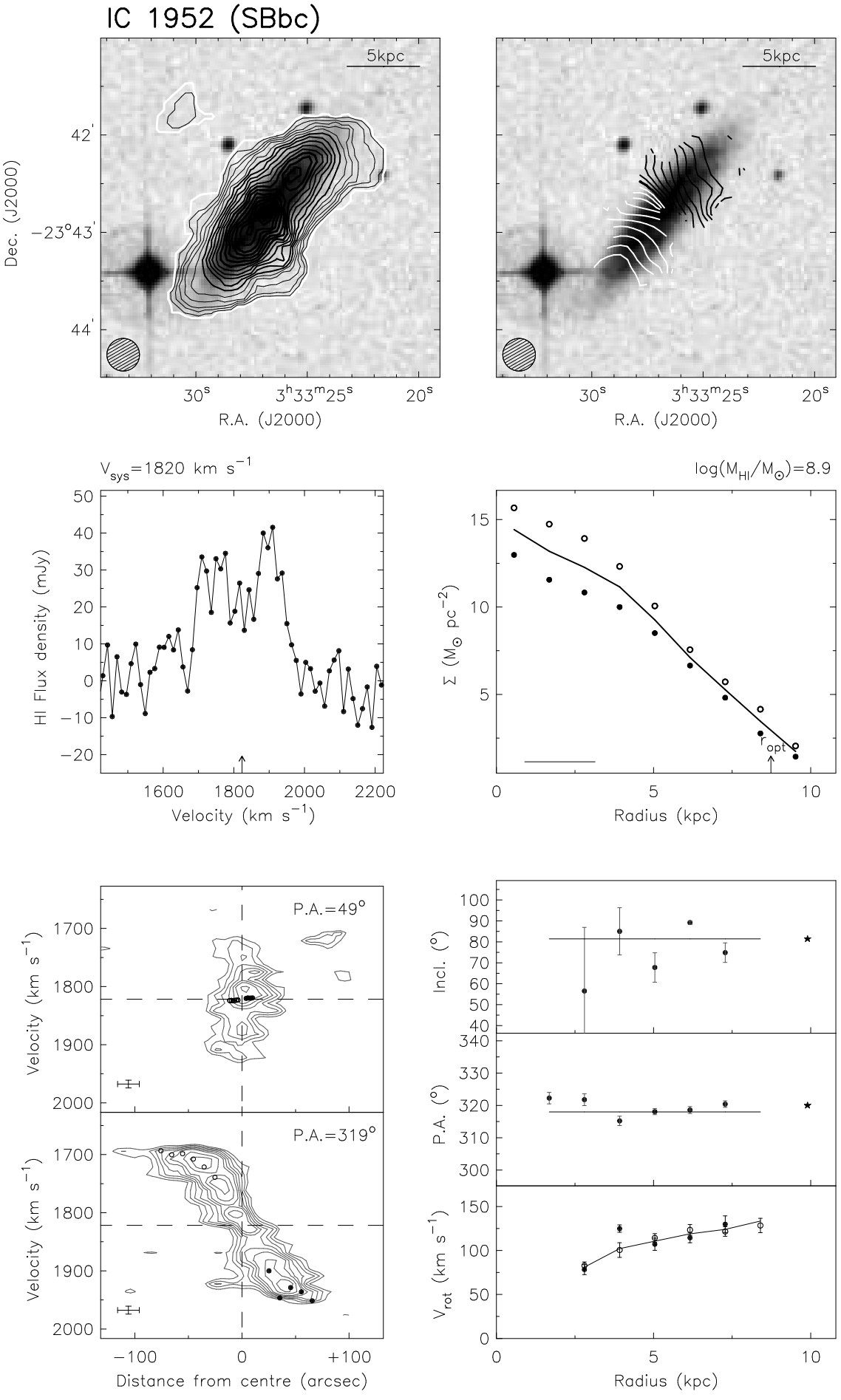
IC 1952 (SBbc)
5kpc
5kpc
Dec. (J2000)
42'
−23°43'
44'
30s
3h33m25s
20s
R.A. (J2000)
30s
3h33m25s
20s
R.A. (J2000)
Vsys=1820 km s−1
log(MHI/M⊙)=8.9
HI Flux density (mJy)
Velocity (km s−1)
Σ (M⊙ pc−2)
Radius (kpc)
ropt
P.A.=49°
P.A.=319°
Velocity (km s−1)
Velocity (km s−1)
Distance from centre (arcsec)
Incl. (°)
P.A. (°)
Vrot (km s−1)
Radius (kpc)

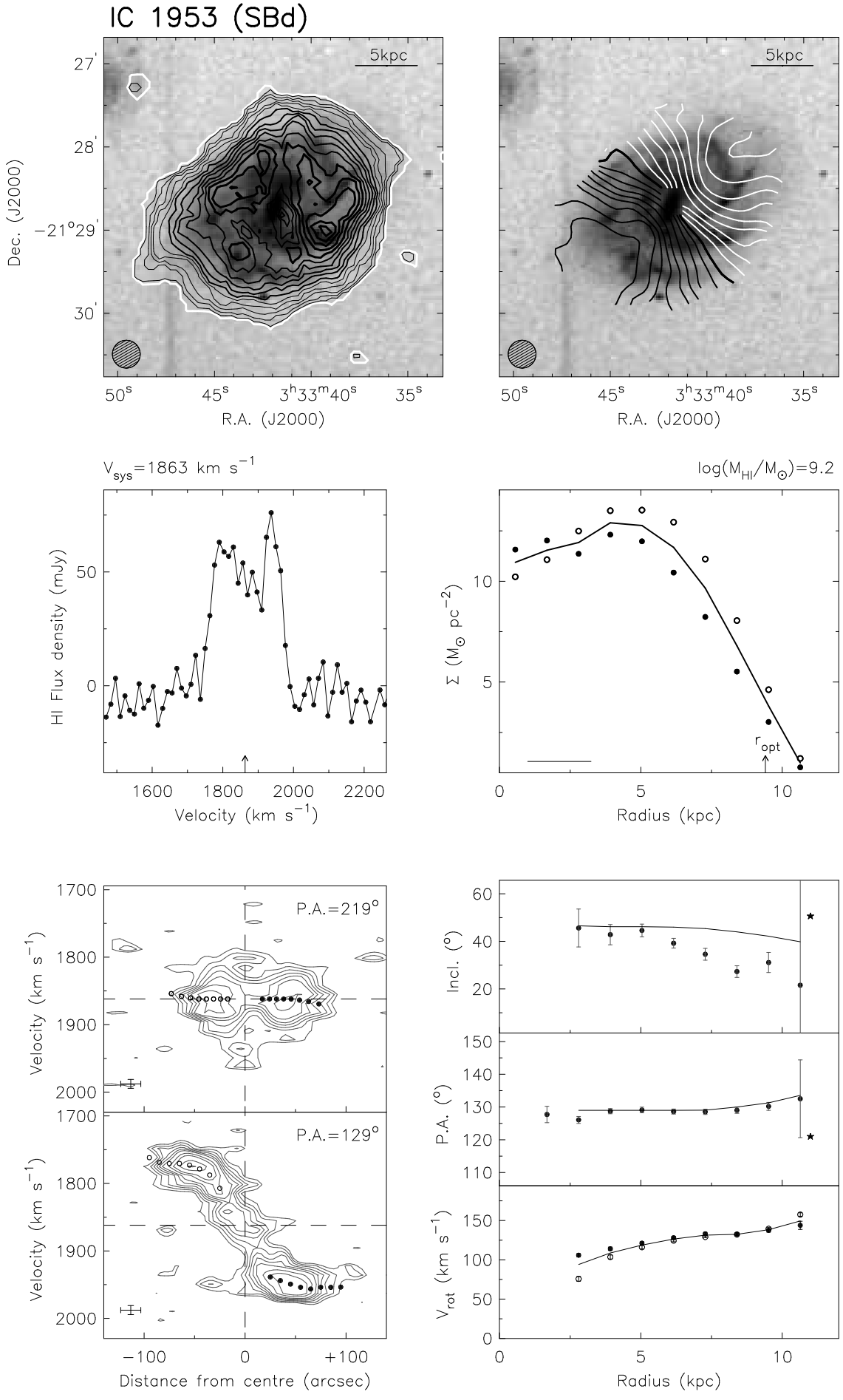
IC 1953 (SBd)
5kpc
Dec. (J2000)
R.A. (J2000)
V_sys=1863 km s^-1
HI Flux density (mJy)
Velocity (km s^-1)
log(M_HI/M_⊙)=9.2
Σ (M_⊙ pc^-2)
r_opt
Radius (kpc)
P.A.=219°
P.A.=129°
Velocity (km s^-1)
Distance from centre (arcsec)
Incl. (°)
P.A. (°)
V_rot (km s^-1)

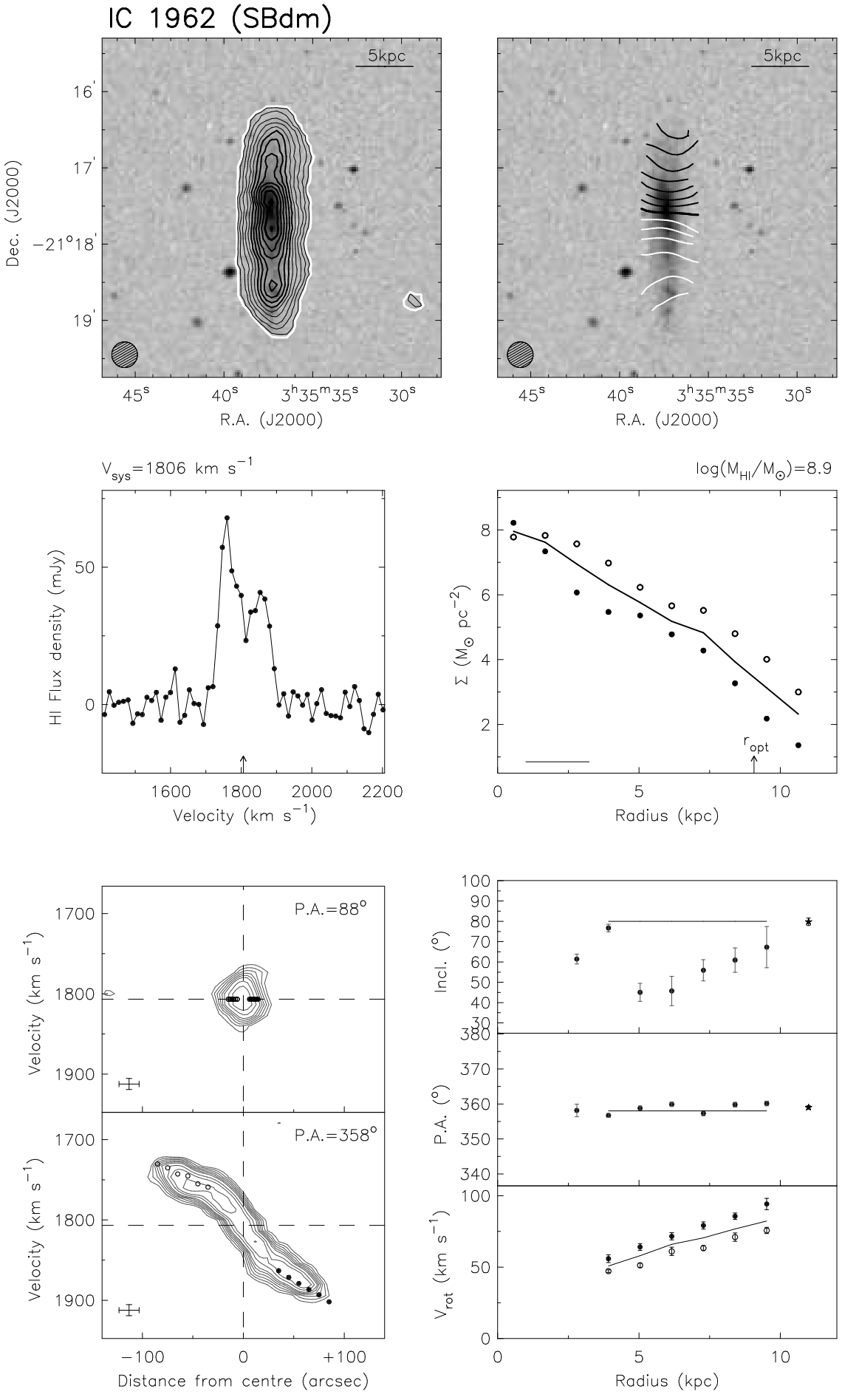
IC 1962 (SBdm)
5kpc
5kpc
Dec. (J2000)
16'
17'
−21°18'
19'
45s
40s
3h35m35s
30s
R.A. (J2000)
45s
40s
3h35m35s
30s
R.A. (J2000)
Vsys=1806 km s−1
log(MHI/M⊙)=8.9
HI Flux density (mJy)
50
0
1600
1800
2000
2200
Velocity (km s−1)
Σ (M⊙ pc−2)
8
6
4
2
ropt
0
5
10
Radius (kpc)
P.A.=88°
P.A.=358°
Velocity (km s−1)
1700
1800
1900
−100
0
+100
Distance from centre (arcsec)
Incl. (°)
100
90
80
70
60
50
40
30
P.A. (°)
380
370
360
350
340
Vrot (km s−1)
100
50
0
0
5
10
Radius (kpc)

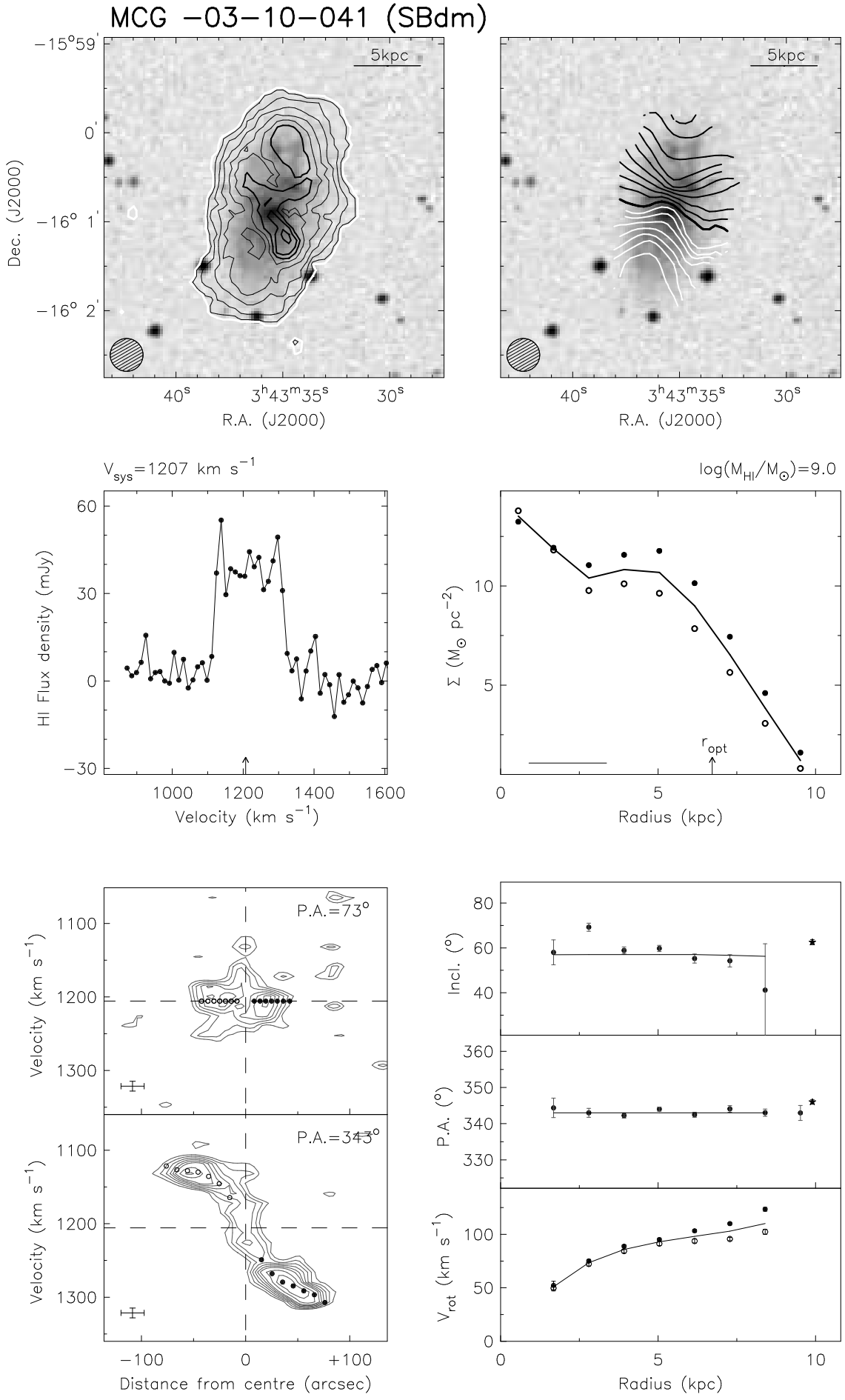
MCG −03−10−041 (SBdm)
5kpc
Dec. (J2000)
R.A. (J2000)
V_{sys}=1207 km s^{-1}
HI Flux density (mJy)
Velocity (km s^{-1})
log($M_{HI}/M_\odot$)=9.0
Σ ($M_\odot$ pc^{-2})
r_{opt}
Radius (kpc)
P.A.=73°
P.A.=343°
Velocity (km s^{-1})
Distance from centre (arcsec)
Incl. (°)
P.A. (°)
V_{rot} (km s^{-1})

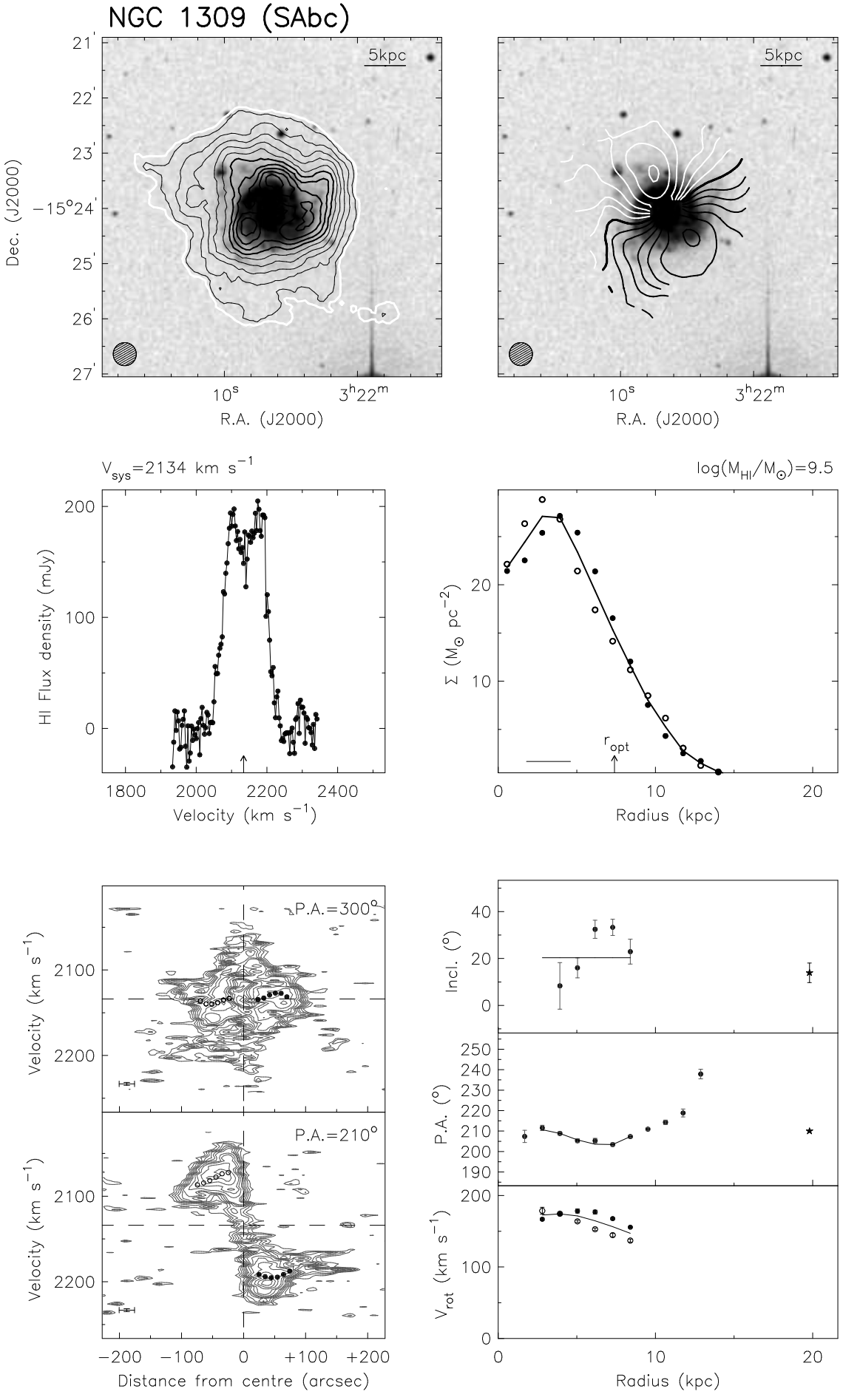
NGC 1309 (SAbc)
5kpc
5kpc
Dec. (J2000)
R.A. (J2000)
R.A. (J2000)
V_sys=2134 km s^-1
log(M_HI/M_⊙)=9.5
HI Flux density (mJy)
Velocity (km s^-1)
Σ (M_⊙ pc^-2)
r_opt
Radius (kpc)
P.A.=300°
P.A.=210°
Velocity (km s^-1)
Distance from centre (arcsec)
Incl. (°)
P.A. (°)
V_rot (km s^-1)
Radius (kpc)

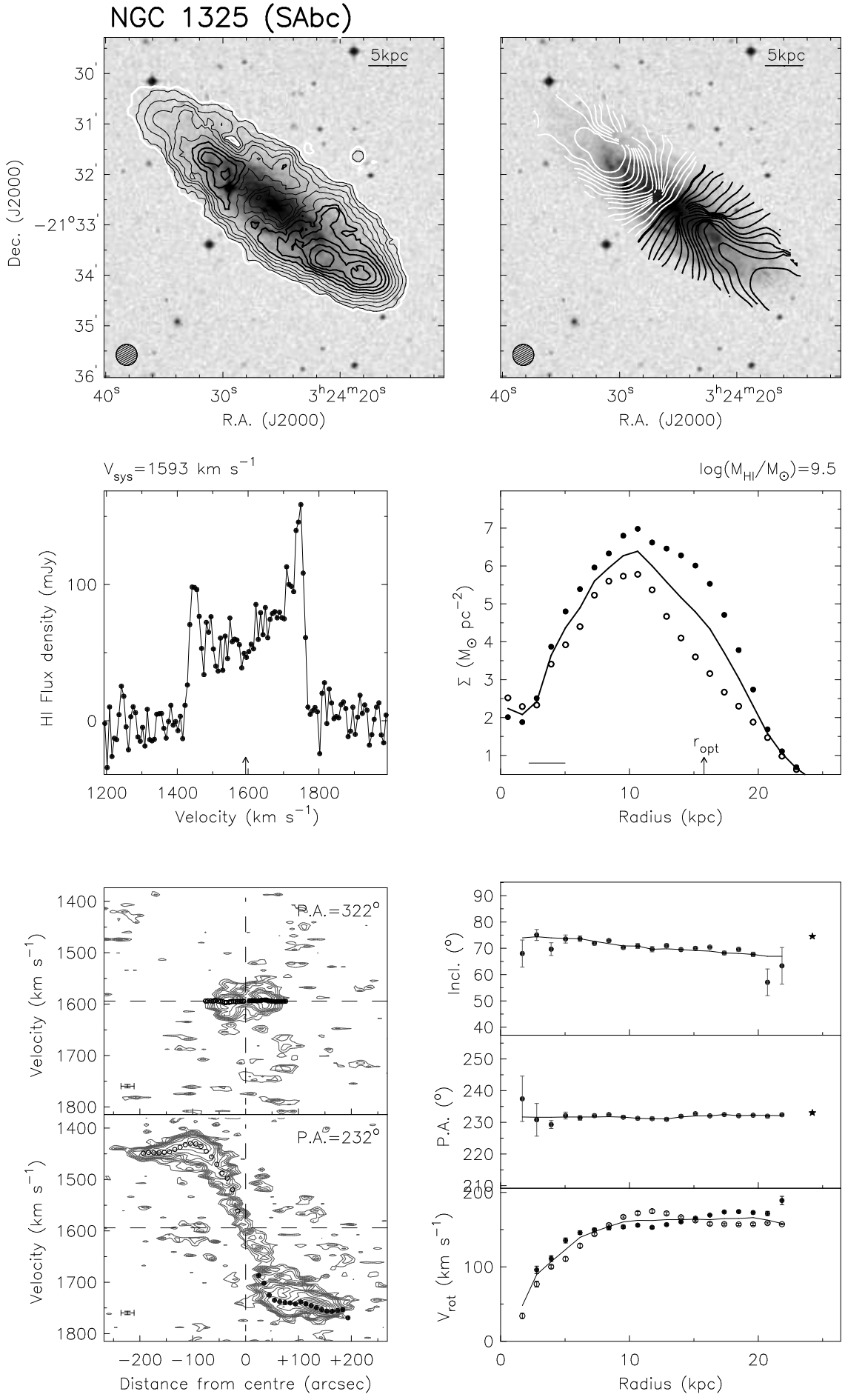
NGC 1325 (SAbc)
5kpc
Dec. (J2000)
R.A. (J2000)
V_sys=1593 km s^-1
log(M_HI/M_⊙)=9.5
HI Flux density (mJy)
Velocity (km s^-1)
Σ (M_⊙ pc^-2)
r_opt
Radius (kpc)
P.A.=322°
P.A.=232°
Distance from centre (arcsec)
Incl. (°)
P.A. (°)
V_rot (km s^-1)

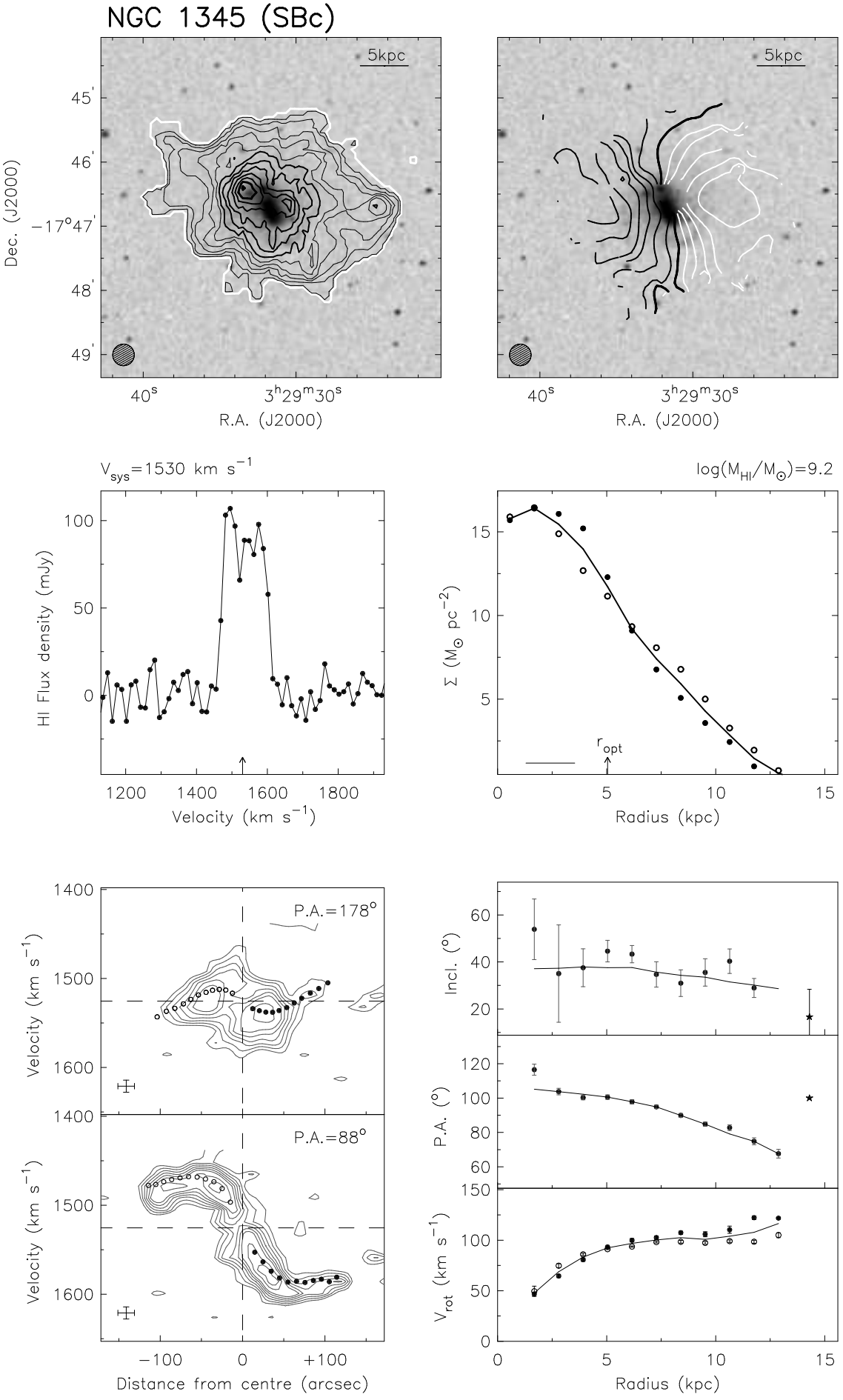
NGC 1345 (SBc)
5kpc
Dec. (J2000)
45'
46'
−17°47'
48'
49'
40s
3h29m30s
R.A. (J2000)
5kpc
40s
3h29m30s
R.A. (J2000)
Vsys=1530 km s−1
HI Flux density (mJy)
100
50
0
1200
1400
1600
1800
Velocity (km s−1)
log(MHI/M⊙)=9.2
Σ (M⊙ pc−2)
15
10
5
ropt
0
5
10
15
Radius (kpc)
Velocity (km s−1)
1400
1500
1600
P.A.=178°
P.A.=88°
−100
0
+100
Distance from centre (arcsec)
Incl. (°)
60
40
20
P.A. (°)
120
100
80
60
Vrot (km s−1)
150
100
50
0
0
5
10
15
Radius (kpc)

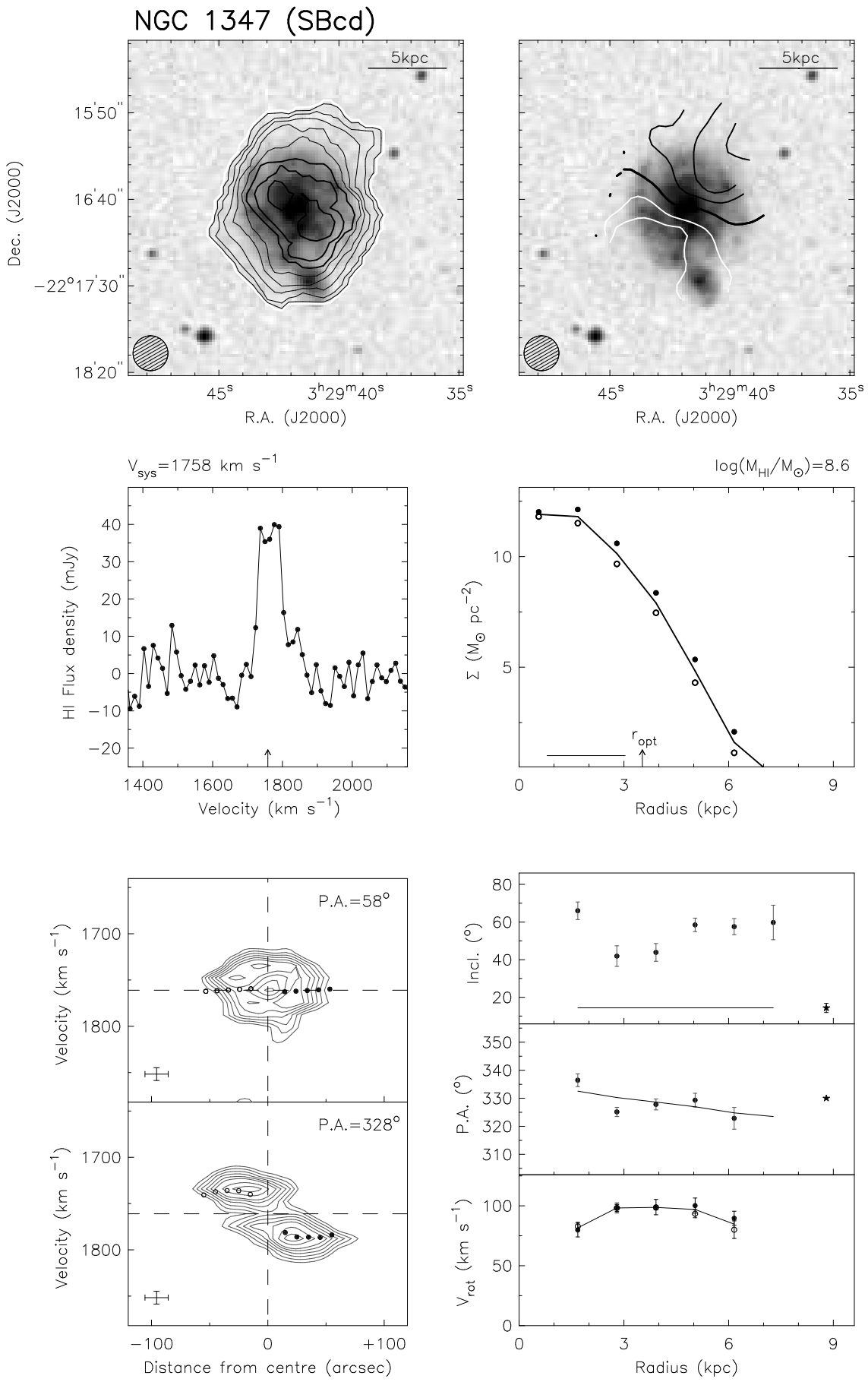
NGC 1347 (SBcd)
5kpc
5kpc
15'50"
16'40"
−22°17'30"
18'20"
Dec. (J2000)
45s
3h29m40s
35s
R.A. (J2000)
45s
3h29m40s
35s
R.A. (J2000)
Vsys=1758 km s−1
log(MHI/M⊙)=8.6
HI Flux density (mJy)
Velocity (km s−1)
Σ (M⊙ pc−2)
ropt
Radius (kpc)
P.A.=58°
P.A.=328°
Velocity (km s−1)
Velocity (km s−1)
Distance from centre (arcsec)
Incl. (°)
P.A. (°)
Vrot (km s−1)
Radius (kpc)

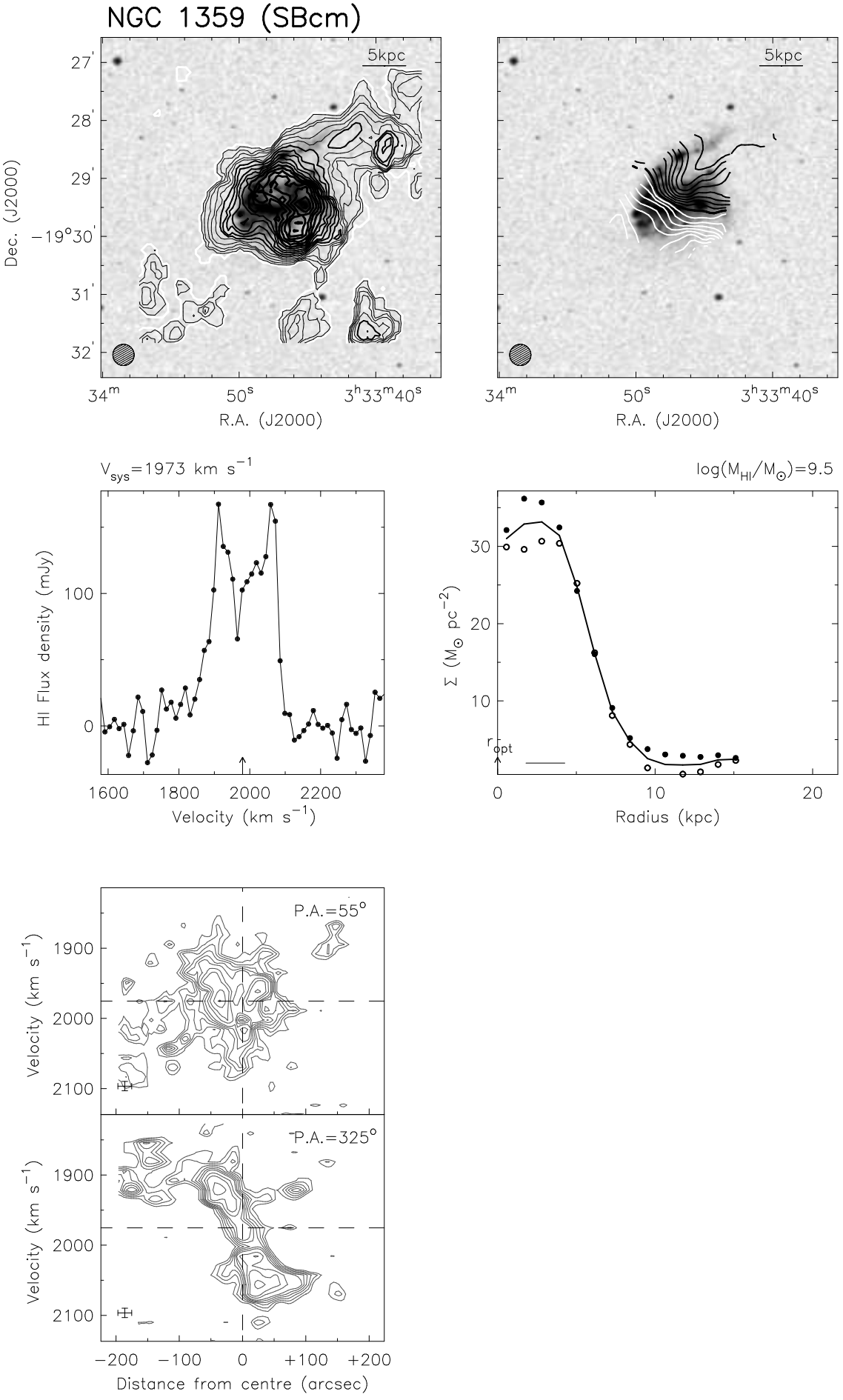
NGC 1359 (SBcm)
5kpc
Dec. (J2000)
R.A. (J2000)
V_{sys}=1973 km s^{-1}
HI Flux density (mJy)
Velocity (km s^{-1})
log($M_{HI}/M_\odot$)=9.5
Σ ($M_\odot$ pc^{-2})
r_{opt}
Radius (kpc)
P.A.=55°
P.A.=325°
Velocity (km s^{-1})
Distance from centre (arcsec)

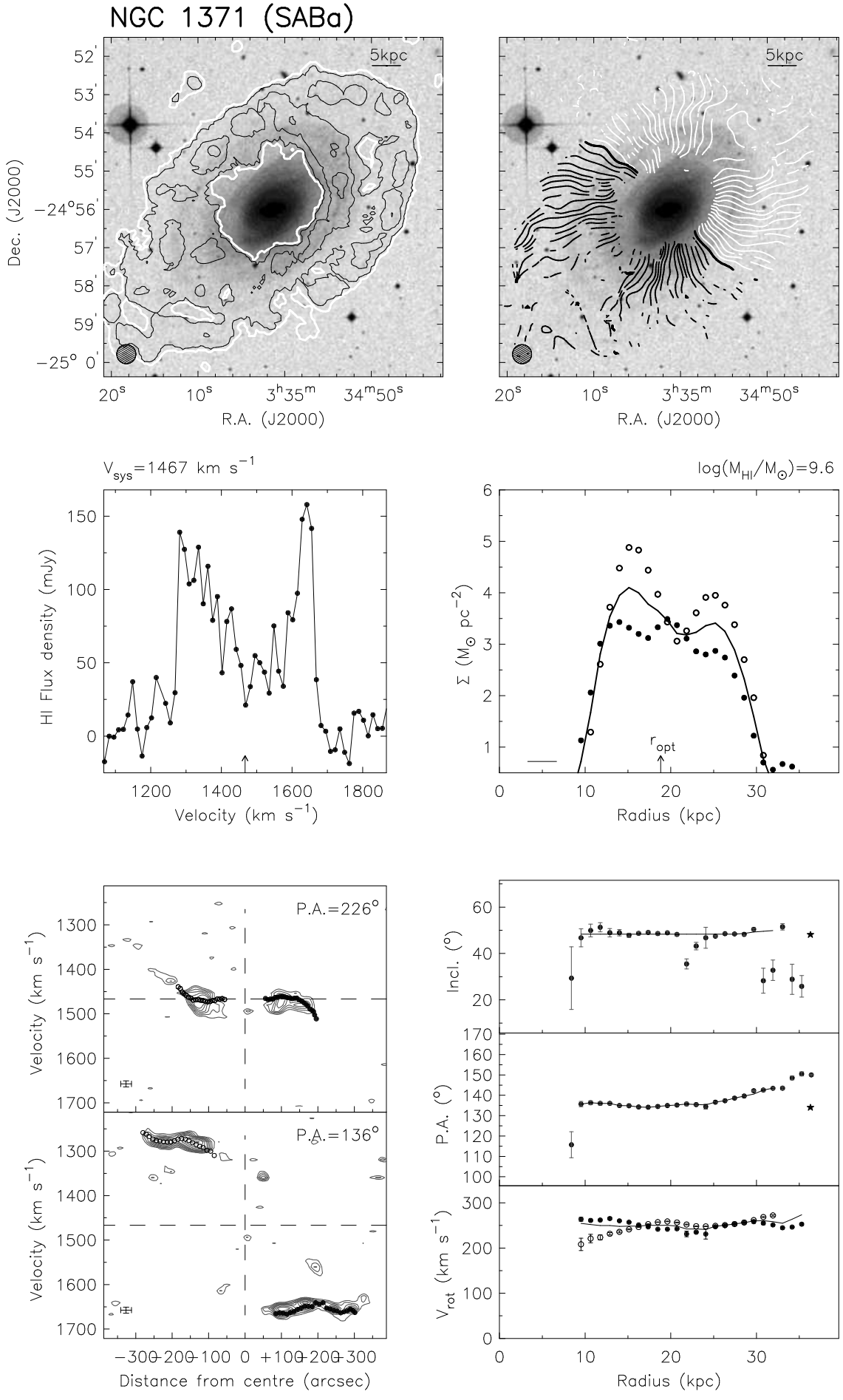
NGC 1371 (SABa)
5kpc
Dec. (J2000)
R.A. (J2000)
V_sys=1467 km s^-1
HI Flux density (mJy)
Velocity (km s^-1)
log(M_HI/M_⊙)=9.6
Σ (M_⊙ pc^-2)
r_opt
Radius (kpc)
P.A.=226°
P.A.=136°
Velocity (km s^-1)
Distance from centre (arcsec)
Incl. (°)
P.A. (°)
V_rot (km s^-1)

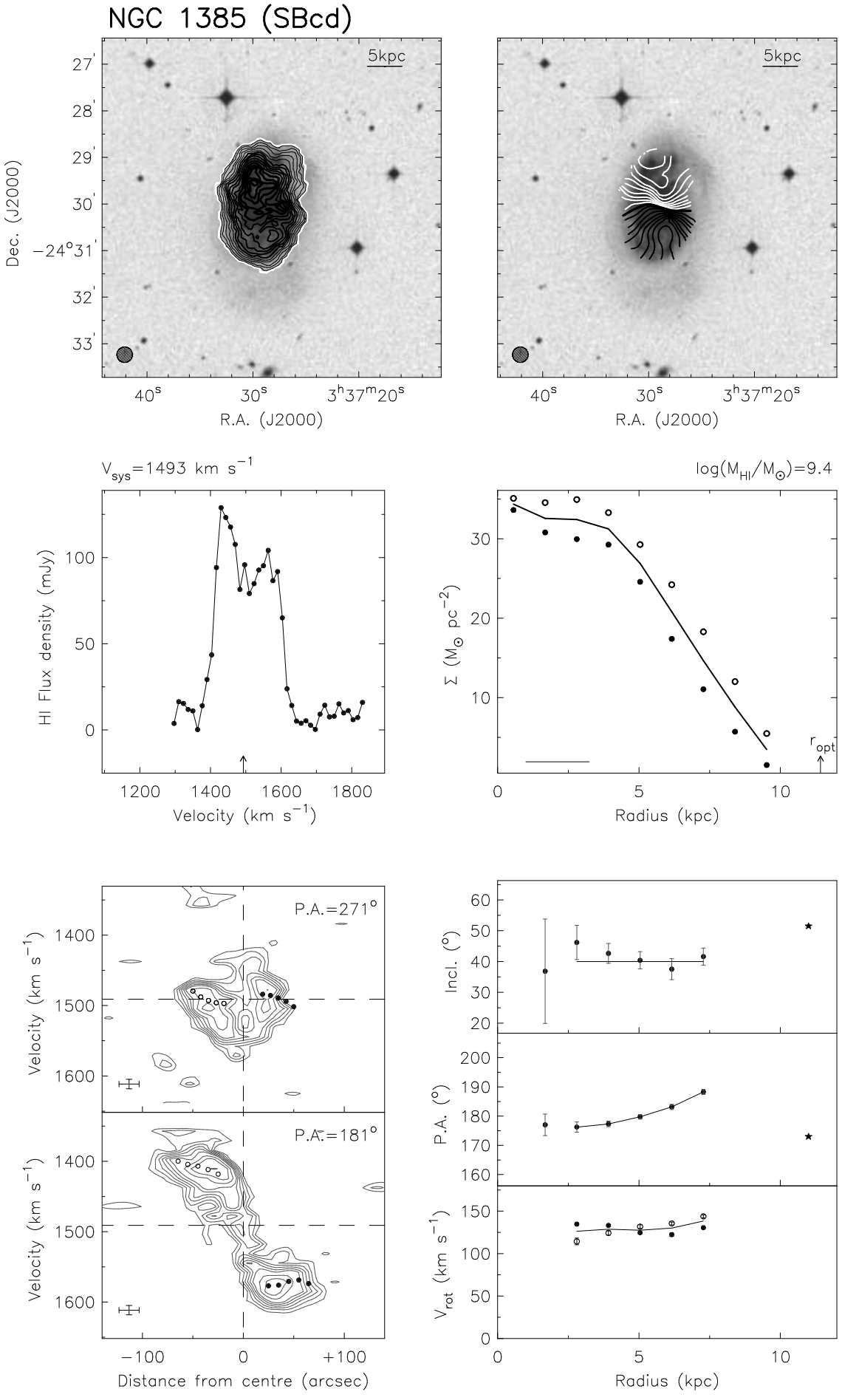
NGC 1385 (SBcd)
5kpc
5kpc
Dec. (J2000)
R.A. (J2000)
R.A. (J2000)
V_sys=1493 km s^-1
log(M_HI/M_⊙)=9.4
HI Flux density (mJy)
Velocity (km s^-1)
Σ (M_⊙ pc^-2)
r_opt
Radius (kpc)
P.A.=271°
P.A.=181°
Velocity (km s^-1)
Velocity (km s^-1)
Distance from centre (arcsec)
Incl. (°)
P.A. (°)
V_rot (km s^-1)
Radius (kpc)

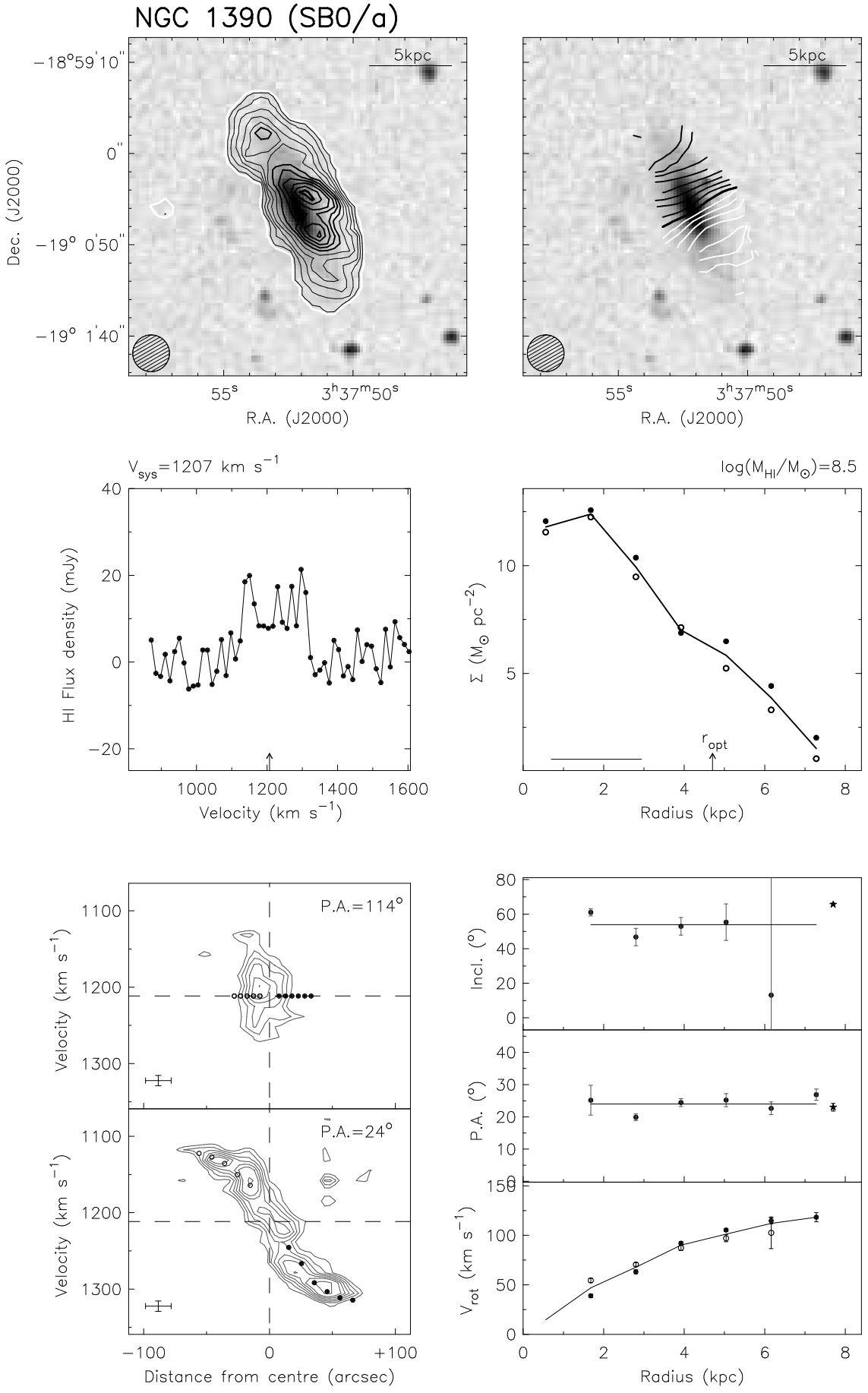
NGC 1390 (SB0/a)
5kpc
5kpc
−18°59'10"
0"
−19° 0'50"
−19° 1'40"
Dec. (J2000)
55s
3h37m50s
R.A. (J2000)
55s
3h37m50s
R.A. (J2000)
Vsys=1207 km s−1
log(MHI/M⊙)=8.5
HI Flux density (mJy)
Velocity (km s−1)
Σ (M⊙ pc−2)
ropt
Radius (kpc)
P.A.=114°
P.A.=24°
Velocity (km s−1)
Velocity (km s−1)
Distance from centre (arcsec)
Incl. (°)
P.A. (°)
Vrot (km s−1)
Radius (kpc)

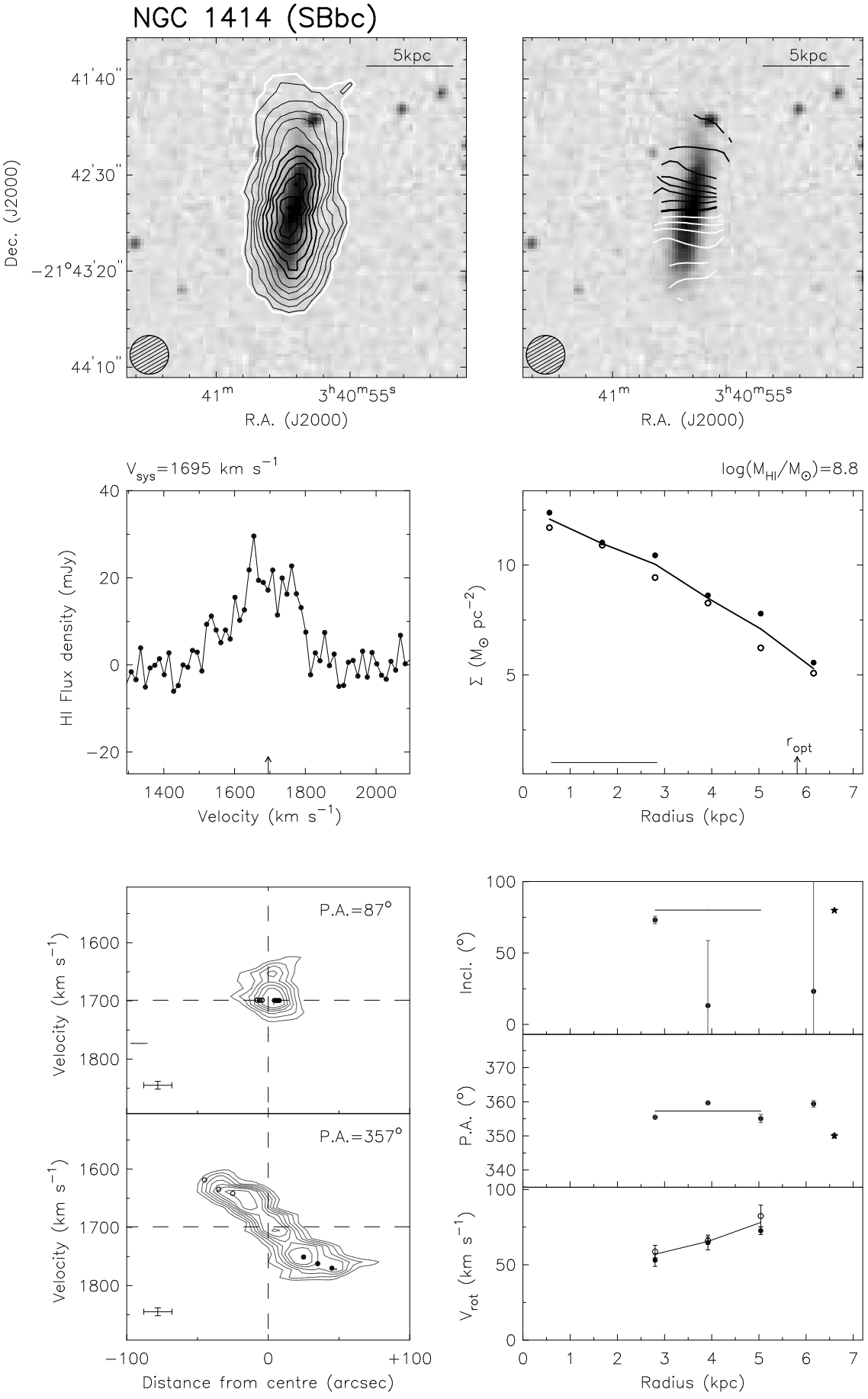
NGC 1414 (SBbc)
5kpc
5kpc
Dec. (J2000)
41'40"
42'30"
−21°43'20"
44'10"
41m
3h40m55s
R.A. (J2000)
41m
3h40m55s
R.A. (J2000)
Vsys=1695 km s−1
HI Flux density (mJy)
40
20
0
−20
1400
1600
1800
2000
Velocity (km s−1)
log(MHI/M⊙)=8.8
Σ (M⊙ pc−2)
10
5
ropt
0
1
2
3
4
5
6
7
Radius (kpc)
P.A.=87°
P.A.=357°
Velocity (km s−1)
1600
1700
1800
−100
0
+100
Distance from centre (arcsec)
Incl. (°)
100
50
0
P.A. (°)
370
360
350
340
Vrot (km s−1)
100
50
0
0
1
2
3
4
5
6
7
Radius (kpc)

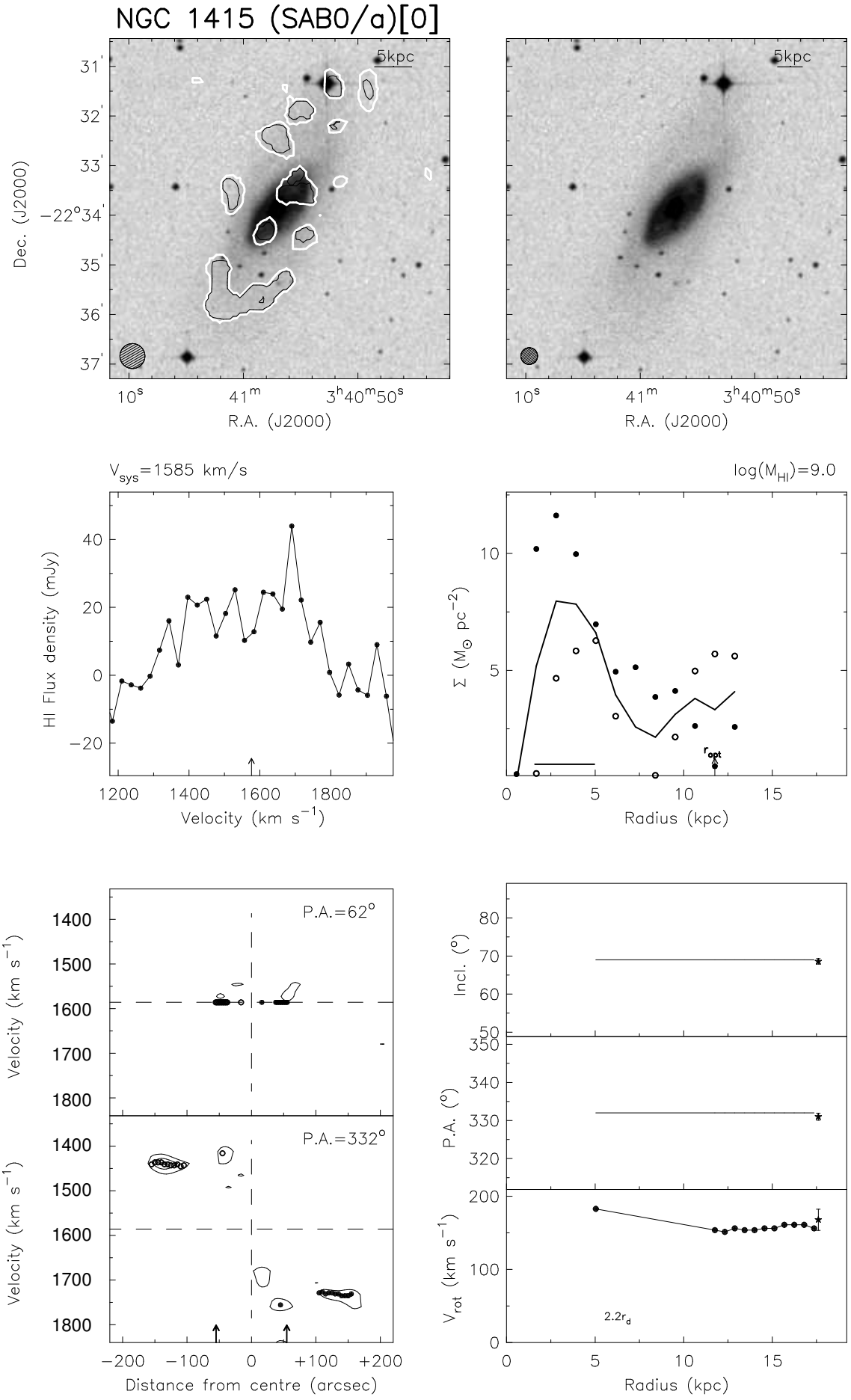
NGC 1415 (SAB0/a)[0]
5kpc
5kpc
Dec. (J2000)
R.A. (J2000)
R.A. (J2000)
V_sys=1585 km/s
log(M_HI)=9.0
HI Flux density (mJy)
Velocity (km s^-1)
Σ (M_⊙ pc^-2)
r_opt
Radius (kpc)
P.A.=62°
P.A.=332°
Velocity (km s^-1)
Velocity (km s^-1)
Distance from centre (arcsec)
Incl. (°)
P.A. (°)
V_rot (km s^-1)
2.2r_d
Radius (kpc)

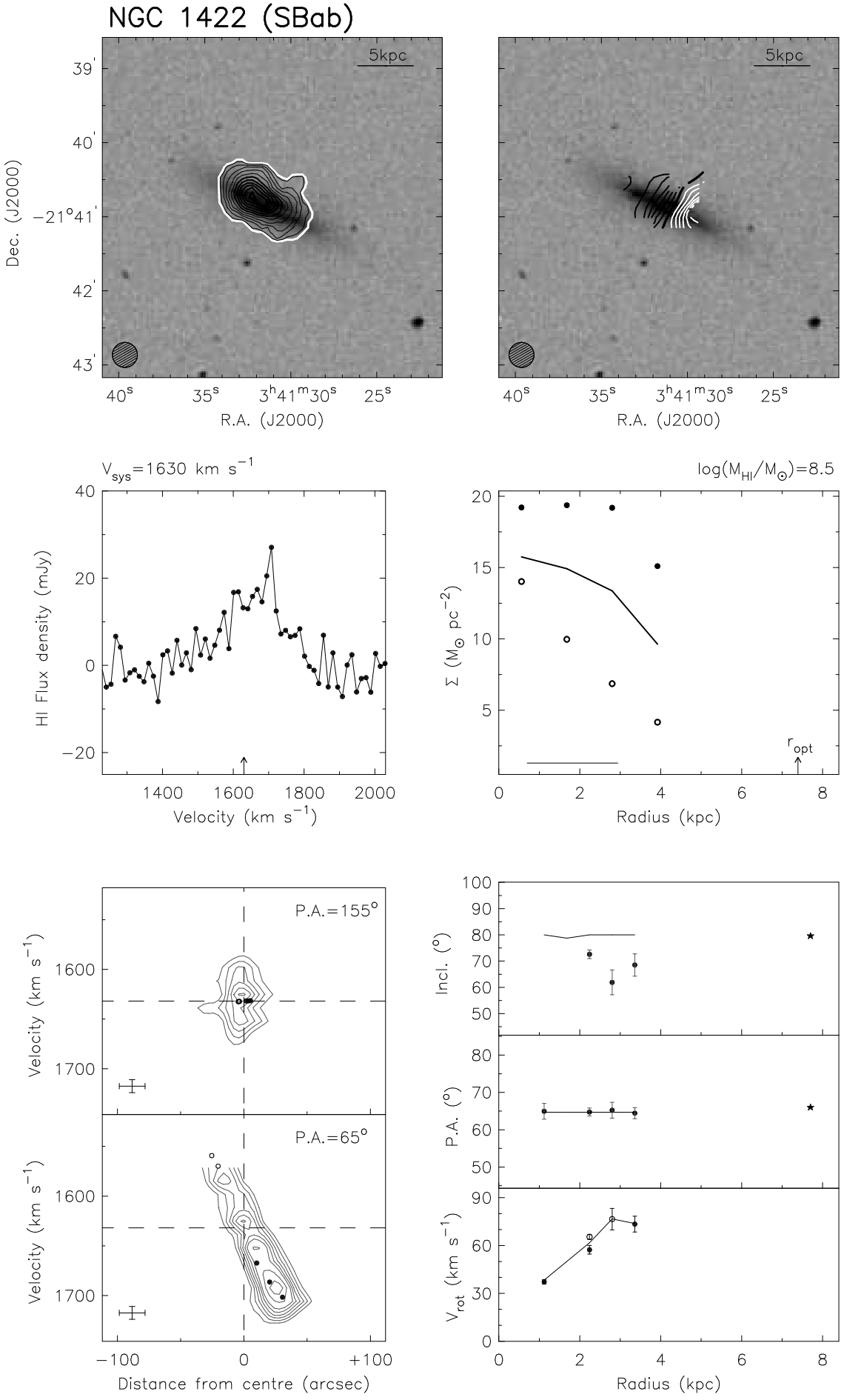
NGC 1422 (SBab)
5kpc
5kpc
Dec. (J2000)
R.A. (J2000)
R.A. (J2000)
V_{sys}=1630 km s^{-1}
log($M_{HI}/M_\odot$)=8.5
HI Flux density (mJy)
Velocity (km s^{-1})
Σ ($M_\odot$ pc^{-2})
r_{opt}
Radius (kpc)
P.A.=155°
P.A.=65°
Velocity (km s^{-1})
Velocity (km s^{-1})
Distance from centre (arcsec)
Incl. (°)
P.A. (°)
V_{rot} (km s^{-1})
Radius (kpc)

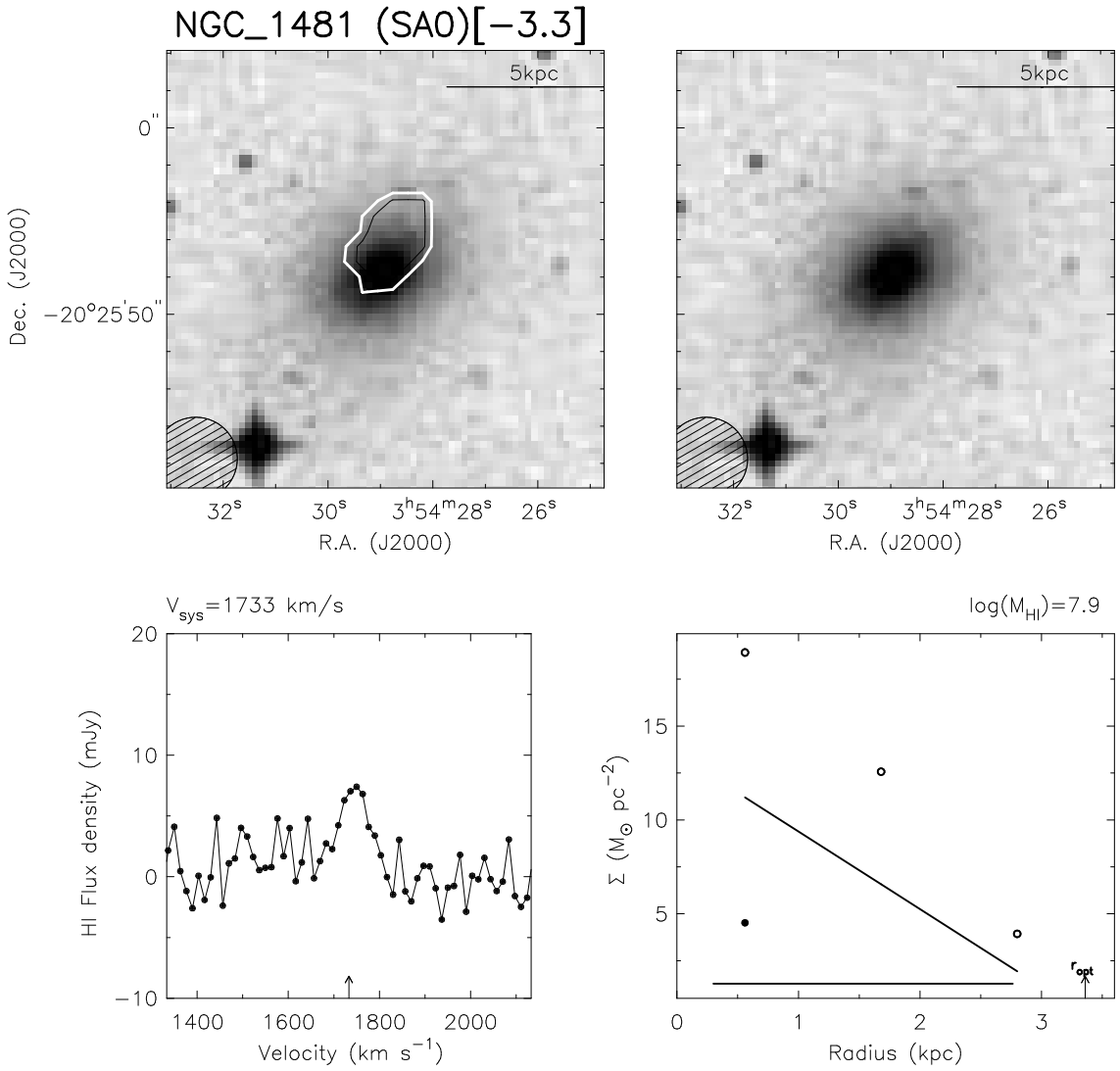
NGC_1481 (SA0)[−3.3]
5kpc
0″
−20°25′50″
Dec. (J2000)
32s 30s 3h54m28s 26s
R.A. (J2000)
5kpc
32s 30s 3h54m28s 26s
R.A. (J2000)
Vsys=1733 km/s
HI Flux density (mJy)
20
10
0
−10
1400 1600 1800 2000
Velocity (km s−1)
log(MHI)=7.9
Σ (M⊙ pc−2)
15
10
5
0 1 2 3
Radius (kpc)
ropt

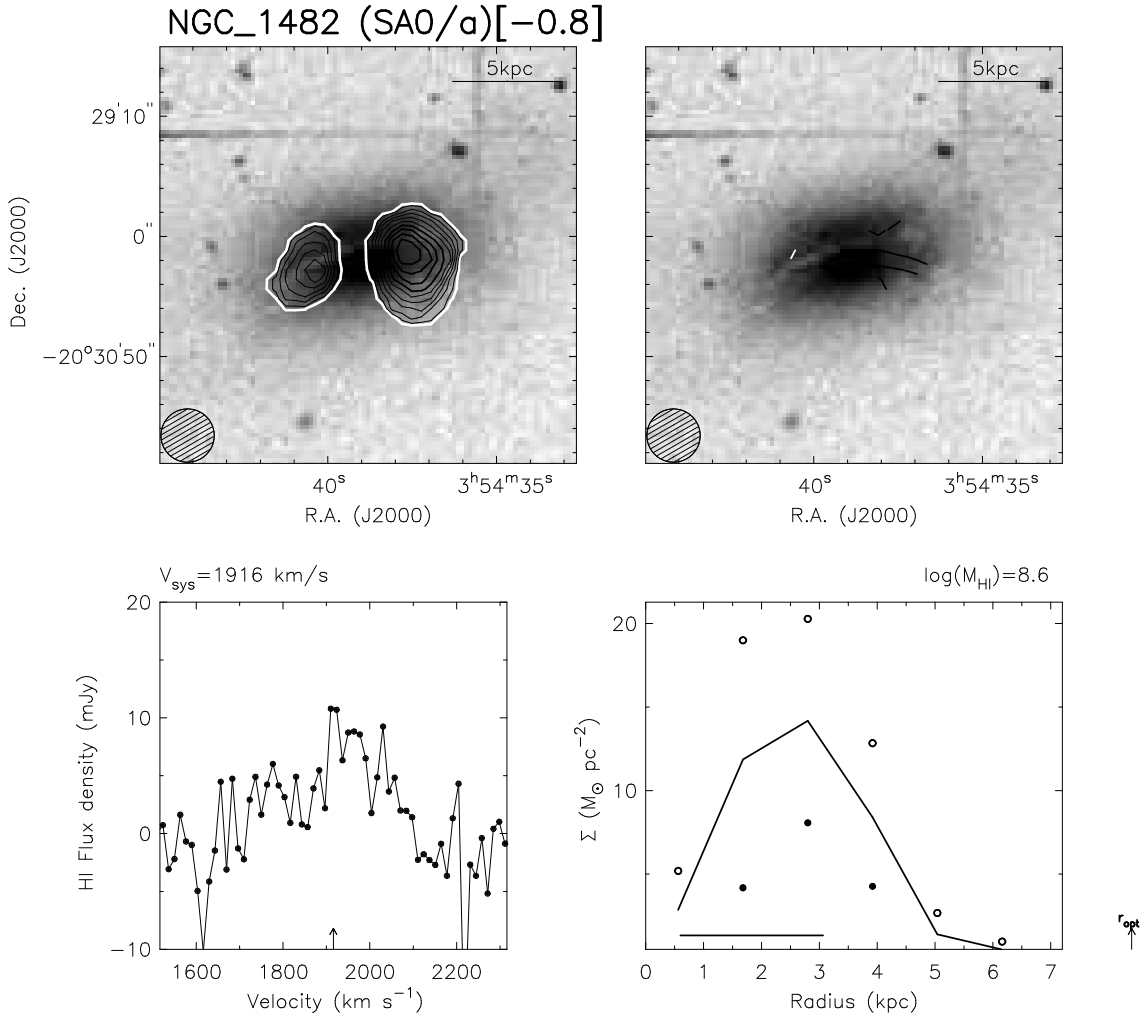
NGC_1482 (SA0/a)[−0.8]
5kpc
5kpc
29'10"
0"
−20°30'50"
Dec. (J2000)
40s
3h54m35s
R.A. (J2000)
40s
3h54m35s
R.A. (J2000)
Vsys=1916 km/s
log(MHI)=8.6
HI Flux density (mJy)
Velocity (km s−1)
Σ (M⊙ pc−2)
Radius (kpc)
ropt

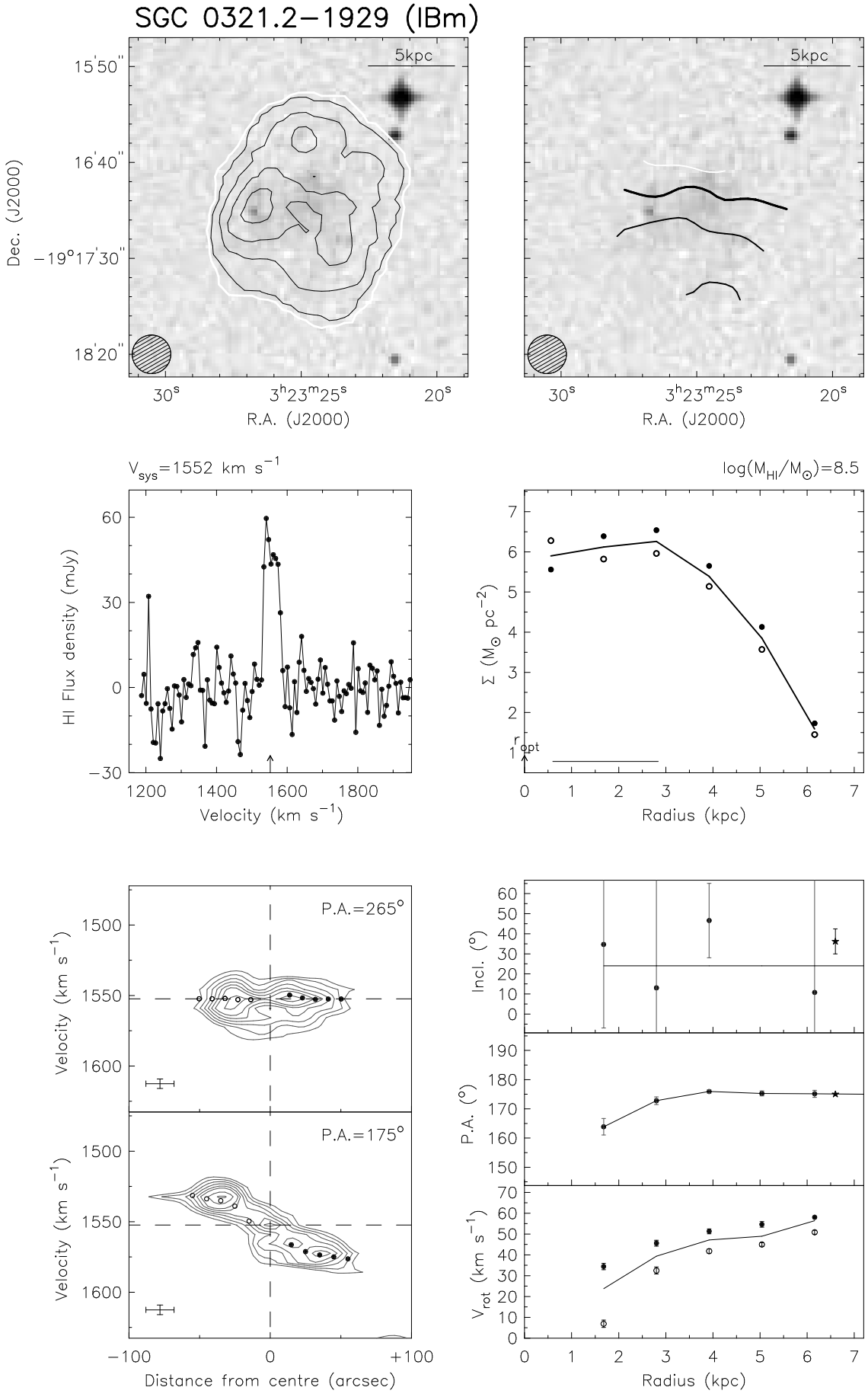
SGC 0321.2−1929 (IBm)
5kpc
5kpc
Dec. (J2000)
15'50"
16'40"
−19°17'30"
18'20"
30s
3h23m25s
20s
R.A. (J2000)
R.A. (J2000)
Vsys=1552 km s−1
log(MHI/M⊙)=8.5
HI Flux density (mJy)
60
30
0
−30
1200
1400
1600
1800
Velocity (km s−1)
Σ (M⊙ pc−2)
7
6
5
4
3
2
1
ropt
0
1
2
3
4
5
6
7
Radius (kpc)
P.A.=265°
P.A.=175°
Velocity (km s−1)
1500
1550
1600
−100
0
+100
Distance from centre (arcsec)
Incl. (°)
60
50
40
30
20
10
0
P.A. (°)
190
180
170
160
150
Vrot (km s−1)
70
60
50
40
30
20
10
0
Radius (kpc)

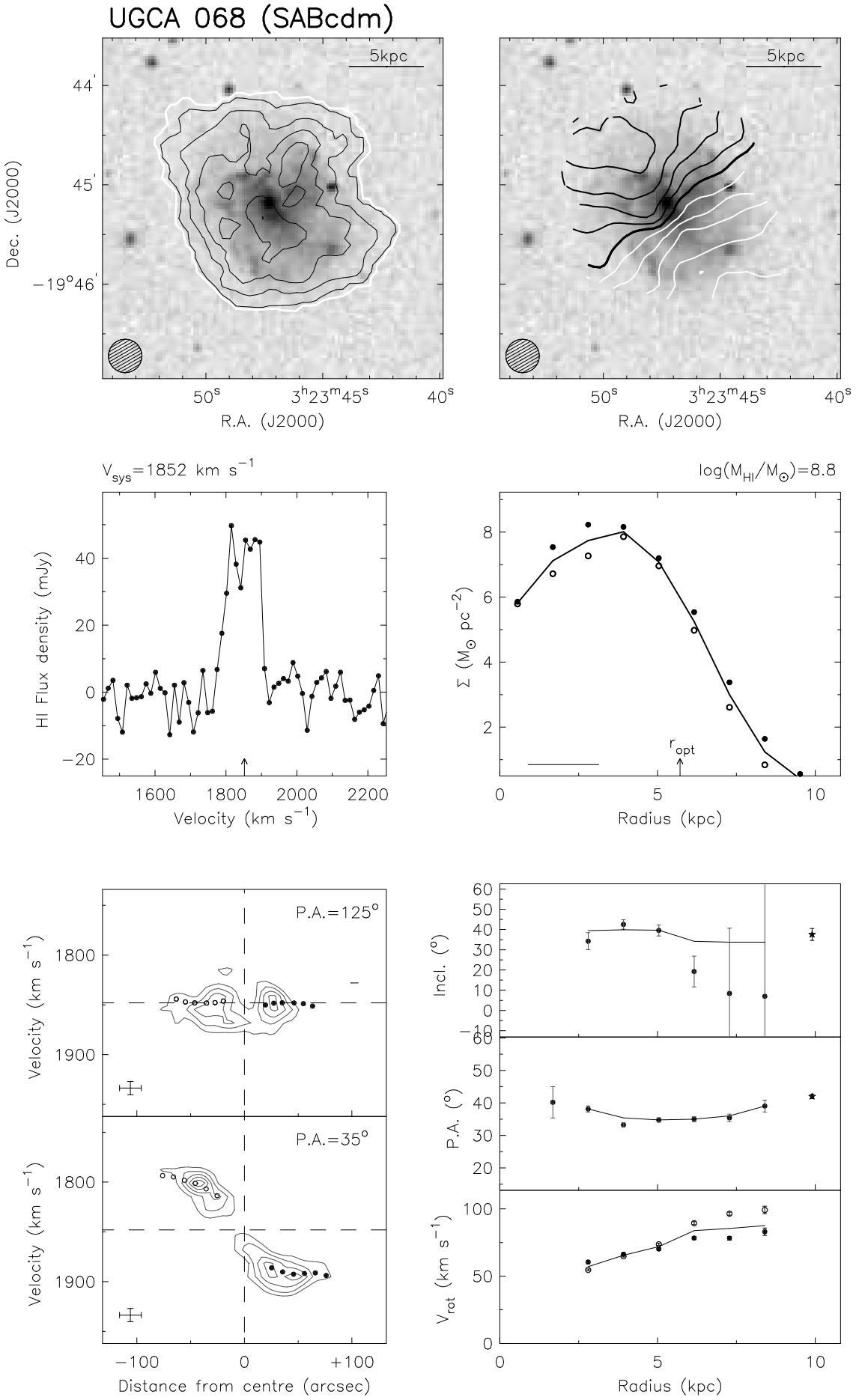
UGCA 068 (SABcdm)
5kpc
5kpc
Dec. (J2000)
44'
45'
−19°46'
50s
3h23m45s
40s
R.A. (J2000)
R.A. (J2000)
Vsys=1852 km s−1
log(MHI/M⊙)=8.8
HI Flux density (mJy)
Velocity (km s−1)
Σ (M⊙ pc−2)
ropt
Radius (kpc)
P.A.=125°
P.A.=35°
Velocity (km s−1)
Distance from centre (arcsec)
Incl. (°)
P.A. (°)
Vrot (km s−1)
Radius (kpc)

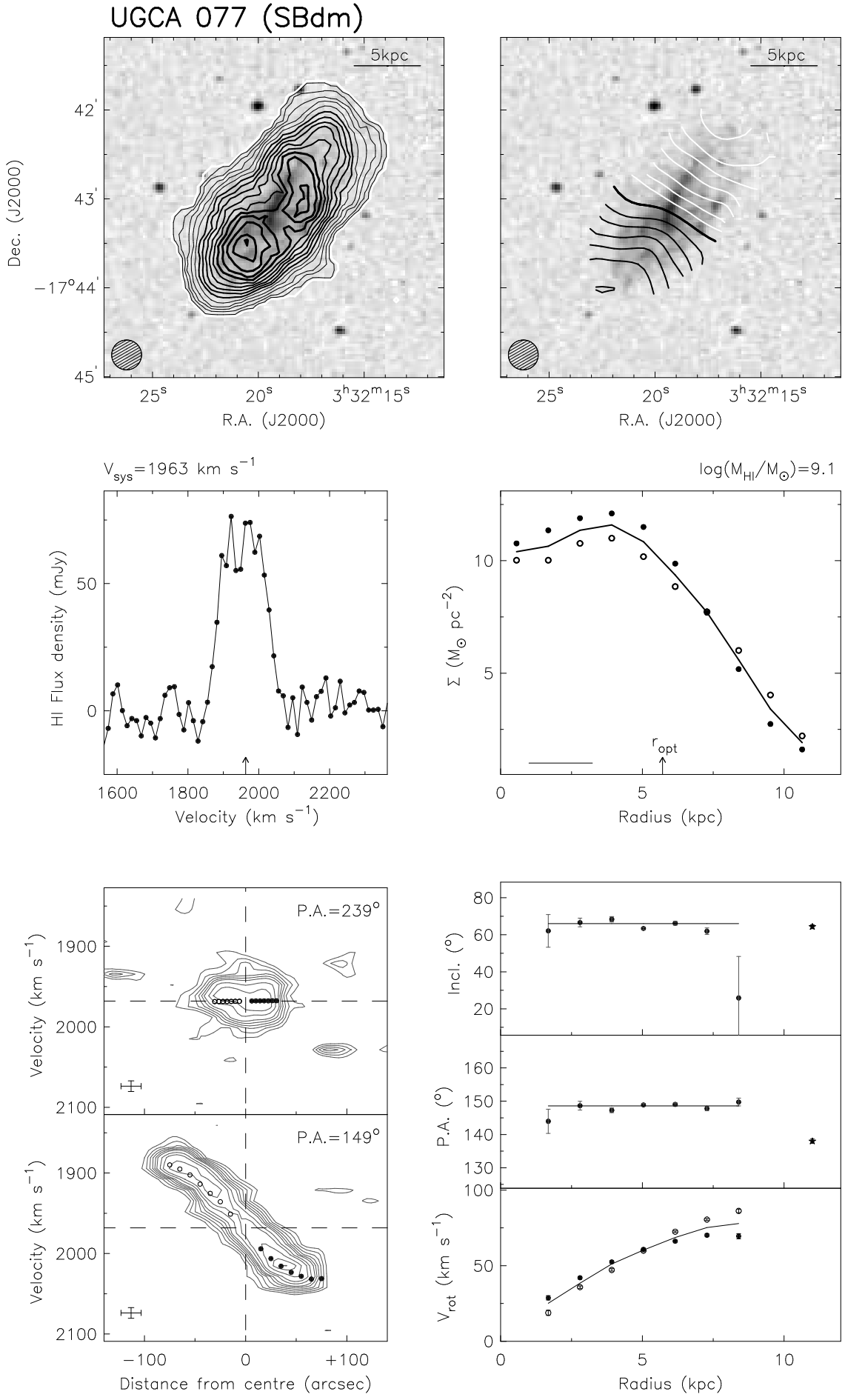
UGCA 077 (SBdm)
5kpc
Dec. (J2000)
42'
43'
−17°44'
45'
25s
20s
3h32m15s
R.A. (J2000)
5kpc
25s
20s
3h32m15s
R.A. (J2000)
Vsys=1963 km s−1
HI Flux density (mJy)
50
0
1600
1800
2000
2200
Velocity (km s−1)
log(MHI/M⊙)=9.1
Σ (M⊙ pc−2)
10
5
ropt
0
5
10
Radius (kpc)
P.A.=239°
Velocity (km s−1)
1900
2000
2100
P.A.=149°
Velocity (km s−1)
1900
2000
2100
−100
0
+100
Distance from centre (arcsec)
Incl. (°)
80
60
40
20
P.A. (°)
160
150
140
130
Vrot (km s−1)
100
50
0
0
5
10
Radius (kpc)